AD-758 778

THEORETICAL AND EXPERIMENTAL STUDIES OF VLF AND LF WAVES

Norbert Nessler

Innsbruck University
Innsbruck, Austria

28 February 1972

DISTRIBUTED BY:

NTIS
National Technical Information Service
U. S. DEPARTMENT OF COMMERCE
5285 Port Royal Road, Springfield Va. 22151

AFCRL-TR-73-0174

AD 758778

DOCUMENT CONTROL DATA - R & D

(Security classification of title, body of abstract and indexing annotation must be entered when the overall report is classified)

1. ORIGINATING ACTIVITY (Corporate author)
University of Innsbruck
Innsbruck, Austria

2a. REPORT SECURITY CLASSIFICATION

2b. GROUP

3. REPORT TITLE

THEORETICAL AND EXPERIMENTAL STUDIES OF VLF AND LF WAVES

4. DESCRIPTIVE NOTES (Type of report and inclusive dates) Scientific Final

5. AUTHOR(S) (First name, middle initial, last name)

E. BERLOFFA, D. FRITZ, R. KLEIN, H. LEONHARD, Dr. N. NESSLER, M. WIESER

6. REPORT DATE February 28, 1973

7a. TOTAL NO. OF PAGES ~~151~~ 159

7b. NO. OF REFS 40

8a. CONTRACT OR GRANT NO F44620-72-C-0052

b. PROJECT NO
4600-10

c. 52702F

d. 674700

9a. ORIGINATOR'S REPORT NUMBER(S) 4-72

9b. OTHER REPORT NO(S) (Any other numbers that may be assigned this report)

10. DISTRIBUTION STATEMENT

This document has been approved for public release and sale; its distribution is unlimited.

11. SUPPLEMENTARY NOTES Tech. other

12. SPONSORING MILITARY ACTIVITY
United States Government
American Embassy (EOAR)
London, England

13. ABSTRACT

The results of the research on the production, transmission and reception of VLF and LF waves is represented in 9 compact chapters. A new improved equivalent circuit diagram for the helix is calculated giving a good explanation of the measured effects over a large frequency range. The receiving characteristic of a ferrite rod antenna in the elliptically polarized field is investigated specifying a method that allows all ellipse parameters to be measured simultaneously. The phase measurement at VLF-wave propagation and the device built for this purpose are described and an improved universally usable digital phase measuring equipment for a large frequency range is particularized. The various pehnomena, e.g. reflection, refraction, and wave guiding, that are occurring at VLF and LF wave propagation are described and explained. A detailed description of a long-time registration of commercial VLF transmitters is given.

14 KEY WORDS	LINK A		LINK B		LINK C	
	ROLE	WT	ROLE	WT	ROLE	WT
trihedral built from ferrite rod antennas						
rotary field ellipse						
phase angles in rotary field ellipse						
spatial position of rotary field ellipse						
wave propagation in valleys						
wave guide theory for mountain valleys						
conformal mapping of hollow wave guides						
superposition of field components						
vector components of the VLF field						
measurements of the rotary field ellipse						
receiving characteristics of a ferrite rod antenna (pedaloid)						
mathematical description of pedaloid						
intersection surface of the pedaloid						
direction finding error in elliptically polarized fields						
helical antennas						
helical antennas for VLF waves						
equivalent circuit of helical antennas						
resonance frequencies of helical antennas						
parameters of helical antennas						
efficiency of helical antennas in air						
phase measurements for VLF waves						
digital phase measuring equipment						
errors of phase measuring devices						
registration of VLF transmitters						
subsurface registration of VLF transmitters						
transmission coefficient of VLF waves						

February 28, 1973

FINAL SCIENTIFIC REPORT
1972

THEORETICAL AND EXPERIMENTAL STUDIES OF VLF AND LF WAVES

Jan. 1, 1972 to Dec. 31, 1972

Dr. Norbert NESSLER
University of Innsbruck
Physics Institute
Electronics Laboratory

This document has been approved for public release and sale; its distribution is unlimited.

This research has been sponsored in part by the United States Government under Contract No. F 44620-72-C-00[illegible]
52

159

PREFACE

During the past 12 years of research on the subject "Theoretical and experimental studies of VLF and LF waves" quite a number of scientific conclusions could be drawn that are reflected in more than hundred papers and were read at several scientific conferences and meetings.

Under the VLF Research Contracts nine comprehensive thesises were completed up to now, four more are in preparation.

Experimental measurements and investigations were conducted in the home mines of Grosskogel/St. Gertraudi, Falkenstein/Schwaz, Lafatsch/Scharnitz, and salt mine Hall (all of them in the Tyrol), as well as in Bleiberg/Carinthia, Mitterberg/Salzburg and in some German and Dutch mines.

In addition to commercial apparatuses and measuring instruments we have designed and built a great number of devices and equipments ourselves to reach an utmost efficiency for our specific purposes. We may especially mention the stationary facilities in the mine of St. Gertraudi, e.g. the fully conditioned mine laboratory, the floodable gallery with the pumping equipment for subsurface experiments, and the big frame antenna, that could be constructed despite of our limited budgetary funds thanks to the generous assistance of our home industries.

The general rise in prices, the shortening of budgetary funds in connection with the financial situation of the USA and last not least the devaluation of the dollar by more than 20 % in the course of the last two years sometimes brought about very serious problems that could only be solved by the working morale of every individual member of the VLF team.

We are indebted to the director of the Montanwerke Brixlegg, Dipl.-Ing. Paul KETTNER, owner of the mine of St. Gertraudi, for being allowed to conduct our measurements there.

I should like to express by special thanks to Univ.-Prof. Dr. Rudolf STEINMAURER, Head of the Physics Department of Innsbruck University, for his benevolent support of our work and I thank all the members of the VLF-Project for the good and successful co-operation.

Norbert Nessler

VLF Team 1972

Contractor: Dr. Norbert NESSLER
Principal Investigator: Dr. Norbert NESSLER

Thesis graduates: Erich BERLOFFA[2]
Dieter FRITZ
Richard KLEIN[2]
Helmut LEONHARD
Michael OBERLADSTÄTTER[1]
Manfred WIESER

[1] Started in 1972

[2] Finished his studies in 1972.

Scientific consultant: Dr. E. SALPETER
Technical consultant: Walter GRADL

Office: Brigitte NESSLER

ABSTRACT

The results of the research on the production, transmission and reception of VLF and LF waves is represented in 9 compact chapters.

A new improved equivalent circuit diagram for the helix is calculated giving a good explanation of the measured effects over a large frequency range. The receiving characteristic of a ferrite rod antenna in the elliptically polarized field is investigated specifying a method that allows all allipse parameters to be measured simultaneously.

The phase measurement at VLF-wave propagation and the device built for this purpose are described and an improved universally usable digital phase measuring equipment for a large frequency range is particularized.

The various phenomena, e.g. reflection, refraction, and wave guiding, that are occurring at VLF and LF wave propagation are described and explained.

A detailed description of a long-time registration of commercial VLF transmitters is given.

CONTENTS

LIST OF ILLUSTRATIONS

Chapter 1

Chapter 2

Chapter 3

Chapter 4

Chapter 5

Chapter 6

Chapter 7

Chapter 8

Chapter 9

CHAPTER 1

HELICAL ANTENNAS IN THE VLF-RANGE

The impedances of the antennas H 1136, H 328, and H 329 Cull in air showed the same characteristic shape of real and imaginary part in the graphical representation as has been stated earlier with the antenna H 772 /1/. The shape of the curves computed at Innsbruck University reminds of the impedance characteristics of a quartz crystal. It was now near at hand to examine the equivalent circuit diagram of a quartz crystal more thoroughly with particular consideration of its applicability for the special case and possibly to modify it.

The equivalent circuit diagram

A small helix for long waves can be thought of as composed in the following way:

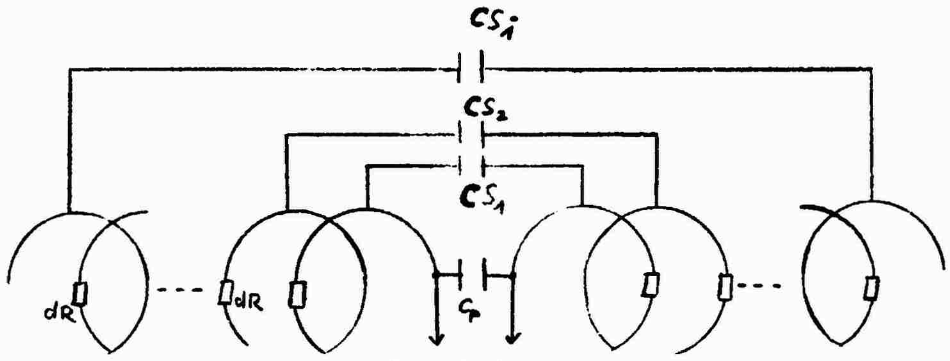

Fig. 1.1

with dL, dR, C_p being constant, CS_i being different.

In the simplified diagram

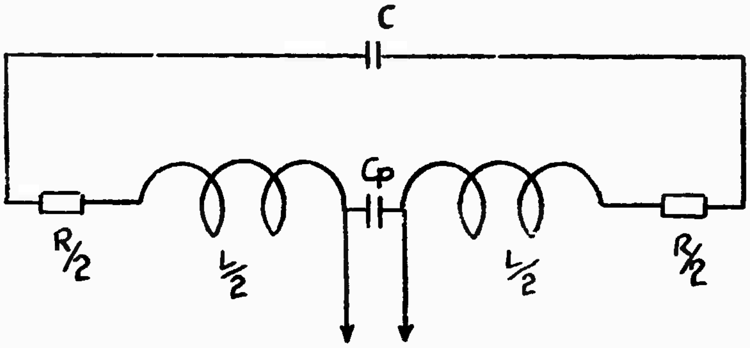

Fig. 1.2

all CS_i were united to C; R, L, C, and C_p remain constant. Fig. 1.3 shows the modified diagram.

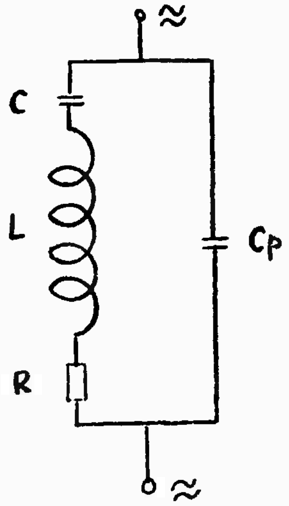

Fig. 1.3

This diagram is identical with the equivalent circuit diagram of a quartz crystal.

Calculation of the impedance of the circuit

The complex conductance amounts to

$$Y = j\omega C_p + \frac{1}{R + j(\omega L - \frac{1}{\omega C})} \quad \text{with } \omega = 2\pi f$$

or

$$Y = \frac{1}{R^2 + (\omega L - \frac{1}{\omega C})} + j \left(- \frac{\omega L - \frac{1}{\omega C}}{R + (\omega L - \frac{1}{\omega C})} + \omega C_p \right) \qquad (1.1)$$

with real and imaginary part separated.

Therefrom real and imaginary part of the complex total resistance Z is calculated to be

$$\mathrm{Re}Z = \frac{R}{1 + \omega^2 C_p{}^2 (R^2 + H^2) - 2\omega C_p \cdot H} \qquad (1.2)$$

$$\mathrm{Im}Z = \frac{H - \omega C_p (R^2 + H^2)}{1 + \quad C_p \ (R \ + H \ ) - 2 \ C_p \cdot H} \qquad (1.3)$$

with the abbreviation

$$H = (\omega L - \frac{1}{\omega C})$$

Resonance frequencies

The resonance frequencies are calculated from ImZ = 0, resulting

$$H - \omega C_p (R^2 + H^2) = 0 \qquad (1.4)$$

and therefrom we obtain a biquadratic equation for ω:

$$\omega^4 - \omega^2 \left(\frac{1}{LC_p} - \frac{R^2}{L^2} + 2 \cdot \frac{1}{LC} \right) + \frac{1}{C} \ \frac{1}{L^2 C_p} + \frac{1}{L^2 C^2} = 0 \qquad (1.5)$$

with the solution

$$\omega_{res}^2 = \frac{1}{2LC_p} - \frac{R^2}{2L^2} + \frac{1}{LC} \pm \frac{1}{2LC_p} \sqrt{1 + \frac{R^4 C_p{}^2}{L^2} \quad \frac{4R^2 C_p{}^2}{LC} \quad \frac{2R^2 C_p}{L}} \qquad (1.6)$$

With the antennas in question, R and C are small, L is large; so the following approximations can be introduced:

$$\frac{2R^2C_p}{L} < 1; \qquad \frac{4R^2C_p{}^2}{LC} < 1.$$

The root is expanded into a series, the term $\frac{R^4C_p}{L^2}$ can be neglected.

$$\omega^2_{res} \quad \frac{1}{LC} + \frac{1}{2LC_p} - \frac{R^2}{2L^2} \pm \frac{1}{2LC_p}\left(1 - \frac{2R^2C_p{}^2}{LC} - \frac{R^2C_p}{L}\right) \tag{1.7}$$

resulting

$$\omega_1^2 \qquad \frac{C + C_p}{LCC_p}\,(1 - \frac{R^2C_p}{L}) \tag{1.8}$$

$$\omega_2^2 \qquad \frac{1}{LC}\,(1 + \frac{R^2C_p}{L}) \tag{1.9}$$

For the special case R = 0 all neglected terms disappear so that the resonance frequency reads as follows:

$$\omega_1^2\,(R=0) = \frac{C+C_p}{LCC_p} = \omega_{10}^2; \quad \omega_{10} = \frac{1}{\sqrt{LC}}\sqrt{1 + \frac{C}{C_p}} \tag{1.10}$$

$$\omega_2^2\,(R=0) = \frac{1}{LC} = \omega_{20}^2; \quad \omega_{20} = \frac{1}{\sqrt{LC}} \tag{1.11}$$

Thus, two neighboring resonance frequencies appear: The first (lowest) resonance originates in the series circuit L-R-C (Fig. 1.3) with C_p as capacitive load parallel to the generator.

The second (slightly higher) resonance forms in the parallel circuit L-R on the one hand and C in series with C_p on the other hand. The tap occurs at the capacitive divider C, C_p.

From (1.8) and (1.9)

$$\omega_1 \approx \omega_p = \frac{1}{\sqrt{LC}} \sqrt{1 + \frac{C}{C_p}} \left(1 - \frac{R^2 C_p}{2L}\right) \tag{1.12}$$

$$\omega_2 \approx \omega_s = \frac{1}{\sqrt{LC}} \left(1 + \frac{R^2 C_p}{2L}\right) \tag{1.13}$$

is calculated.

Generally, $\frac{R^2 C_p}{2L} << 1$, i.e. the shift of the resonance frequency on account of the loss resistance is negligible with the antennas used here (smaller than the inaccuracy of measurement).

Loss factors are:

for parallel resonance $\left(\frac{R^2 C_p}{2L} << 1\right)$

$$\tan \delta_p = \frac{IR}{I\omega_p \cdot L} \qquad \frac{R}{\omega_{p_o} \cdot L} = R\sqrt{\frac{C}{L\left(1 + \frac{C}{C_p}\right)}} \tag{1.14}$$

for series resonance $\left(\frac{R^2 C_p}{2L} << 1\right)$

$$\tan \delta_s = \frac{R}{\omega_s \cdot L} \qquad \frac{R}{\omega_{s_o} \cdot L} = R\sqrt{\frac{C}{L}} \tag{1.15}$$

With the assumption of small loss factors the resonant impedances are calculated as

$$|Z| \approx \frac{1}{R(\omega_{p_o} C_p)^2} = \frac{C_p \cdot L}{RC_p(C + C_p)} = R_p \tag{1.16}$$

for parallel resonance, and

$$Y = \frac{1}{R}\,(1 + j\omega_{s_o} C_p \cdot R) \approx \frac{1}{R} \qquad \frac{1}{|Y|} = R_s \approx R \qquad (1.17)$$

for series resonance.

From the loss factors both quality and band width can be calculated:

$$Q_s = \tan\delta_s = \frac{1}{R}\sqrt{\frac{L}{C}}\,, \qquad Q_p = \frac{1}{R}\sqrt{\frac{L\left(1 - \frac{C}{C_p}\right)}{C}}$$

$$b = \Delta f = \tan\delta \cdot f_{res} \Longrightarrow b_s = b_p = \frac{R}{2\pi \cdot L} \qquad (1.18)$$

The calculation of the constants L, R, C, and C_p from the geometric and electric data of antenna and feed line

Inductance L: calculated in approximation as inductance of a long air-core coil /2/. An accurate calculation is given in /3/:

Inductance of a single-layer cylindrical coil:

$$L_o = \frac{21.8 \cdot n^2 \cdot r}{1 + 2.2 \cdot \frac{l}{r}} \cdot 10^{-7} \qquad |H, m| \qquad (1.19)$$

2l .... total length

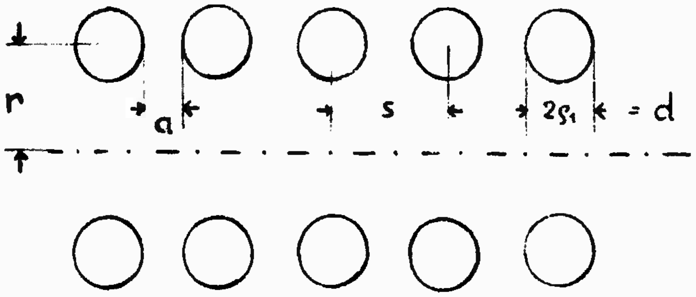

Fig. 1.4

If the clear distance a between two neighboring windings is not equal to the wire thickness $2\rho_1 = d$, the correction term ΔL must be added to Eq. (1.19).

$$\Delta L = 2n \cdot K_8 \cdot r \cdot 10^{-7} \qquad |H, m| \qquad (1.20)$$

The correction factor K_8 can be taken from Fig. 1.5.

Series loss resistance R_{total}:

The series loss resistance R of the antenna consists of the following partial resistances:

$$R_{total} = R_{wire} + R_{eddy\ curr.} + R_{diel.} + R_{rad.}$$

1. R_{wire} is the Ohmic resistance of the wire where a current I with the frequency f flows. Current displacement by skin and proximity effect must be considered at the calculation of R_{wire}.

The Ohmic resistance R_o of the wire material can be taken from tables /4/. The Ohmic resistances for wire gauges relevant for helical antennas are listed in Table 1.1.

Table 1.1: Resistance of a round Cu wire in dependence of diameter.

Ø $\|mm\|$	q $\|mm^2\|$	R(Ohm/m)	1 per R $\left\|\frac{m}{\Omega}\right\|$
0.9	0.6362	0.0281	35.6
1.0	0.7854	0.0227	43.9
1.1	0.9503	0.0188	53.2
1.2	1.131	0.0158	63.2
1.5	1.767	0.0101	99

The increase of resistance caused by skin effect is thoroughly dealt with in /3/, approximation formulas are given:

For $\frac{d}{b} < 2$ $$R = R_o \tag{1.21}$$

$2 < \frac{d}{b} < 4$ $$R = R_o\left[1 + \left(\frac{d}{5.3b}\right)^4\right] \tag{1.22}$$

$\frac{d}{b} > 4$ $$R = R_o\left[\frac{d}{4b} + 0.25\right] \tag{1.23}$$

$\frac{d}{b} > 10$ $$R = R_o \frac{d}{4b} \tag{1.24}$$

d .... wire diameter

b .... equivalent conducting layer thickness (cf. Eq. 1.25)

$$b = \frac{6.4\ K_1}{\sqrt{f}} \cdot 10^{-2} \qquad |m, H_z| \tag{1.25}$$

The correction factor K_1 is dependent upon the wire material and can be seen from Table 1.2

Table 1.2

material	K_1
silver	1.00
copper	1.03
aluminum	1.37
zinc	1.97
brass	2.2
platinum	2.62

or can be taken directly from Fig. 1.6 in dependence on the frequency.

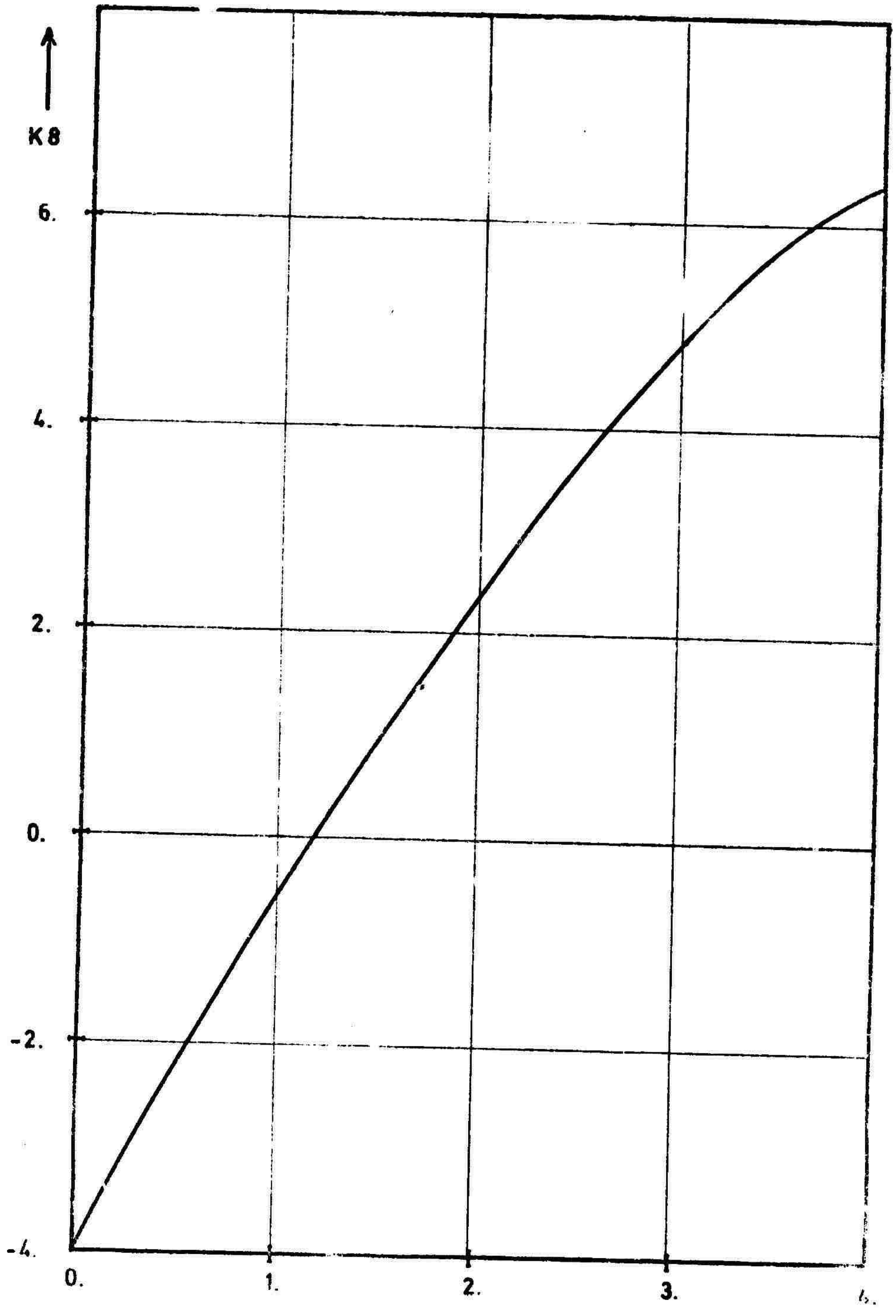

FIG. 1.5 CORRECTION FACTOR K8

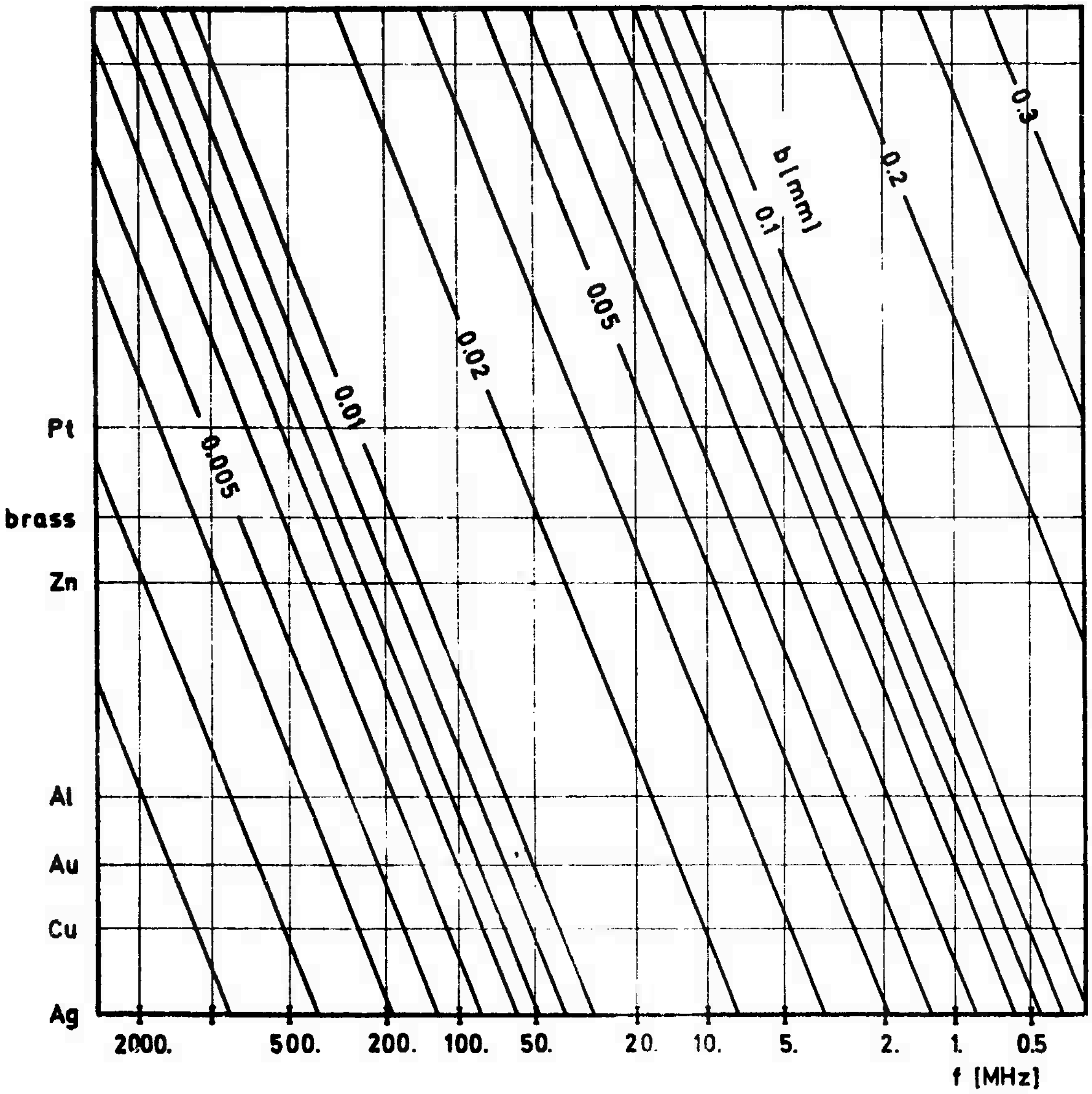
Pt
brass
Zn
Al
Au
Cu
Ag
0.005
0.01
0.02
0.05
0.1
b [mm]
0.2
0.3
2000.
500.
200.
100.
50.
20.
10.
5.
2.
1.
0.5
f [MHz]

FIG. 1.6

The resistance of a 1 m silver wire in dependence on the frequency and the radius of the wire can be deduced from Fig. 1.7. If we use another wire the effective radius must be divided by the factor K_1.

Proximity effect: If currents are flowing in neighboring wires in same or opposite directions, current displacement occurs in addition to the skin effect on account of the change of magnetic fields according to Fig. 1.8.

same current direction

opposite current direction

Fig. 1.8: Proximity effect

The hf-resistance of the respective wire is thus increased. By multiplying the hf-resistance by the correction factor K_2 this increase is taken into account. For the case of two parallel wires with circular cross section, K_2 can be taken from Fig. 1.9.

$\underline{R_{eddy\ current}}$ is caused by the surrounding conductive rock and by the influence of the measuring devices.

If the antenna is surrounded by a second shorted wire with the resistance R_2, $R_{eddy\ current}$ reads

$$R_{eddy\ current} = \omega^2 \frac{M^2}{R^2} \qquad (1.26)$$

M .... mutual induction

for the frequency range up to about 0.5 MHz, i.e., $R_{\text{eddy current}}$ is increasing proportionally to f^2. For higher frequencies, the approximation

$$R_{\text{eddy current}} = R_2 \cdot k^2 \frac{L_1}{L_2} \tag{1.27}$$

k .... coupling coefficient

is valid, i.e., the increase of eddy-current resistance is only proportional to the increase in R_2 by the skin effect.

$\underline{R_{\text{diel.}}}$ consists of losses caused by the capacitive currents in the wire isolation and in the carrier material. For constant current $R_{\text{diel.}}$ increases with f^3.

$$R_{\text{diel.}} = 0.25 \cdot f^3 \cdot C_L \cdot L^2 \cdot d_c \cdot 10^3 \quad |\Omega, \text{Hz}, \text{F}, \text{H}| \tag{1.28}$$

C_L .... self-capacitance of the antenna
L ..... inductivity of the antenna
d_c .... loss factor of the dielectric

The value of C_L can be seen from Fig. 1.10 (with the same designation as in Fig. 1.4), d_c from tables, e.g. in /4/.

$\underline{R_{\text{radiation}}}$ must be considered only with very high frequencies or in the case of antenna dimensions larger than $\lambda/10$ (λ = working wavelength). In /5/ radiation resistances for smaller antennas (capacitive or inductive standard antenna) are quoted:

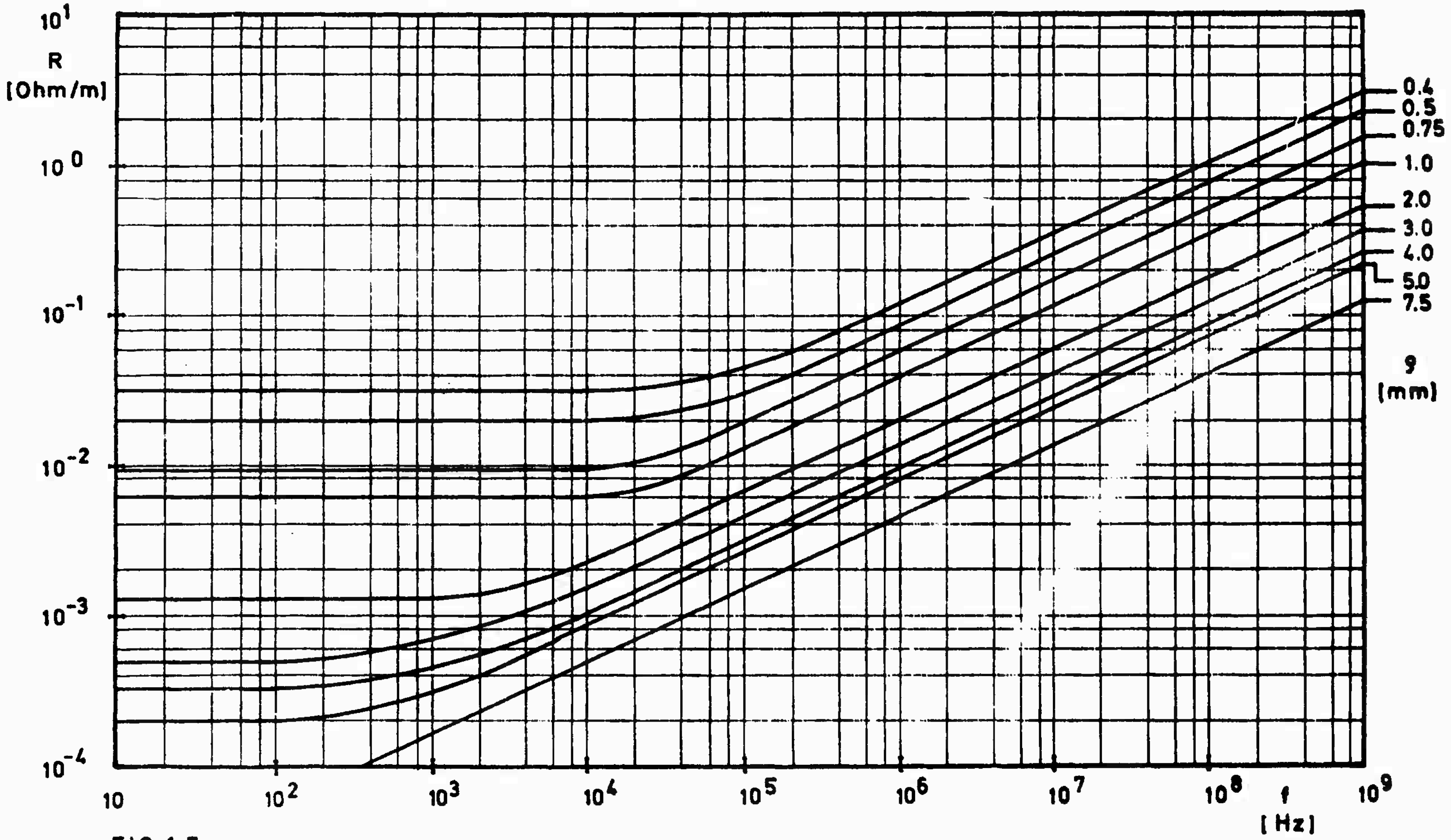

10^1
R
[Ohm/m]
10^0
10^-1
10^-2
10^-3
10^-4
10
10^2
10^3
10^4
10^5
10^6
10^7
10^8
f
[Hz]
10^9
0.4
0.5
0.75
1.0
2.0
3.0
4.0
5.0
7.5
9
[mm]

FIG. 1.7

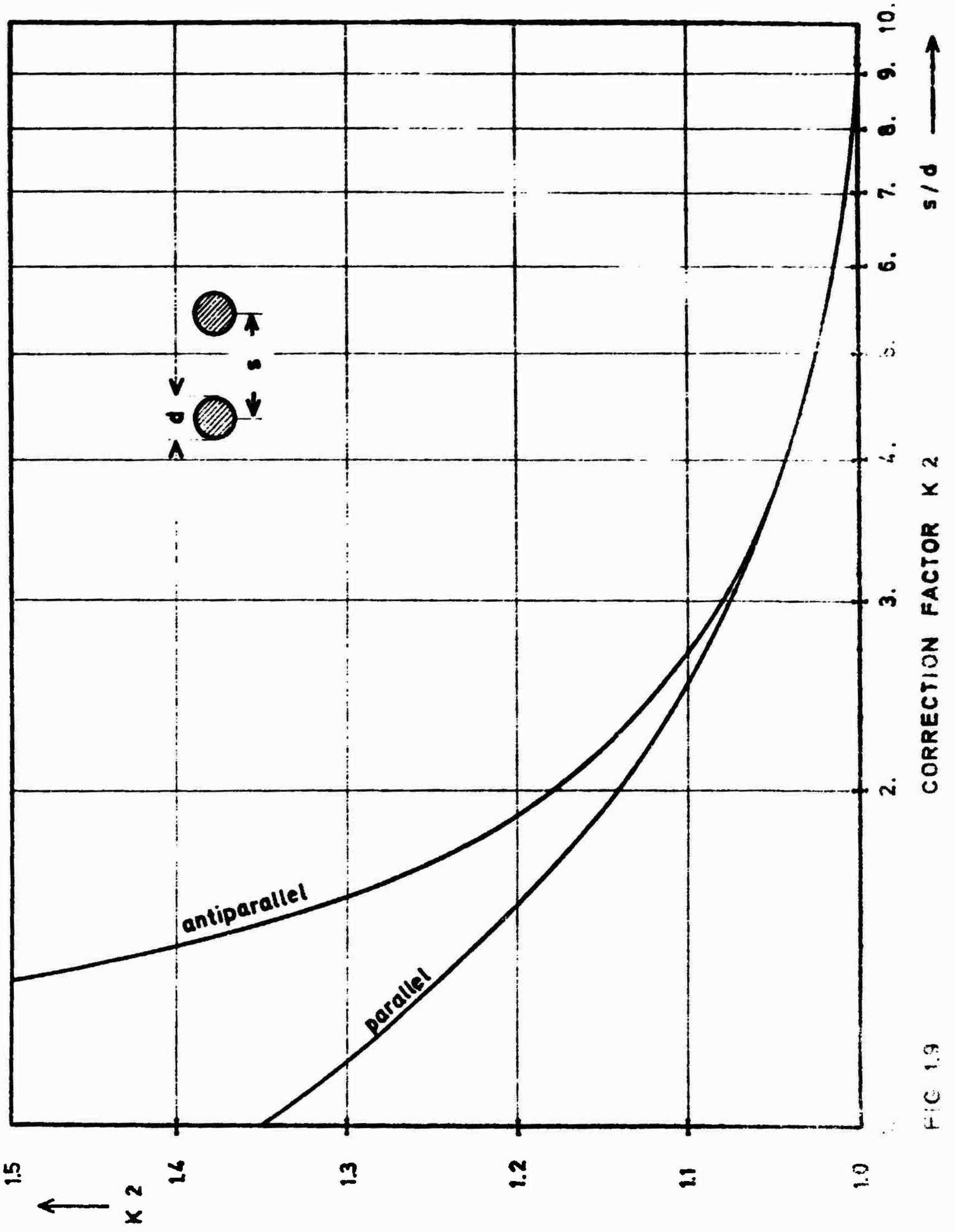

CORRECTION FACTOR K 2

FIG 1.9

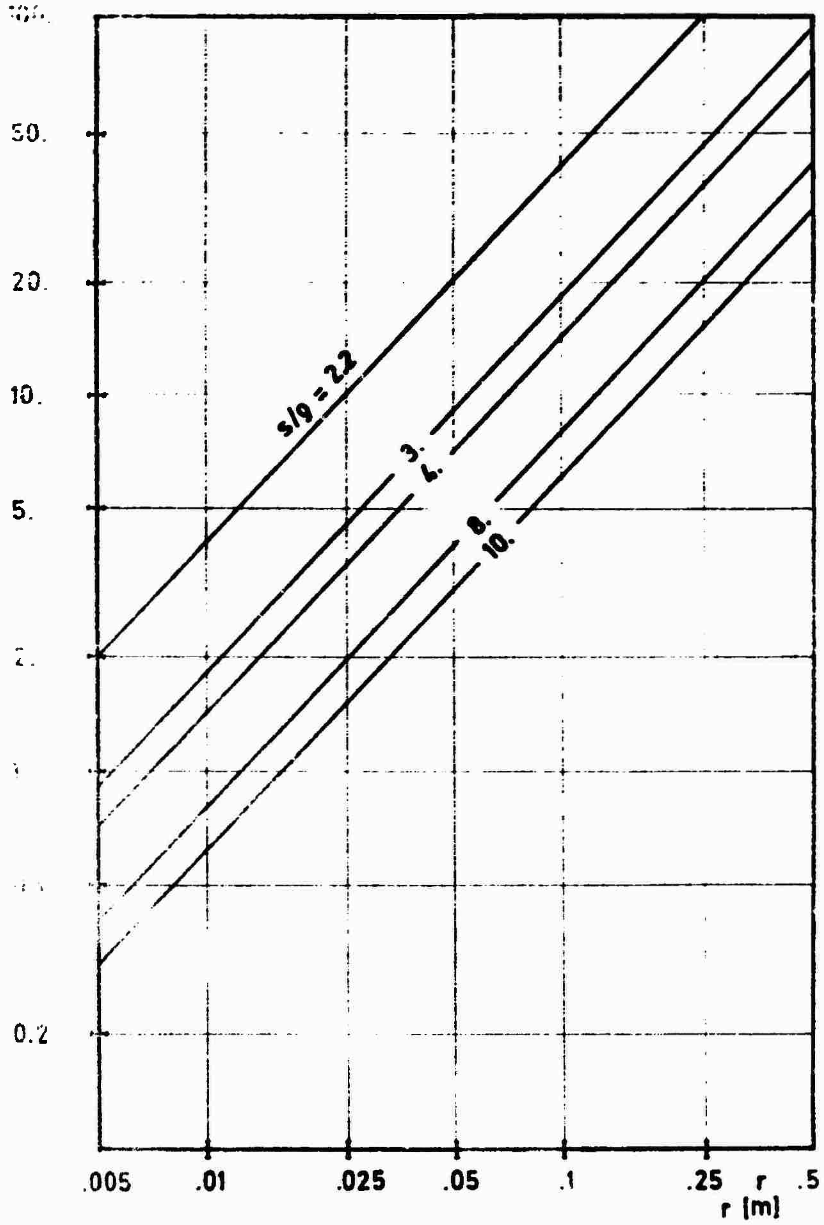

FIG. 1.10

capacitive antenna $$R_e = 80 \cdot \pi^2 \cdot \left(\frac{l}{\lambda}\right)^2 \qquad (1.29)$$

inductive antenna $$R_m = 80 \cdot \pi^2 \cdot \left(\frac{n \cdot A}{\lambda^2}\right)^2 \qquad (1.30)$$

λ ..... wavelength

l ..... length of the electric dipole

n·A ... turn area of the magnetic dipole

R_e, R_m . radiation resistances

In every case, however, R_{rad} is essentially (several decimal powers) smaller than R_{wire} and R_{diel}, respectively.

With sufficiently large gallery cavity, $R_{eddy\ current}$ is as well much smaller than R_{wire} and R_{diel} on account of the low conductivity of the surrounding rock and the small dimensions of the used measuring devices.

Capacity C: For the calculation of C, the approximation formula for the static capacity of a symmetric cylindrical antenna has proved useful. According to /6/

$$C = \frac{2\pi\varepsilon_0 \cdot l}{\ln\left(\frac{l}{3r^2}\right)} = \frac{\pi \cdot \varepsilon_0 \cdot l}{\ln\left(\frac{l}{r}\right) - 0.55} = \frac{3.54 \cdot l}{\ln\left(\frac{l}{r}\right) - 0.55} \cdot 10^{-13} \quad |F,m| \qquad (1.31)$$

2l .... total length of the antenna

r ..... radius of the cylinder

$2l > r$

In this simple form the equation is only valid with comparatively narrow windings (as e.g. at H 772, H 1362, H 1136 Cull, H 328 etc.).

C_p is calculated from the parallel connection of the capacity of the feed line and the capacity of the two inner windings:

$$C_p = C_K + C_i$$

According to /3/ the feed-line capacity appears as the capacity of the symmetric two-wire line and reads

$$C_k = \frac{\pi \cdot \varepsilon_0 \cdot \varepsilon_r \cdot l}{\ln\left(\frac{D}{d}\right) + \sqrt{\frac{D^2}{d^2} - 1}} = \frac{0.121 \cdot \varepsilon_r \cdot l}{\log\left(\frac{D}{d} + \sqrt{\frac{D^2}{d^2} - 1}\right)} \cdot 10^{-10} \quad |F,m| \qquad (1.32)$$

D .... distance between wires

d .... diameter of the wires

l .... length of the wires

Generally, the cable capacity is given by the manufacturers or can easily be determined by experiment.

The capacity C_i of the two inner windings of the antenna can be calculated according to /3/ as the capacity of two parallel wires of the length l, of the antenna circumference $2r\pi$, the distance D and the diameter d:

$$C_i = \frac{0.121 \cdot \varepsilon_r \cdot l}{\log\left(\frac{D}{d} + \sqrt{\frac{D^2}{d^2} - 1}\right)} \cdot 10^{-10} = \frac{0.754 \cdot \varepsilon_r \cdot r}{\log\left(\frac{D}{d} + \sqrt{\frac{D^2}{d^2} - 1}\right)} \cdot 10^{-10} \quad |F,m| \qquad (1.33)$$

with ε_r to be determined experimentally on account of the influence of the wire isolation (ε not known with sufficient accuracy).

Numerical evaluation of the parameters of the equivalent circuit diagram for the antennas H 1136 Cull, H 328 I, H 328 II:

Table 1.3: Geometrical data

quantity	unit	H 1136 Cull	H 328 I	H 328 II	Remark
n		1136	328	328	
r	m	$1.43 \cdot 10^{-1}$	$5.5 \cdot 10^{-2}$	$5.5 \cdot 10^{-2}$	
s	m	$1.72 \cdot 10^{-3}$	$2.5 \cdot 10^{-3}$	$2.5 \cdot 10^{-3}$	
ρ	m	$0.75 \cdot 10^{-3}$	$5 \cdot 10^{-4}$	$5 \cdot 10^{-4}$	
l	m	0.977	0.41	0.41	
d_c		$4 \cdot 10^{-3}$	$4 \cdot 10^{-3}$	$4 \cdot 10^{-3}$	loss factor of the dielectric carrier material

Table 1.4: Results

quantity	unit	equation	H 1136 Cull	H 328 I	H 328 II
L	H	19, 20	$2.7 \cdot 10^{-2}$	$8.04 \cdot 10^{-4}$	$8.04 \cdot 10^{-4}$
R_{wire}	Ω	24, 25	57	16	16
$+ R_{diel.}$	Ω	28	332	24	24
$= R_{total}$	Ω		389	40	40
C	F	31	$20.1 \cdot 10^{-12}$	$7.8 \cdot 10^{-12}$	$7.8 \cdot 10^{-12}$
C_p	F	32, 33	$90 \cdot 10^{-12}$	$98 \cdot 10^{-12}$	$1.97 \cdot 10^{-9}$

__H 328 II:__ Same data as for H 328 I, C_p artificially increased by parallelling of a low-induction ceramic drop capacitor.

The measurements, their evaluation and comparison with the equivalent circuit diagram

The measurements were executed in a larger cavity in the SO-gallery of the mine St. Gertraudi/Tyrol. The following measuring devices were used:

for the frequency range up to 600 kHz:

selective levelmeter SPM-2, Wandel & Goltermann
decade R-C-generator TG 66 A, Levell
three-stage preamplifier, gain 80 dB, 50-1000 kHz, transistorized, constructed in the VLF-lab

for the frequency range over 600 kHz:

L-C-generator, transistorized, constructed in the VLF-lab
selective heterodyne voltmeter 2006, Brüel & Kjaer

for both frequency ranges:

R-C-L-bridge LE 300/A 1, Hatfield
frequency counter, type 100A, Monsanto

The values of RE Z (exp) and IM Z (exp) were computed according to the formulas given in /1/ and listed in tables 1.5 to 1.7.

The columns mean from the left to the right:

f	kHz	working frequency
RE Z (exp)	kΩ	real part of impedance calculated from experiment
RE Z (th)	kΩ	real part of impedance calculated from the equivalent circuit diagram
DRE Z		ratio RE Z (exp) / RE Z (th)
IM Z (exp)	kΩ	imaginary part of impedance calculated from experiment
IM Z (th)	kΩ	imaginary part of impedance calculated from the equivalent circuit diagram
DIM Z		ratio IM Z (exp) / IM Z (th)

A graphical representation of the measuring results is shown in Figs. 1.11 to 1.16.

Tab. 1.5

F	RE Z (EXP)	RE Z (TH)	DRE Z	IM Z (EXP)	IM Z (TH)	DIM Z
50.0	0.1327E-[illegible]	0.1648E+01	124.16	-0.2893E+02	-0.2687F+02	0.93
100.0	0.1757E[illegible]1	0.5574E+00	31.73	-0.1398E+02	-0.1324E+02	0.95
120.0	0.2114[illegible]01	0.4642E+00	21.96	-0.1135E+02	-0.1076E+02	0.[illegible]5
150.0	0.31[illegible]01	0.3358E+00	10.72	-0.8495E+01	-0.8086E+01	0.[illegible]5
180.0	0.[illegible]E-01	0.2392E+00	4.12	-0.6088E+01	-0.5965E+01	0.[illegible]
200.0	0[illegible]E+00	0.1775E+00	1.60	-0.4190E+01	-0.3971E+01	0.[illegible]
210.0	[illegible]66E+00	0.1837E+00	1.04	-0.2836E+01	-0.2600E+01	0.92
215.0	[illegible]361E+00	0.2224E+00	0.94	-0.1918E+01	-0.1652E+01	0.56
218.0	0.2886E+00	0.2673E+00	0.93	-0.1236E+01	-0.8261E+00	0.67
220.0	0.3345E+00	0.3740E+00	1.12	-0.7039E+00	-0.2171E+00	0.[illegible]
222.0	0.3930E+00	0.5025E+00	1.28	-0.898[illegible]E-01	0.8075E+00	[illegible]
240.0	0.8436E+01	0.9761E+01	1.16	0.2536E+02	0.1855E+02	0.[illegible]
250.0	0.5707E+01	0.6202E+01	1.09	-0.3314E+02	-0.2280E+02	0.[illegible]
300.0	0.4775E-01	0.1954E-01	0.41	-0.7928E+01	-0.4421E+01	0.56
350.0	0.1108E-01	0.1770E+00	15.97	-0.5892E+01	-0.4681E+01	0.79
400.0	0.4340E-02	0.1837F+00	42.33	-0.4881E+01	-0.3970E+01	0.81
450.0	0.2140E-02	0.1464E+00	68.40	-0.4217E+01	-0.3461E+01	0.82
500.0	0.1204E-02	0.1389E+00	115.36	-0.3731E+01	-0.2761E+01	0.74

14-b

Tab. 1.6

F	RE Z (EXP)	RE Z (TH)	DRE Z	IM Z (EXP)	IM Z (TH)	DIM Z
1000.0	0.4029E-03	0.1583E-02	3.93	-0.1466E+01	-0.3979E+01	2.71
1500.0	0.9[illegible]2E-03	0.7036E-03	0.71	-0.9181E+00	-0.2653E+01	2.89
1300.0	0.[illegible]312E-02	0.1909E-03	0.06	-0.6527E+00	-0.1382E+01	2.17
1900.0	0.5922E-02	0.6744E-04	0.01	-0.5133E+00	-0.8212E+00	1.60
1950.0	0.1173E-01	0.1167E-01	0.99	-0.4001E+00	-0.4182E+00	1.05
2000.0	0.2462E-01	0.2419E-01	0.98	-0.2014E+00	-0.2544E+00	1.26
2020.0	0.3684E-01	0.3653E-01	0.99	-0.6498E-01	-0.7487E-01	1.15
2030.0	0.4676E-01	0.4676E-01	1.00	0.2808E-01	0.3435E-01	1.22
2040.0	0.6138E-01	0.5043E-01	0.82	0.1474E+00	0.1810E+00	1.23
2050.0	0.8424E-01	0.5072E-01	0.60	0.3067E+00	0.3224E+00	1.05
2080.0	0.3618E+00	0.5383E-01	0.15	0.1440E+01	0.8970E+00	0.62
2100.0	0.3880E+01	0.2836E-01	0.01	0.5407E+01	0.1684E+01	0.31
2200.0	0.2968E-01	0.5815E-01	1.96	-0.1346E+01	-0.2411E+02	17.92
2500.0	0.1454E-02	0.3958E-03	0.27	-0.7676E+00	-0.1989E+01	2.59
3000.0	0.2292E-03	0.2171E-01	94.72	-0.5800E+00	-0.1473E+01	2.54
4000.0	0.3567E-04	0.9894E-02	277.37	-0.4172E+00	-0.9946E+00	2.38

Tab. 1.7

F	RE Z (EXP)	RE Z (TH)	DRE Z	IM Z (EXP)	IM Z (TH)	DIM Z
1500.0	0.3342E-05	0.1441E-02	431.12	-0.5323E-01	-0.8486E-01	1.59
1800.0	0.1499E-04	0.1478E-02	98.61	-0.4392E-01	-0.6546E-01	1.49
1900.0	0.4424E-04	0.1213E-02	27.42	-0.4104E-01	-0.5981E-01	1.46
1950.0	0.1126E-03	0.1138E-02	10.11	-0.3921E-01	-0.5439E-01	1.39
2000.0	0.7361E-03	0.1923E-02	2.61	-0.3509E-01	-0.4202E-01	1.20
2020.0	0.5069E-02	0.8723E-02	1.72	-0.2724E-01	-0.2511E-01	0.92
2030.0	0.3434E-01	0.5318E-01	1.55	-0.3171E-01	0.6593E-02	-0.21
2040.0	0.7071E-02	0.3920E-01	5.54	-0.5374E-01	-0.1121E+00	2.09
2050.0	0.1858E-02	0.8138E-02	4.38	-0.4719E-01	-0.8178E-01	1.73
2100.0	0.1441E-03	0.1246E-02	8.65	-0.4056E-01	-0.6313E-01	1.56
2200.0	0.2297E-04	0.2429E-03	10.57	-0.3745E-01	-0.5399E-01	1.44
2500.0	0.2602E-05	0.1453E-06	0.06	-0.3247E-01	-0.3812E-01	1.17
3000.0	0.4944E-06	0.7402E-07	0.15	-0.2694E-01	-0.2721E-01	1.01
4000.0	0.8332E-07	0.1759E-07	0.21	-0.2016E-01	-0.1326E-01	0.66

14 - D

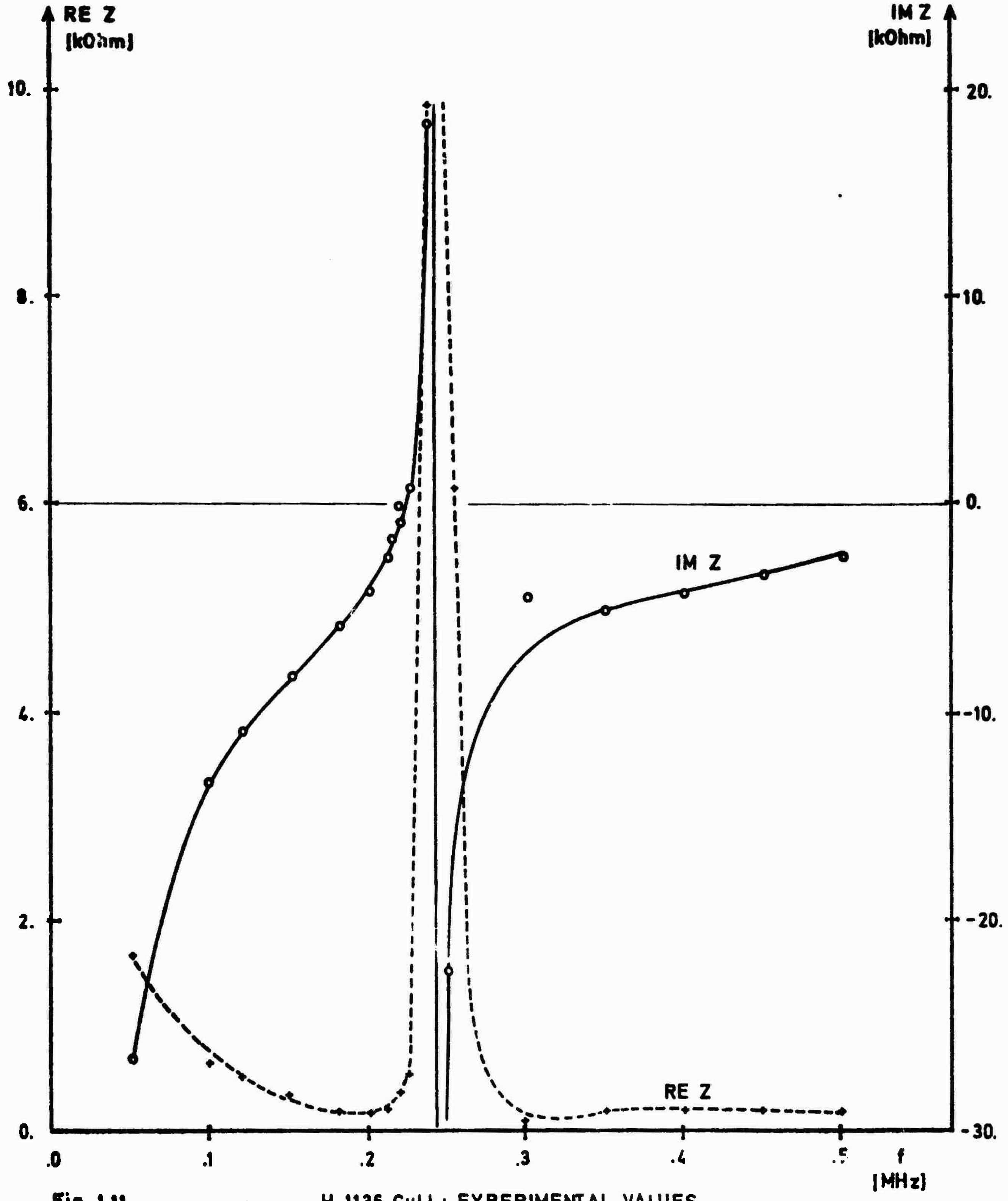

Fig. 1.11 H 1136 CuLL: EXPERIMENTAL VALUES

14.e

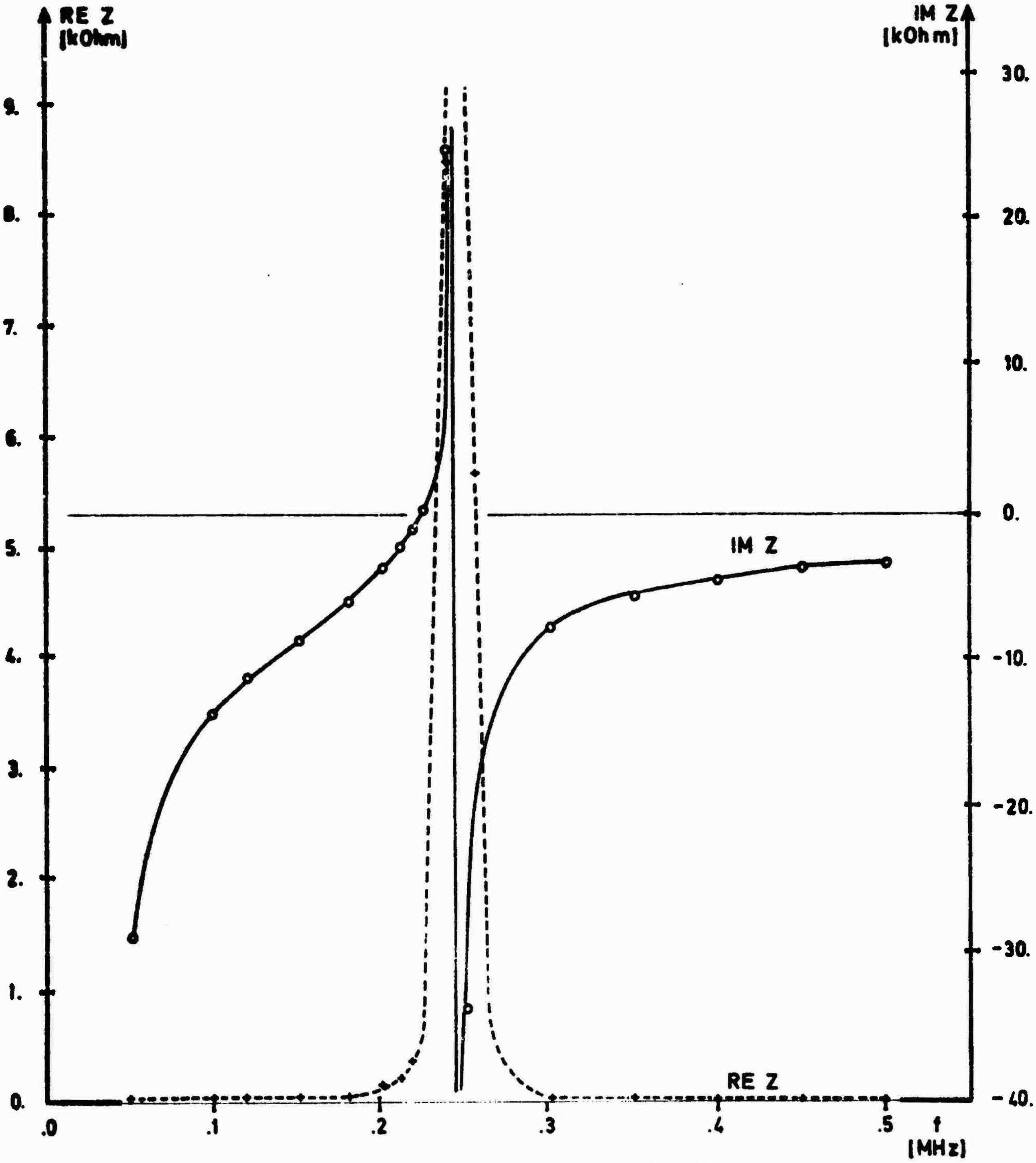

Fig. 1.12 H 1136 CuLL : THEORETICAL VALUES

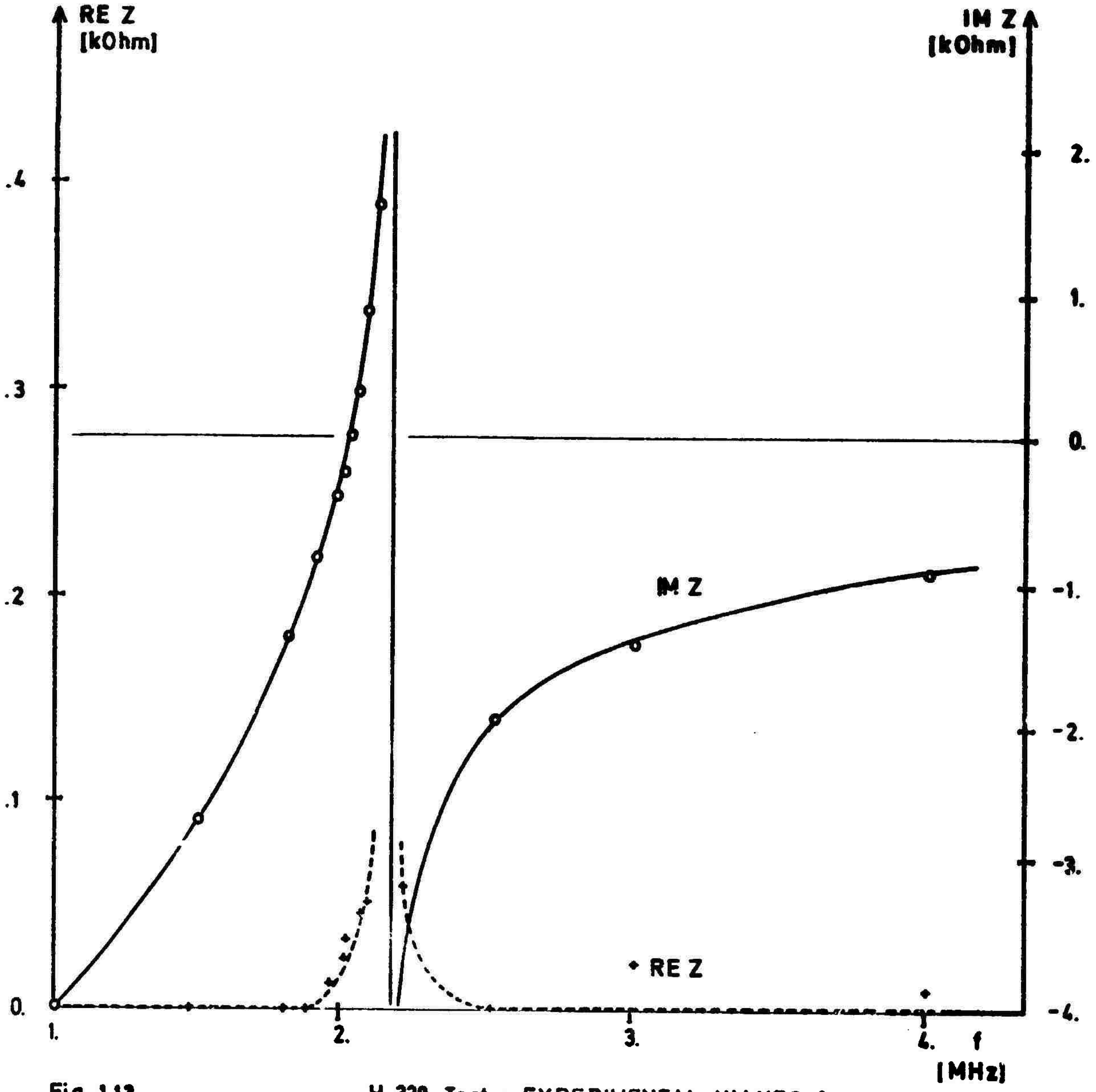

Fig. 1.13 H 328 Test : EXPERIMENTAL VALUES I

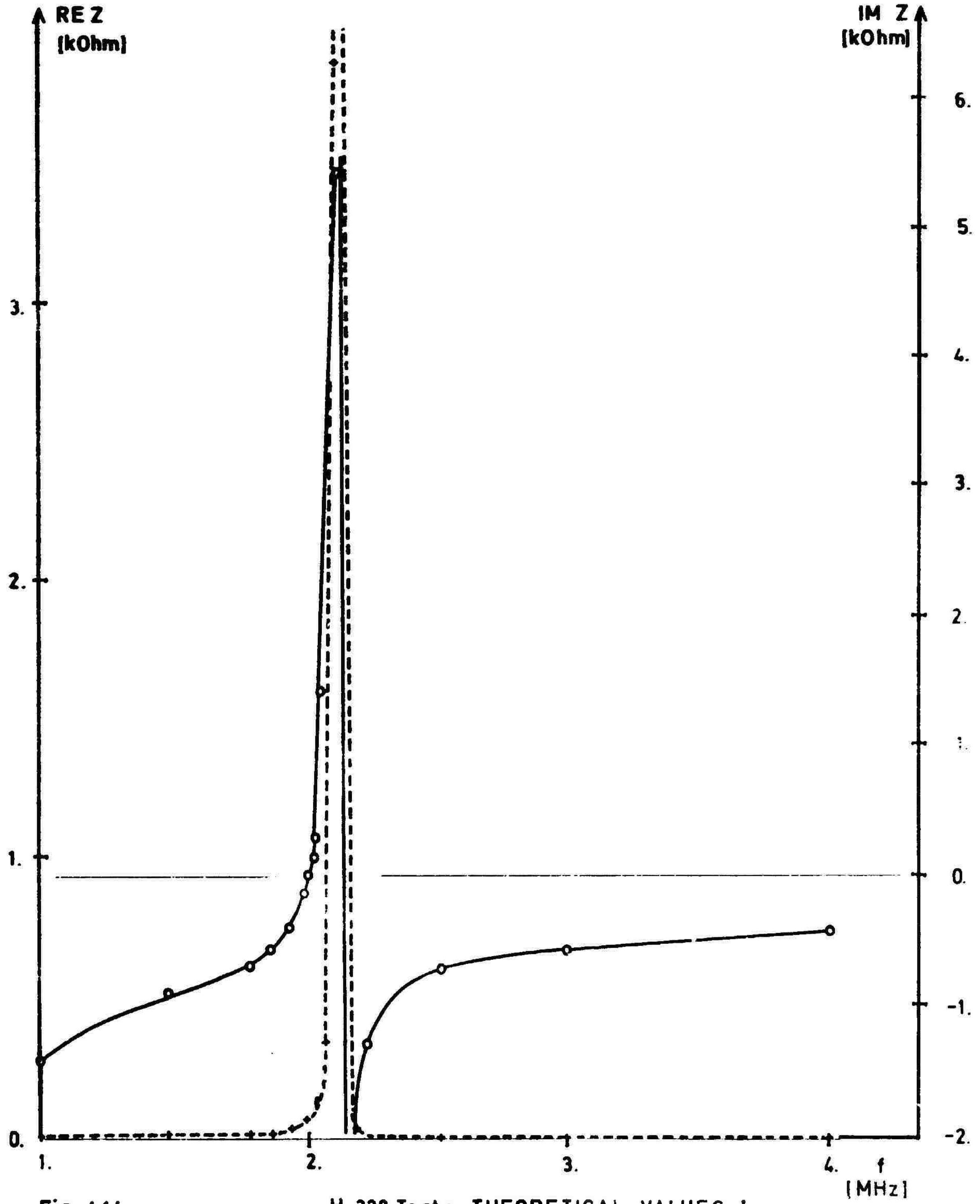

Fig. 1.14 H 328 Test : THEORETICAL VALUES I

14-H

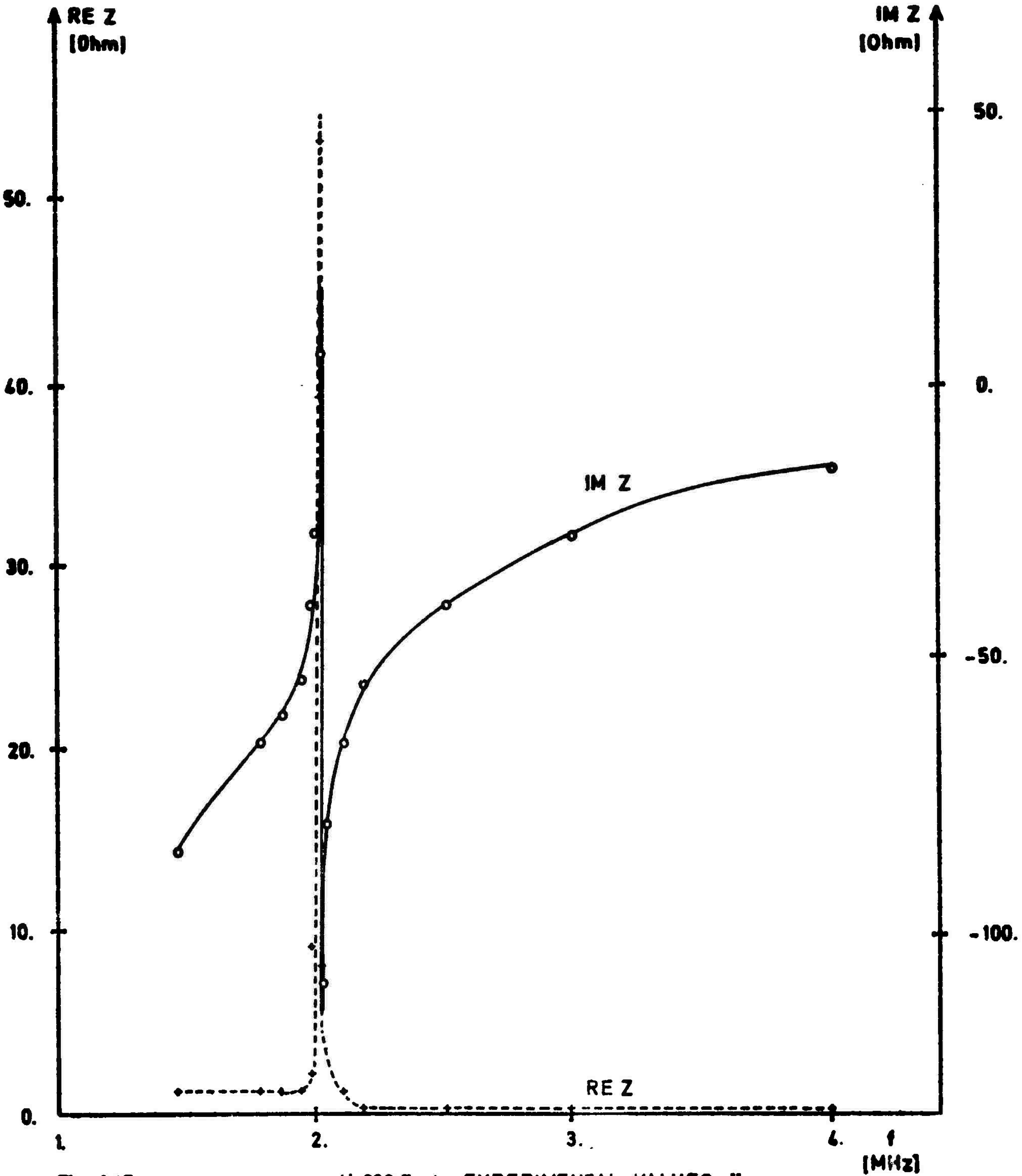

Fig. 1.15 H 328 Test : EXPERIMENTAL VALUES II

14-I

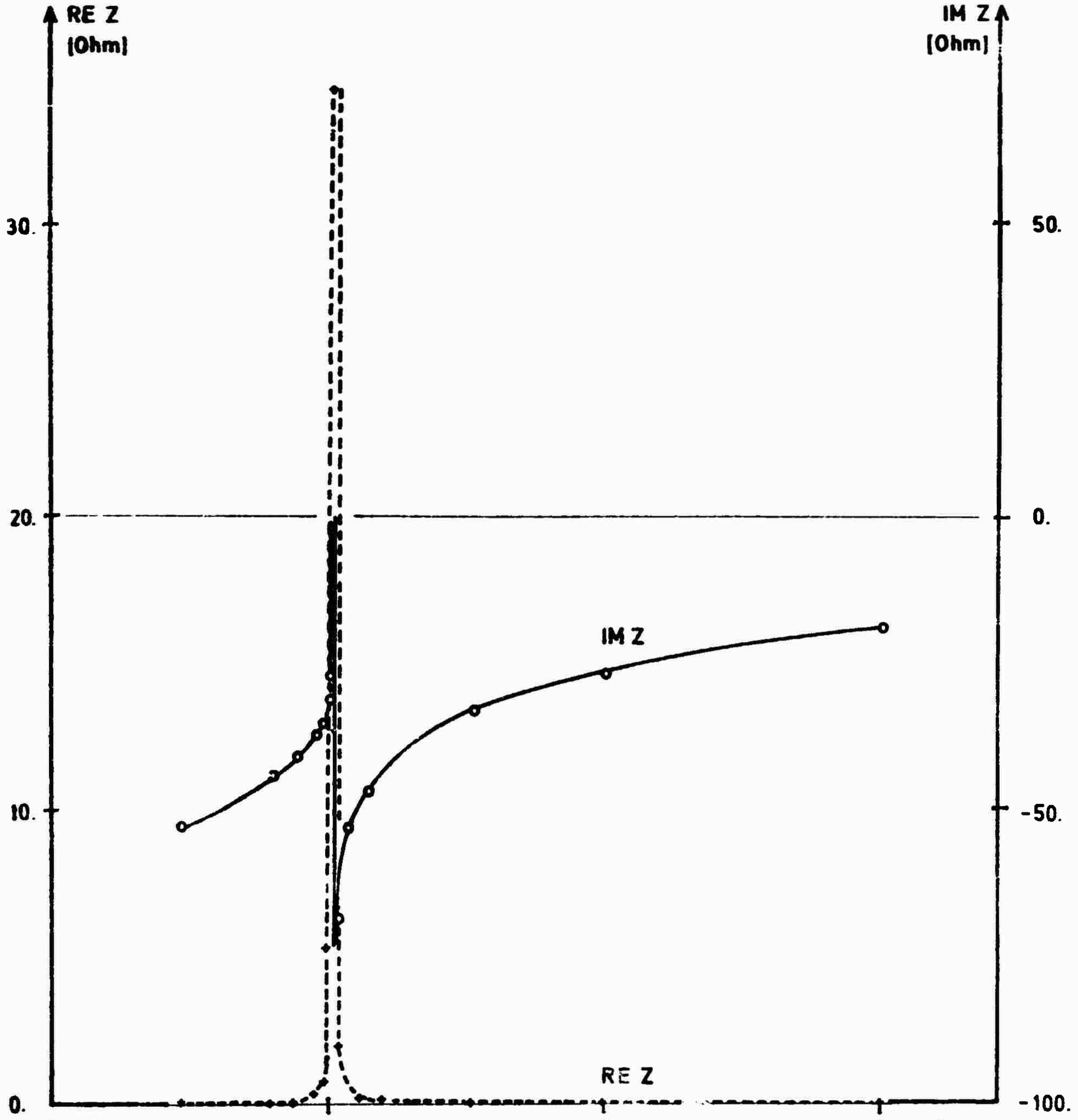

Fig. 1.16 H 328 Test : THEORETICAL VALUES II

Discussion of results

The deviations still appearing between experiment and theory can be explained on account of the following considerations:

1. The equivalent circuit diagram is calculated with a constant resistance R_{total} which, however, changes with frequency (skin-effect, dielectric losses). The influence of the surrounding medium on the eddy-current resistance is virtually incalculable.

2. Due to the high humidity in the mine the parameters R_{diel} and C change in a way not yet investigated (measurements in the mine have, however, among others the advantage of an essentially lower noise level!).

3. The parameters L, R, C, C_p cannot be calculated with the required accuracy (approximation formulas) because there are quantities (e.g. ε) that are not known exactly enough.

4. The calculation of RE Z (exp), IN Z (exp) is subject to an error of measurement, yet not exceeding 10 %.

The equivalent circuit diagram gives, however, a good interpretation of some effects, that have not been able to be cleared satisfactorily up to now:

1. In the equations of /1/ C_i is contained in the calculation of the series resonance frequency. This is, however, in variance with present experiments, where the decrease of C_i by raising the distance between the two inner windings has no influence on the series resonance. The equivalent circuit diagram shows definitely that C_i is only affecting the parallel resonance. This is proved by the experiment with the antenna H 328 II, with C_i

being artificially increased by parallelling a capacitor. The series resonance frequency remained constant whereas the parallel resonance approached the series resonance.

2. Body effect: The small static capacity C is essentially changed (increase of ε_r!) by approaching a hand especially at the two ends of the antenna, whereas it is relatively insensitive in the middle.

3. Influence of humidity: Water vapour deposits on the antenna on account of the high humidity thus influencing both loss resistance and capacity C. This gives a good explanation for the difficulties occurring with earlier experiments using wood as carrier material. Water-repellent materials such as epoxy, PVC etc. proved more favorable.

Finally the qualitative agreement of the impedance curve in experiment and theory can be regarded as best proof for the validity of the equivalent circuit diagram which, however, holds only in the range of the first (deepest) series and parallel resonances. At higher frequencies additional effects of the individual windings occur and the simple model described here fails.

Considerations on the efficiency of the antennas in air

According to /7/, the distant field of a small self-resonant helix with many windings may be regarded as a combination of an electric with a magnetic dipole. The length of the helix corresponds to the length of the electric dipole, the turn area corresponds to the magnetic dipole $n \cdot A = n \cdot r^2 \cdot \pi$.

For these dipoles the efficiency can be calculated with given radiation frequency (here the first resonance frequency) according to /5/:

$$\eta = \frac{P_{radiation}}{P_{rad} + P_{loss}} = \frac{I^2 R_{radiation}}{I^2 (R_{rad} + R_{loss})} \qquad (1.34)$$

As mentioned already the radiation resistance is smaller than the loss resistance by several decimal periods, so that R_{rad} can be neglected in the denominator:

$$\eta = \frac{I^2 R_{rad}}{I^2 R_{loss}} = \frac{R_{rad}}{R_{loss}} = \frac{P_{rad}}{R_{loss}} \qquad (1.35)$$

R_{rad} can be calculated according to Eqs. (1.29) and (1.30). Eqs. (1.34) and (1.35) are only valid with antenna dimensions $\ll \lambda$ (which is certainly the case for the antennas described). Table 1.7 gives a survey of these calculations for the antennas H 1136 Cull, H 328, and H 1136 in water.

Table 1.7

	R_{loss} Ω	R_e	η dB	R_m	η dB	f_{res} kHz
H 1136 Cull	400	$1.6 \cdot 10^{-3}$	-74	$40 \cdot 10^{-6}$	-70	220
H 328	40	0.24	-22	$5.6 \cdot 10^{-4}$	-48	2020
H 1136 Cull in water	35	$4.4 \cdot 10^{-8}$	-71	$2.8 \cdot 10^{-6}$	-89	1.1

Discussion: Antennas with a relatively low resonance frequency in air (e.g. H 1136, H 772) show a decrease of resonance frequency caused by a narrower winding and thus increased inductance. As regards efficiency these "inductive" antennas are by far less favorable than "capacitive" antennas as is shown in the table. Thus, for any application we have to make a compromise between antenna efficiency and favorable frequency for the transmission in the dissipative medium, which is thoroughly dealt with in /8/.

Propagation measurements

Diagram 1.17 shows the characteristic course of a propagation measurement. In this case, antenna H 1136 Cull was operated in water in the mine St. Gertraudi.

Curve a shows the curvature of field strength in dependence on the distance. The antenna was situated in the water-filled "Mabuse-gallery", measurements were executed along the west-gallery.

Measuring data of this experiment:

frequency $f = 1.1$ kHz
antenna current $I = 1$ A
applied power $P_i = 100$ W

Transmission was detected unobjectably in a distance of 1 km with a signal-to-noise-ratio of 7 dB. The components B_r, B_ϕ could be determined. B_θ vanished in the noise at greater distances.
This result indicates the predomination of the part of the electric dipole.

Stimulated by this experiment the same antenna was once more fed in water, this time, however, in a lower water-filled gallery near the VLF-laboratory. For this experiment, the VLF-transmitter (Savage) in the lab was used.

Measuring data of the experiment:

frequency $f = 1.1$ kHz
antenna current $I = 3.5$ A
applied power $P_i = 700$ W

The power could not be increased on account of sparkovers at the ends of the antenna that would surely have influenced the measurement.
Surprisingly, the signal was to be detected unobjectably even in a distance of more than 7 km on the earth surface.

18.9

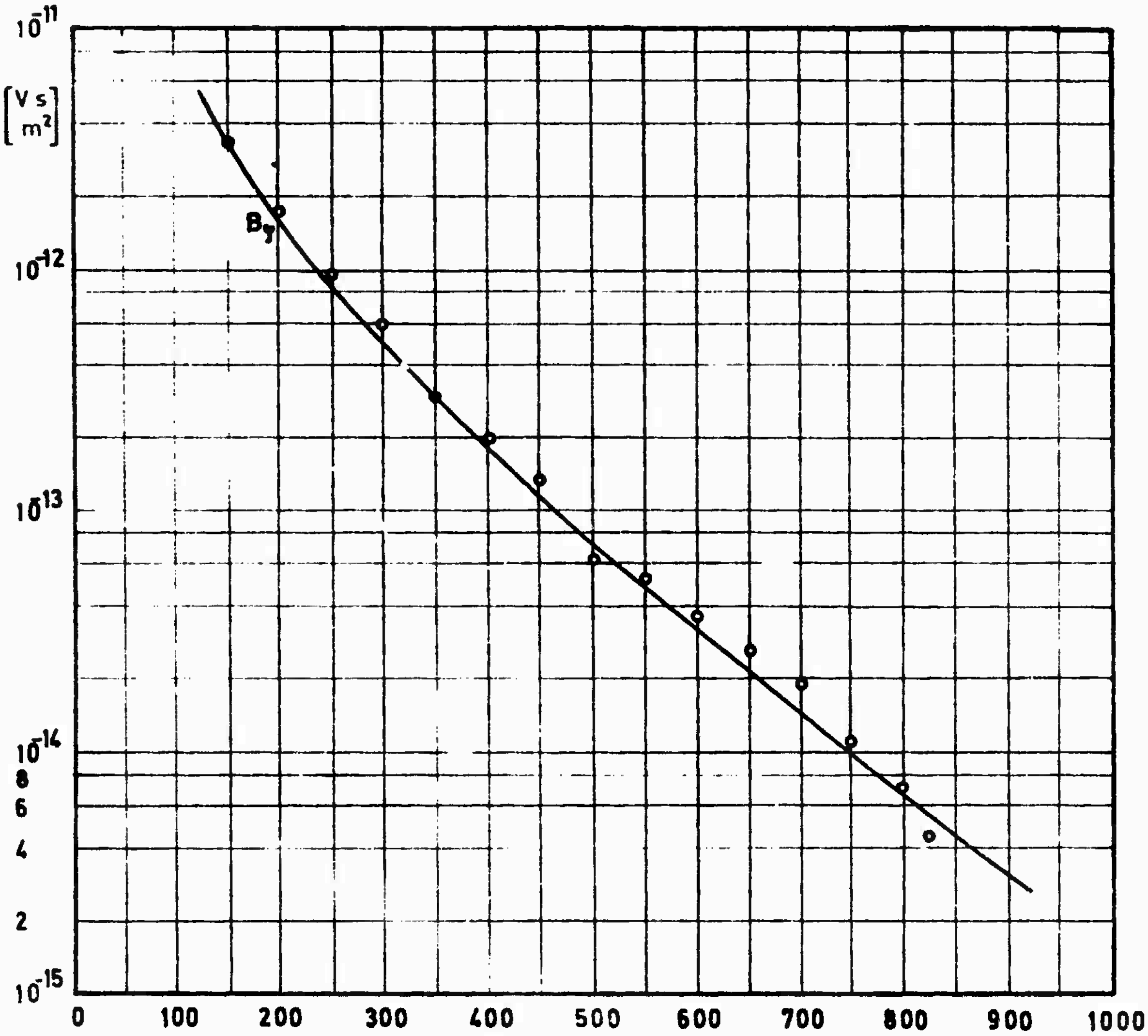

10^{-11}
$\left[\frac{V s}{m^2}\right]$
B_y
10^{-12}
10^{-13}
10^{-14}
8
6
4
2
10^{-15}
0
100
200
300
400
500
600
700
800
900
1000
r [m]

Fig.: 1.17

CHAPTER 2

MEASURING THE ROTARY FIELD ELLIPSE BY A FERRITE ROD ANTENNA - "PEDAL LOCUS CURVE"

In the magnetic alternating field a coil (frame) receives an e.m.f. being proportional to the area A, the number of turns n and the change velocity of the magnetic induction B, the latter being proportional to the projection of the field direction to the frame axis. The desired high e.m.f. is reached by a high μ of the ferrite material, filled into the coil and A. Technical problems restrict the two values. Comprehensive investigations /9/ showed the use of a ferrite rod to be optimal with the dimensions given. This ferrite rod coaxial to the receiving coil represents the coil axis and thereby the direction of the receiving antenna for all further considerations.

An alternating field constant in space induces an e.m.f. in the ferrite antenna according to

$$\text{e.m.f.}_{\text{ind.}}(t) = K \cdot B \sin\omega t \cos\psi \qquad (2.1)$$

K ... calibration factor, specific for electric and geometric properties of the ferrite antenna
ψ ... angle between ferrite rod and field direction

If the field consists not only of one vector, but is an elliptical field, then the projection of the instantaneous field vector on the antenna direction is a direct measure for the e.m.f.

2.1 Two-dimensional case

At first, the three-dimensional problem is confined to a two-dimensional one by moving the antenna only in the plane of the rotary field ellipse. Let the x-y plane of the coordinate system coincide with this plane.

It could be shown in /11/ that always only one planar ellipse will result, even if more than two components with different phase and direction in space are superposed.

On account of the continuous change of direction and value of the field vector the instantaneous vector in the antenna direction generally does not yield the maximum amount of projection and thus maximum e.m.f. In Fig. 2.1a the maximum e.m.f. is plotted as radius for each position of angle ψ of the receiving antenna (dashed curve "pedal locus curve") and reduced to the same scale the rotary field ellipse is plotted. It can be realized that always that point T of the ellipse produces one point of the pedal locus curve F in which a normal to the antenna direction contacts the ellipse.

In vector form the analytic description of this pedal locus curve measured in earlier studies /10,11/ reads as follows:

$$\vec{X}_F = \sqrt{a^2\cos^2\psi + b^2\sin^2\psi} \begin{pmatrix} \cos\psi \\ \sin\psi \end{pmatrix} \tag{2.2}$$

being the basis for further calculations.

Special cases:

For a = b (circular polarization)

$$\vec{X}_F = a \begin{pmatrix} \cos\psi \\ \sin\psi \end{pmatrix}$$

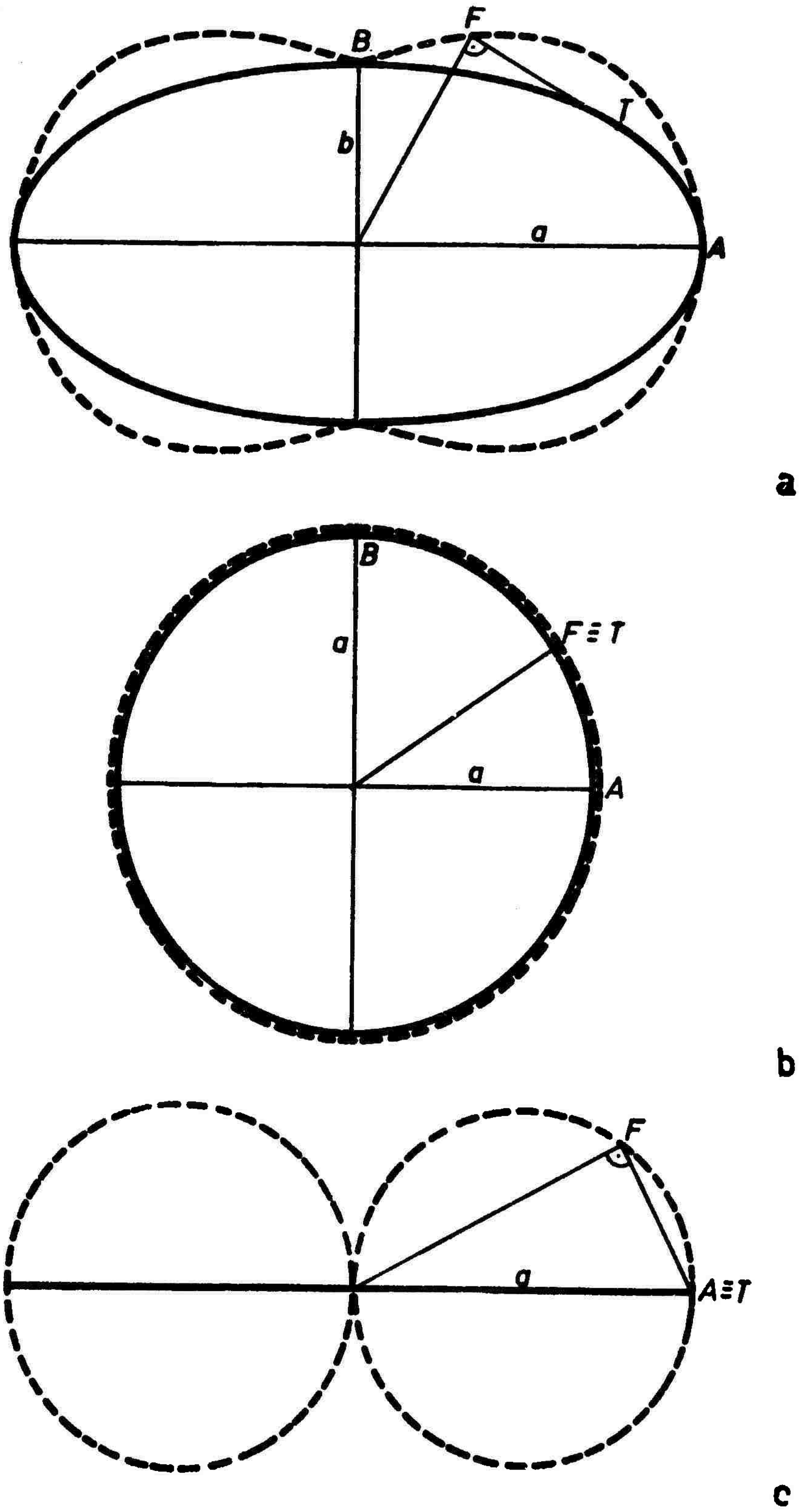

Fig . 2.1

or without parameter

$$x^2 + y^2 = a^2 \quad \text{(circle is counted twice)}$$

The receiving e.m.f. is independent on the direction (see Fig. 2.1b).

For b = 0 (linear polarization)

$$\vec{x}_F = a \cos\psi \begin{pmatrix} \cos\psi \\ \sin\psi \end{pmatrix}$$

or without parameter

$$x^2 + y^2 \pm ax = 0$$

and

$$(x \pm \frac{a}{2})^2 + y^2 = \frac{a^2}{4} \quad \text{(2 circles shifted by } \pm a/2 \text{ including the origin)}$$

in the standard form, resp., reflecting the figure-eight pattern of the pure cosine-dependency (see Fig. 2.1c).

2.2 Phase relation

Assuming linear polarization (only one vector instead of the rotary field ellipse) it becomes evident that the induced voltage U_{ind} is in phase with the alternating field, independently of the angle ψ between field vector and antenna direction (cf. Fig. 2.1c). If there exists a rotary field ellipse, each rotation of the instantaneous vector at the same time means a continuous phase rotation on 2π. With the phase position of the major axis of ellipse as zero point we measure a phase for each antenna direction corresponding precisely to that instantaneous vector that induces maximum amplitude into the antenna. With the exception of the case when the antenna is oriented in the main axes of the ellipse the phase of the e.m.f. in the antenna is not identical with the phase of the instantaneous vector in antenna direction.

Corresponding to the definition of the pedal locus curve, the phase-determining contact points T (cf. Fig. 2.1a) of the tangent lines normal to the antenna move close together near the major axis but move away from the minor axis. This means that the phase of <u>a</u> dominates in quite a large angular sector around A. In the neighborhood of B, however, the phase position changes much more than in A even at the same change of space angle. This is of great importance for the phase measurement described later on: the phase errors caused by errors of angular adjustment are lowest at maximum amplitude.

2.3 Technology of measurement

For measuring the rotary field ellipse, a ferrite antenna with Cardanic suspension is used. Fig. 2.2 shows the goniometer that had been used earlier and is described in /10/. This special construction allows to turn the top-most plane C (on which the ferrite rod is pivoted) into any direction. The scale has a reading accuracy of 1/2 degree.

If the position of the ellipse plane is known, e.g. let it be horizontal, a and b are comparatively easy to measure. The top-most plane of the goniometer is adjusted in the direction of the ellipse plane and the minimum and maximum voltages are measured. For determining the directions of a and b, "minimum" adjustment (= b) is preferred, yielding higher accuracy (cf. Fig. 2.1a).

It is much more difficult to measure the rotary field ellipse if the latter is oriented arbitrarily in space, orientation being unknown.

There are five independent, unknown quantities to be determined:

Orientation of ellipse plane in space	2 angles
Orientation of the major (or minor) axis in the ellipse plane	1 angle
Size of axes	2 voltages

In /10/, two different methods were developed for measuring these quantities by means of the goniometer.

Assumption for method 1: When rotating the ferrite rod in a plane arbitrarily inclined to the ellipse the minimum reception voltage always occurs in the plane normal to $\underline{a}$, i.e., the plane given by the z-axis and the minor axis b. Proceeding on this assumption the 5 desired quantities can be measured as follows in 5 definite steps (cf. Fig. 2.2).

1. Starting position: plane A horizontal, plane B in
   northern direction ⟹ $\alpha = 0^{\circ}$, $\gamma = 0^{\circ}$,
   ferrite rod in plane B
2. $\beta = 0^{\circ}$, $\gamma = 90^{\circ}$, turn α as far as $U_{ind} = \min$; fix $\underline{\alpha}$
3. $\gamma = 0^{\circ}$, turn β as far as $U_{ind} = \min$; fix $\underline{\beta}$
4. Turn γ as far as $U_{ind} = \min \Longrightarrow \underline{U_3}$, $\underline{\gamma}$
   The angles α, β, γ resulting therefrom are listed.
5. $\gamma \pm 90^{\circ}$, $U_{ind} \Longrightarrow \underline{U_2}$
6. $\gamma = 0^{\circ}$, $\beta \pm 90^{\circ}$, $U_{ind} \Longrightarrow \underline{U_1}$

U_1 ... proportional to major axis a
U_2 ... proportional to minor axis b
U_3 ... should be zero (noise level)

A correction of the angles α or β for an accurate adjustment of U_3 can be done after step 4. The minimum voltage U_3 must be as small as possible compared to U_1 thereby constituting a measure for the accuracy of the angular measurement.

As is shown in the following calculation, the basic assumption for method 1 only yields an approximation that is fulfilled the better the narrower the allipse, i.e. the higher the ratio a/b and the smaller the inclination of the ellipse plane to the horizontal one from which the measurement starts.

Method 2 is based on the fact that there is always one space direction where an absolute minimum of reception voltage can be measured: the normal to the ellipse (z-direction) which is reached within several steps of asymptotic adjustment. If the normal to the ellipse and thus the position of the ellipse plane is determined, subsequent measurements are performed as described earlier.

Method 2 is always successive except for b = 0 and will be preferred in such cases where method 1 delivers inaccurate results.

With method 1 being technologically much more favorable (5 definite steps of adjustment on the one hand, asymptotic finding of the first adjustment on the other hand), an antenna pattern is first measured in the horizontal plane. Assuming random position in space of the rotary field ellipse, the horizontal pattern means an inclined, plane, central section through the pedaloid.

For the mathematical description of this measuring technology a detailed calculation of receiving characteristics is necessary. In the general case, the basic element of the curves and surfaces listed in the following is the ellipse.

24-9

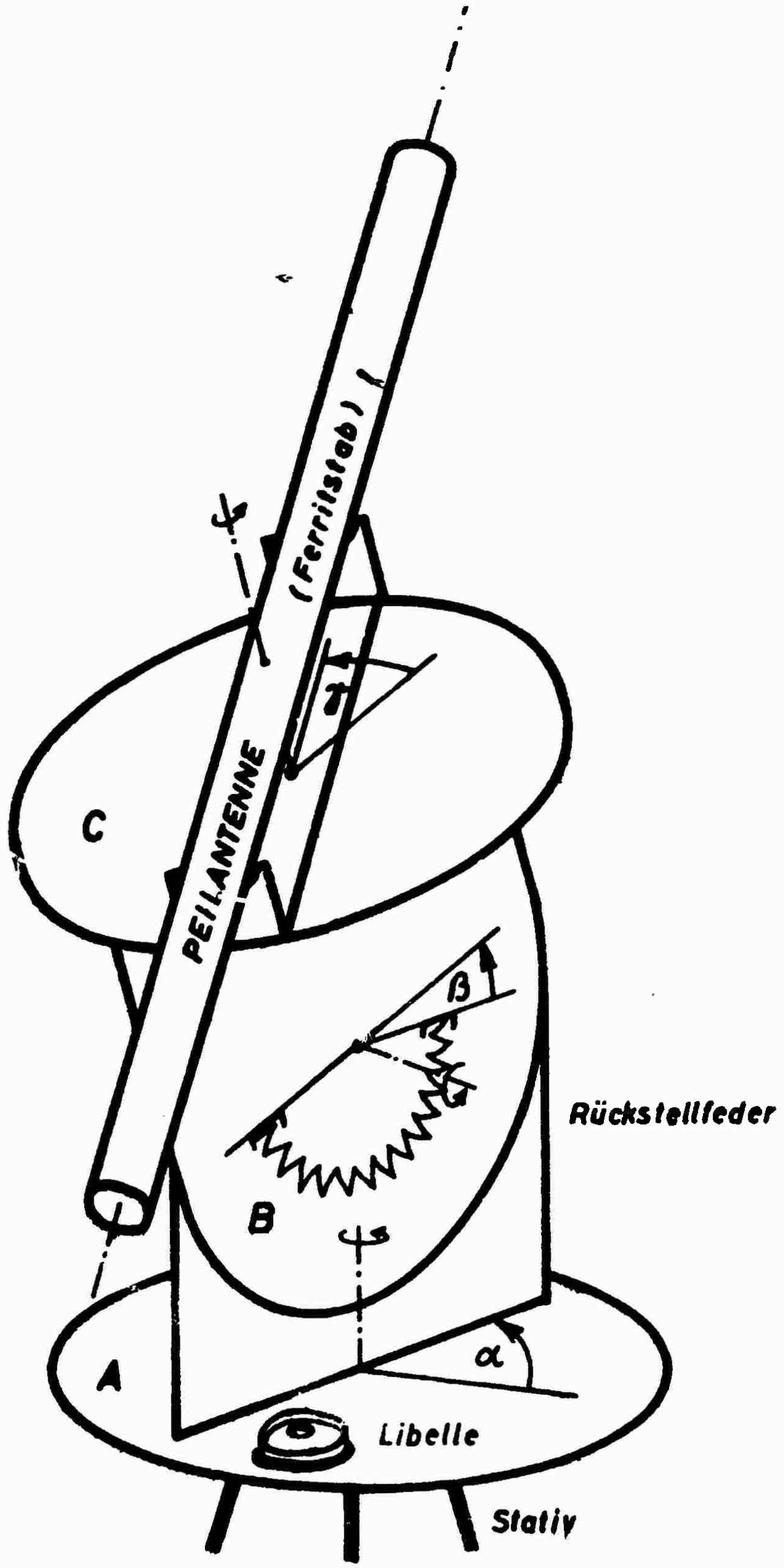

Peilkopf (schematisch)

Empfangsantenne FA6

Fig.: 2 2

2.4 Pedal locus curve of the ellipse

General definition for a pedal locus curve (cf. /12/):

The pedal locus curve of a given curve related to a pole O is the geometrical locus of the pedal loci F of those perpendicular lines that can be dropped from O on to the tangents of the curve.

Examples:

a) cardioid - pedal locus curve of the circle for one of its points on the periphery as a pole (Fig. 2.3a)

b) lemniscate or figure-of-eight curve - pedal locus curve of an equilateral hyperbola with the center as a pole (Fig. 2.3b).

For the ellipse the pedal locus curve takes the form as is illustrated in Fig. 2.3c with the center as a pole.

Two essential features are

1. that the pedal locus curve differs the less from its ellipse the more circular the latter becomes, and
2. that the pedal locus curve contacts the ellipse in the end points of the major and minor axes.

From the parametric representation in Eq. (2.2) the arbitrary radius r_p of the pedal locus curve can be derived. This calculus was done by /13/ and /14/.

$$r_p = \sqrt{a^2\cos^2\alpha + b^2\sin^2\alpha} = \sqrt{\frac{a^2+b^2}{2} \quad \frac{a^2-b^2}{2}\cos 2\alpha} \tag{2.3}$$

Therefrom, the parameter-free representation of the pedal locus curve (Fig. 2.3c) in Cartesian coordinates can be derived:

$$a^2x^2 + b^2y^2 = (x^2+y^2)^2 \tag{2.4}$$

2.5 The triaxial pedaloid

constitutes the three-dimensional counterpart to the pedal locus curve of the ellipse and can be derived from the ellipsoid on account of the definition of the pedal locus curve.

The derivation of the parameter-free representation of the pedaloid is done in the same way as with the ellipsoid, i.e., in the arbitrary radius of the pedaloid

$$r_{ped} = \sqrt{r_p^2 \cos^2\beta + c^2 \sin^2\beta} \qquad (2.5)$$

r_p is substituted by Eq. (2.3) and the angular functions by the relations mentioned above. The following equation results:

$$a^2x^2 + b^2y^2 + c^2z^2 = (x^2 + y^2 + z^2)^2 \qquad (2.6)$$

Special case 1:

revolution pedaloid - it develops by rotating a pedal locus curve of an allipse e.g. on its major axis. Since $b = c$ in this case,

$$a^2x^2 + b^2(y^2 + z^2) = (x^2 + y^2 + z^2)^2 \qquad (2.7)$$

is valid.

Note: Pedaloid and revolution pedaloid occur in optics at the description of the double refraction of the light. The ray surface or wave surface of the extraordinary ray is a (revolution) ellipsoid. To be able to apply SNELLIUS' law of refraction for this extraordinary ray, the term "wavelength standard velocity" is introduced instead of "ray velocity", which is no longer equal to the amount of the radius of the (revolution) ellipsoid but equal to the amount of the radius of the pertinent (revolution) pedaloid.

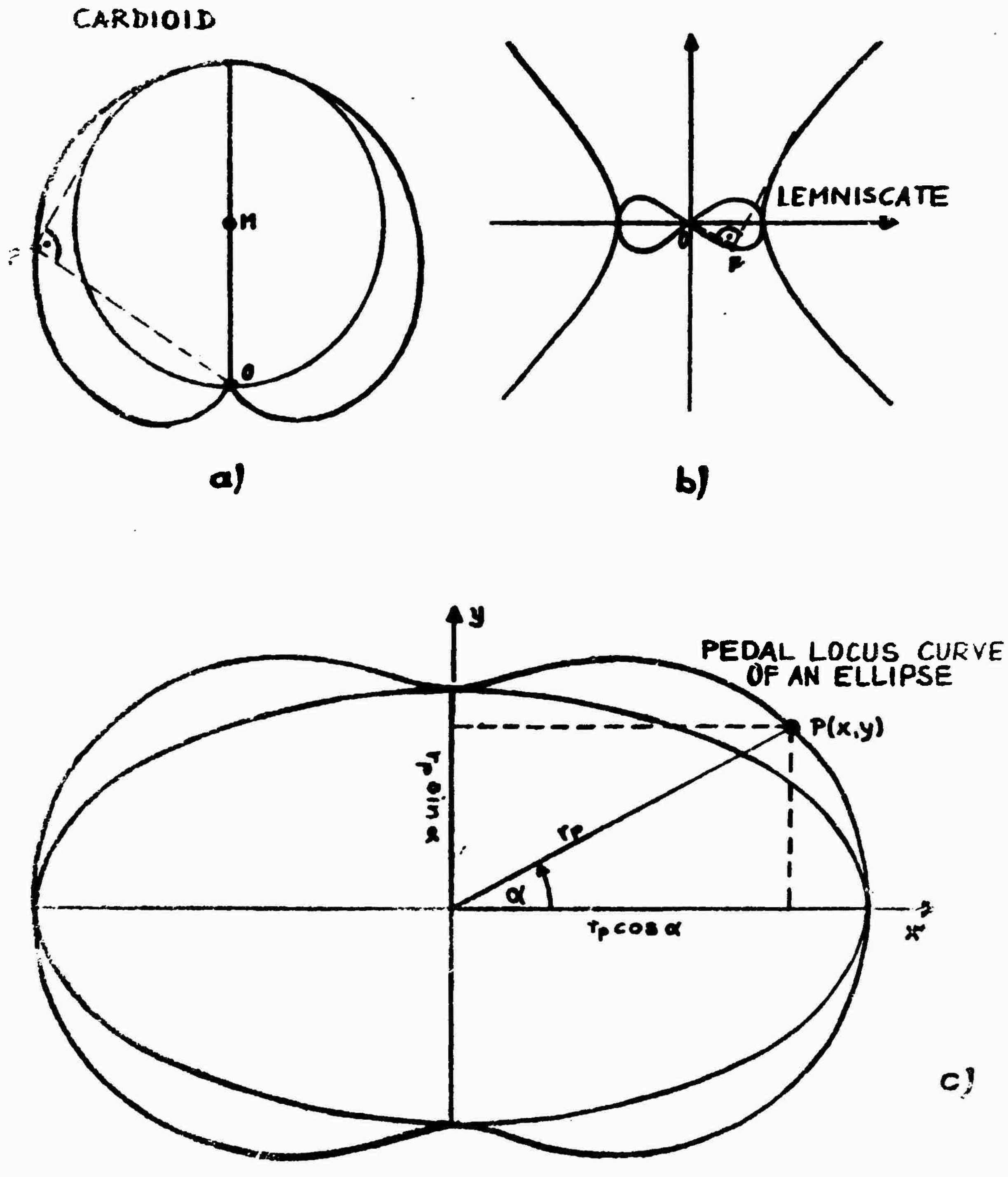
CARDIOID
M
O
P
LEMNISCATE
O
F
a)
b)
y
PEDAL LOCUS CURVE
OF AN ELLIPSE
P(x,y)
r_p
$r_p \sin \alpha$
α
$r_p \cos \alpha$
x
c)

FIG.23

In /15/ formula (2.7) is quoted and the surface is termed "(revolution) ovaloid", the pedal locus curve of the ellipse is termed "oval", since in the above mentioned case of double refraction, the axes of the ellipse etc. differ only slightly. The shape of the pedal locus curve of the ellipse deviates only slightly from that of an ellipse, that is why this term ovaloid is used.

Special case 2:

sphere - if all three axes are equal, i.e., $a = b = c$, both the ellipsoid and the triaxial pedaloid become spheres.

If the passage to the limit $c \to 0$ is affected, the ellipsoid degenerated to its main sectional ellipse.

2.6 The (true) pedaloid

When keeping to this systematic mathematical classification the receiving characteristic in the elliptically polarized field can be interpreted as being the degenerate case of a triaxial pedaloid by setting the third axis $c = 0$. In contrast to the ellipsoid, the three-dimensional character of the formation thereby developing is preserved in this case.

The parameter-free representation can be obtained quite similarly to that of the ellipsoid. The arbitrary radius r_{pe} results from the radius of the pedal locus curve r_p (cf. Eq. (2.3)) by multiplying by the cosine of the angle of elevation β

$$r_{pe} = r_p \cos\beta = \sqrt{a^2\cos^2\alpha + b^2\sin^2\alpha} \cdot \cos\beta \qquad (2.8)$$

By substituting the angular functions as mentioned before the equation of the (true) pedaloid

$$a^2x^2 + b^2y^2 = (x^2 + y^2 + z^2)^2 \qquad (2.9)$$

is obtained which is most important for measurements in the elliptically polarized field. The families of pedaloids are listed in Fig. 2.4.

Special case:

Circular ring (torus) with the inner radius being zero; occurs with circular polarization of the field (a = b). Eq. (2.9) then reads

$$a^2(x^2 + y^2) = (x^2 + y^2 + z^2)^2 \qquad (2.10)$$

The arbitrary radius r_{tor}

$$r_{tor} = a \cdot \cos \beta \qquad (2.11)$$

Degenerate case:

Double sphere - representing the three-dimensional receiving characteristic in the linearly polarized field. On account of b = 0, its equation reads

$$ax = x^2 + y^2 + z^2 \qquad (2.12)$$

The arbitrary radius

$$r_{ds} = a \cos \alpha \cdot \cos \beta \qquad (2.13)$$

2.7 Intersection of the pedaloid with a plane

Owing to the measuring technique it is important to know the sections of the pedaloid involved. To find them, a new coordinate system x', y', z' is introduced resulting

THE FAMILIES OF ELLIPSOIDS

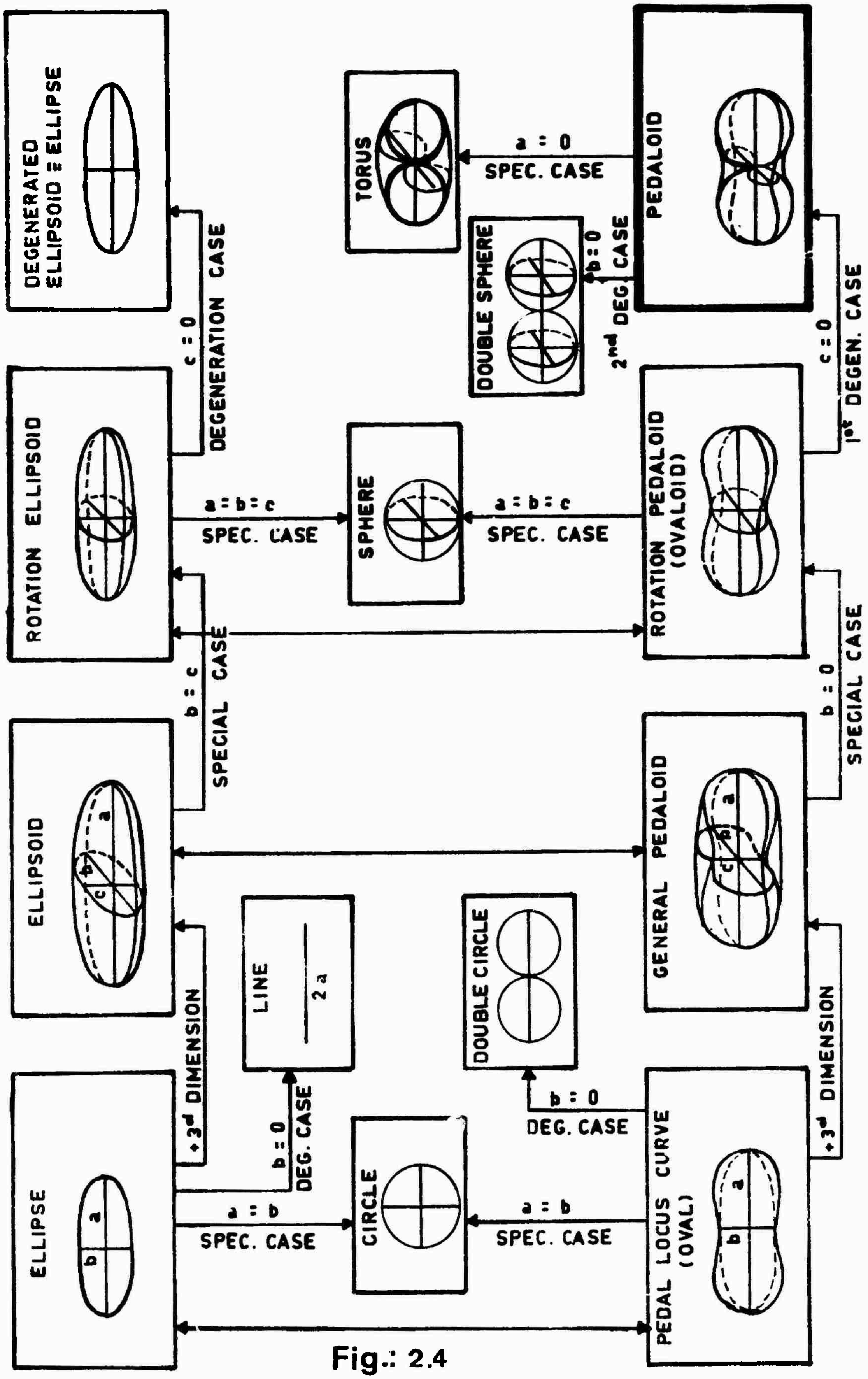

Fig.: 2.4

from the original one by successive rotation by the angles u, v, w (Eulerian angles). The origin remains constant. Setting z' = 0, we obtain the cross-sectional area lying in the plane (x', y').

The following equation describes this rotation

$$\vec{r} = a_{ik}\vec{r}' \qquad \vec{r} = (x, y, z) \quad \vec{r}' = (x', y', z') \tag{2.14}$$

$\vec{r}$ and $\vec{r}'$ are position vectors. The elements of the matrix a_{ik} are the direction cosines and read

$$\begin{aligned}
a_{11} &= \cos v \cdot \cos w \\
a_{12} &= -\cos u \cdot \sin w \\
a_{13} &= \sin v \\
a_{21} &= \cos u \cdot \sin w + \sin u \cdot \sin v \cdot \sin w \\
a_{22} &= \cos u \cdot \cos w - \sin u \cdot \sin v \cdot \sin w \\
a_{23} &= -\sin u \cdot \cos v \\
a_{31} &= \sin u \cdot \sin w - \cos u \cdot \sin v \cdot \cos w \\
a_{32} &= \sin u \cdot \cos w + \cos u \cdot \sin v \cdot \sin w \\
a_{33} &= \cos u \cdot \cos v
\end{aligned} \tag{2.15}$$

In Eq. (2.9) x, y, z are substituted by x', y', z'. On account of the above relation the pedaloid in the dashed coordinates is obtained:

$$\begin{aligned}
&a^2(a_{11}x' + a_{12}y' + a_{13}z')^2 + b^2(a_{21}x' + a_{22}y' + a_{23}z')^2 = \\
&= \left[(a_{11}x' + a_{12}y' + a_{13}z')^2 + (a_{21}x' + a_{22}y' + a_{23}z')^2 + \right. \\
&\left. + (a_{31}x' + a_{32}y' + a_{33}z')^2\right]^2
\end{aligned} \tag{2.16}$$

Since only the intersection is of interest here, z' = 0. By squaring the brackets in Eq. (2.16) we obtain

$$a^2(a_{11}^2x'^2 + 2a_{11}a_{12}x'y + a_{12}^2y'^2) + b^2(a_{21}^2x'^2 + 2a_{21}a_{22}x'y' + a_{22}^2y'^2) = |(a_{11}^2 + a_{21}^2 + a_{31}^2)x'^2 + (a_{12}^2 + a_{22}^2 + a_{32}^2)y'^2 + 2(a_{11}a_{12} + a_{21}a_{22} + a_{31}a_{32})x'y'|^2 \tag{2.17}$$

If the left side is rearranged and if we further consider on the right side that the sum of the squares of the direction cosines is equal to 1 and the sum of the composite products is equal to zero, we obtain

$$(a^2a_{11}^2 + b^2a_{21}^2)x'^2 + (a^2a_{12}^2 + b^2a_{22}^2)y'^2 + 2(a^2a_{11}a_{12} + b^2a_{21}a_{22})x'y' = (x'^2 + y'^2)^2 \tag{2.18}$$

This equation again represents a pedal locus curve of an ellipse in relation to the coordinate system x', y'. On account of the term with the composite elements, major and minor axes of the pedal locus curve are not lying in the direction of the coordinate axes. The sections on the x' and y' axes are

$$A' = \sqrt{a^2a_{11}^2 + b^2a_{21}^2} \quad \text{and} \quad B' = \sqrt{a^2a_{12}^2 + b^2a_{22}^2} \tag{2.19}$$

Proceeding from the general equation of sections (2.18) the various special cases can be derived.

Special case 1: (plane vertical to main pedal locus curve)

a) plane vertical to the original pedal locus plane through the major axis a, u = 90°, v = 0°

Note: Rotation by the two angles u and v is sufficient to reach any desired direction in space. The matrix of rotation is simplified to a 2 x 2 matrix: the angular functions for w = 0 must be equal to 1 or 0.

The matrix of rotation therefore reads

$$a_{ik} = \begin{Vmatrix} 1 & 0 \\ 0 & 0 \end{Vmatrix} \tag{2.20}$$

Eq. (2.18) is reduced to

$$ax' = x'^2 + y'^2 \qquad \text{or} \qquad y'^2 = ax' - x'^2 \tag{2.21}$$

which is well known to be the vertex equation of the circle with the radius a/2, where x' is pointing into the direction of x and y' into that of z.

b) plane vertical through minor axis b, $u = 0^\circ$, $v = 90^\circ$

$$\text{matrix} \qquad a_{ik} = \begin{Vmatrix} 0 & 0 \\ 0 & 1 \end{Vmatrix} \tag{2.22}$$

In this case,

$$by' = x'^2 + y'^2 \qquad \text{or} \qquad x'^2 = by' - y'^2 \tag{2.23}$$

is the vertex equation of the circle with the radius b/2, where x' is pointing into the direction of z and y' into that of y.

c) arbitrary plane vertical to main pedal locus curve, $u = 90^\circ$, $0 < v < 90^\circ$

$$\text{matrix} \qquad a_{ik} = \begin{Vmatrix} \cos v & 0 \\ \sin v & 0 \end{Vmatrix} \tag{2.24}$$

yields

$$y'^2 = x'\sqrt{a^2\cos^2 v + b^2\sin^2 v} - x'^2 \tag{2.25}$$

The radical represents the radius of the intersected pedal locus curve and is equal to the diameter of the vertex circle represented by Eq. (2.25).

<u>Result from 1 a) - c):</u> All surfaces of intersection vertical to the main pedal locus curve of the pedaloid are vertex circles in relation to the center of the pedaloid.

<u>Special case 2:</u>

Intersections through the minor axis b, $u = 0^\circ$, $0 < v < 90^\circ$

$$\text{matrix} \qquad a_{ik} = \begin{Vmatrix} \cos v & 0 \\ 0 & 1 \end{Vmatrix} \qquad (2.26)$$

We obtain the pedal locus equations

$$a^2 a_{11}^2 x'^2 + b^2 y'^2 = (x'^2 + y'^2)^2 \qquad (2.27)$$

The condition $a_{11} = \cos v = b/a$ yields a circle with the radius b as surface of intersection.

<u>Proof:</u>

$$a^2 \frac{b^2}{a^2} x'^2 + b^2 y'^2 = (x'^2 + y'^2)^2$$

$$b^2 (x'^2 + y'^2) = (x'^2 + y'^2)^2$$

$$x'^2 + y'^2 = b$$

If $\cos v < \frac{b}{a}$, $b > a^2 a_{11}^2$ and forms the major axis of the curve of intersection which is again a pedal locus curve.

Special case 3:

Intersections through the major axis a, $0 < u < 90^\circ$, $v = 0^\circ$

$$\text{matrix} \qquad a_{ik} = \begin{Vmatrix} 1 & 0 \\ 0 & \cos u \end{Vmatrix} \qquad (2.28)$$

We obtain the pedal locus equation

$$a^2 x'^2 + b^2 a_{22}^2 y'^2 = (x'^2 + y'^2)^2 \qquad (2.29)$$

Summarizing the following characteristic properties of the pedaloid can be given:

1. The main intersection (containing the axes a and b of the ellipse) is the pedal locus curve with the largest area.
2. The radius vector vertical through the center 0 of the main intersection is equal to zero.
3. All intersections vertical to the main pedal locus surface have the shape of a figure eight. The largest area of this kind occurs at the intersection containing the major axis a, the smallest area arises at the intersection containing the minor axis b.
4. That intersection area that contains the minor axis and is inclined to the main pedal locus curve by the angle v, so that
   $$\cos v = a/b$$
   is valid, is a circle with the radius $r_{pe} = b$.

2.8 Calculation of the squint at polarization ellipses lying arbitrarily in space

If the polarization ellipse is not lying in the horizontal plane of measurement and if the direction finder for the detection of the maximum and minimum of field strength is rotated only in this plane, a specific error of measurement arises which can be determined by the following extreme value problem.

If the coordinate system in which the major axis of the pedaloid is pointing in the direction of the x-axis and the minor axis in y-axis direction, is revolved on the x-axis by the angle u and consequently on the new y_1-axis by the angle v, any arbitrary intersection area can be obtained as x'y'-plane. Let this intersection area of the pedaloid be the pedal locus curve measured horizontally; the question arises, what size the angle w must assume to make the newly developed axes x' and y' point in the directions of a' and b', respectively; a' and b' are the major and minor axes of the pedal locus curve in the intersection. This angle w is at the same time that squint that is made with the above described direction finding.

Proceeding from the equation of the pedaloid in the dash system, the coefficient of x' giving the length of the section A' on the x'-axis reads as follows:

$$\begin{aligned} A' &= (a^2 a_{11}^2 + b^2 a_{12}^2) = \\ &= a^2 \cos^2 v \cdot \cos w + b^2 (\cos^2 u \cdot \sin^2 w + \\ &+ \sin^2 u \cdot \sin^2 v \cdot \cos^2 w + \sin u \cdot \cos u \cdot \sin v \cdot \sin 2w) \end{aligned} \tag{2.30}$$

The derivation with respect to w is formed and set zero resulting

$$\frac{\sin 2w}{\cos 2w} = \tan 2w = \frac{\sin 2u \cdot \sin v}{\frac{a^2}{b^2}\cos^2 v + \sin^2 u \cdot \sin^2 v - \cos^2 u} \tag{2.31}$$

BEARING ERROR W

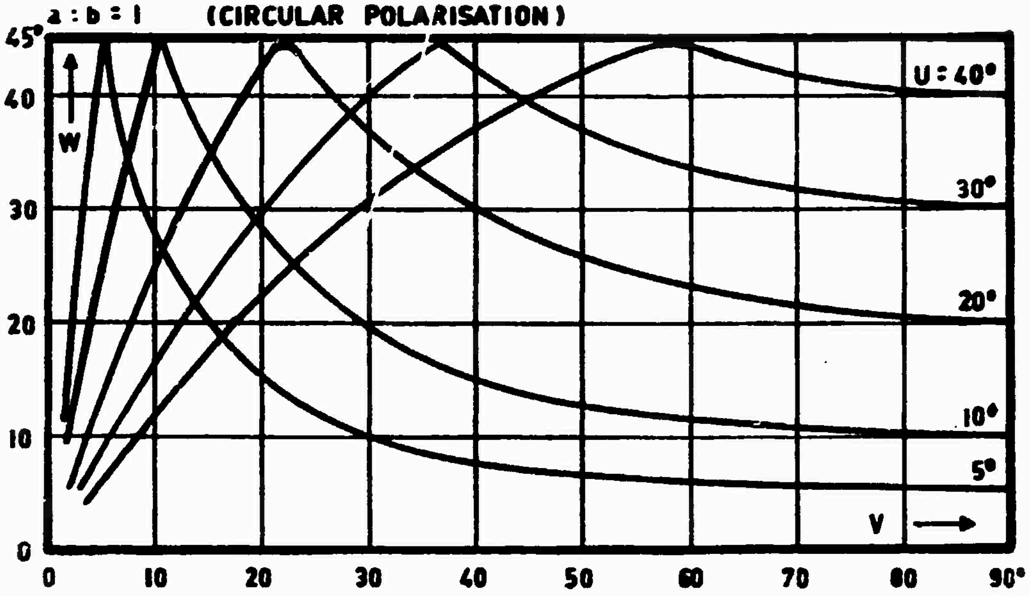

FIG. 2.5

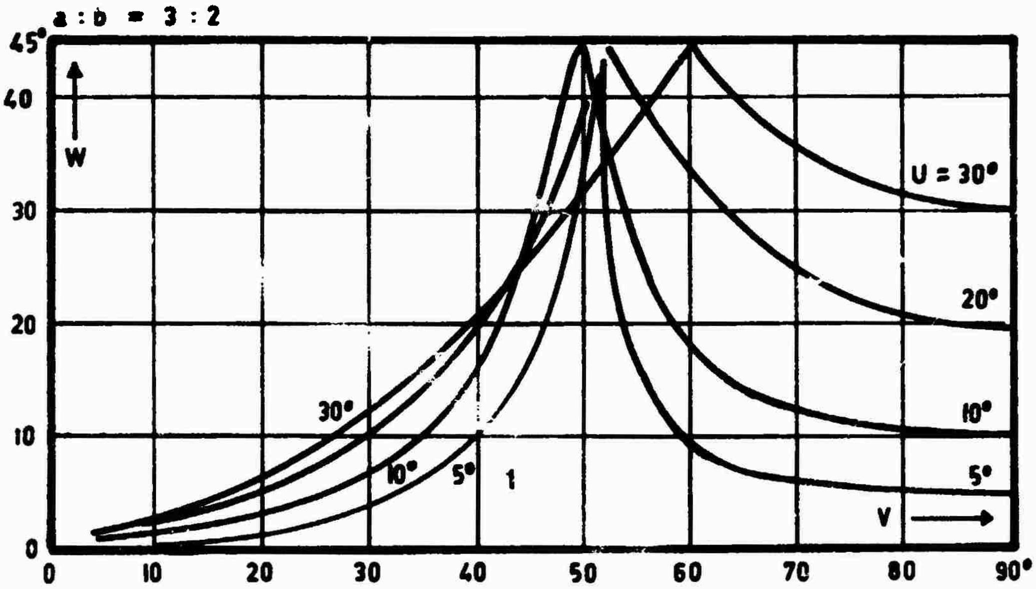

FIG. 2.6

BEARING ERROR W

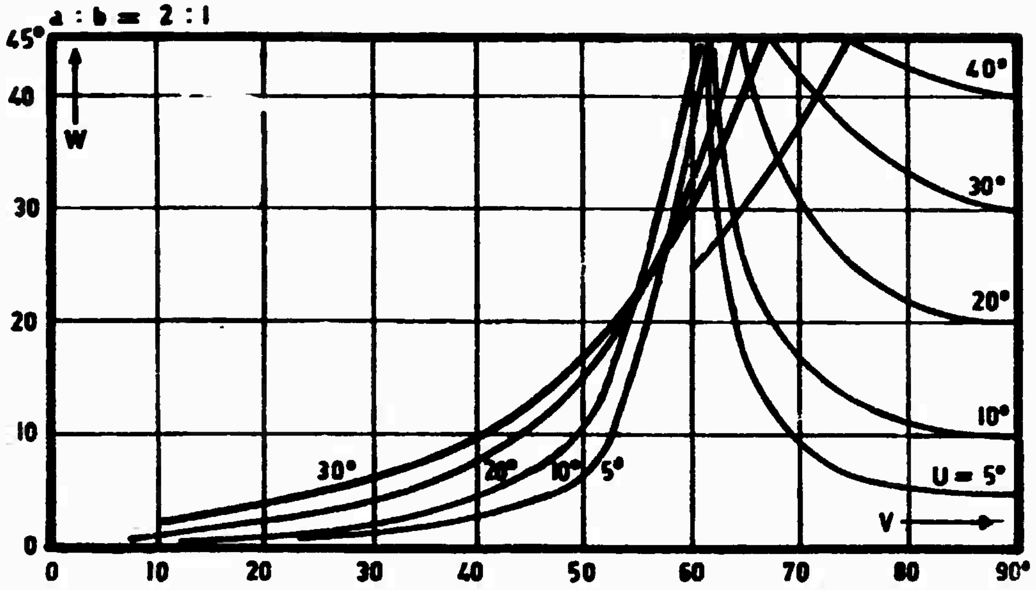

FIG. 2.7

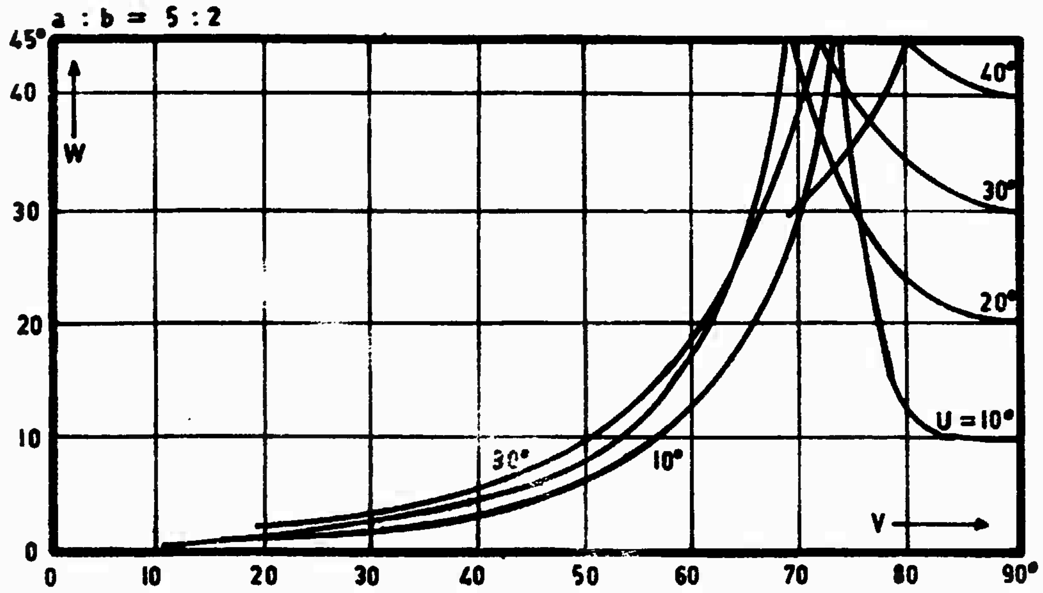

FIG. 2.8

For a check the angle obtained from the above equation can be inserted into the coefficient of the "term of rotation" of Eq. (2.18) which then has to vanish. The easier way is to set the coefficient C' of the term of rotation equal to zero and calculate w therefrom and compare it with the above result proving it.

The angle w was consequently computed for the following parameters:

Q (= a : b) = 1; 1.5; 2; 2.5; 3; 3.5; 4; 4.5; 5

$$\left.\begin{matrix} u \\ v \end{matrix}\right\} = 1, 2, 3, 4, 5, 6, 7, 8, 9, 10, 20, 30, \ldots, 80^{\circ}$$

The results are represented graphically in Figs. 2.5 - 2.8 for different ratios of axis a : b of the polarization ellipse. Fig. 2.5 is valid for a circularly polarized field (a = b). From the other diagrams it is to be seen that only for great angles u and v the squint is essential, e.g. for $u = v = 30^{\circ}$, $w = 12^{\circ}$ (a : b = 3 : 2), cf. Fig. 2.6. For ellipses with a smaller ratio of axes this squint becomes less important. Fig. 2.8 shows that a distortion of the ellipse $u = v = 30^{\circ}$ yields the negligible angle $w = 4^{\circ}$.

2.9 Conclusions

With the mathematical representation of the receiving characteristic in an elliptically polarized electromagnetic field (= pedaloid) it is possible to calculate every arbitrary section plane of this pedaloid. This fact involved many advantages for field strength measurements. One of the most important things is that we are able to calculate the squint that arises when the direction finder is rotated only in the horizontal plane when measuring the maximum, the polarization ellipse, however, lies arbitrarily in space.

CHAPTER 3

A NEW METHOD TO DETERMINE THE SPATIAL POSITION OF THE MAGNETIC ROTARY FIELD ELLIPSE

3.1 Introduction

For many experiments concerning VLF-reception it is necessary to know the exact position of the rotary field ellipse. N. NESSLER described a method to determine the pedaloid in his thesis /10/. This method, however, showed to be time-wasting and in some cases unexact; the error made by this method is calculated by R. Klein /16, 17/. The problem was to find a new method using all characteristics of the pedaloid for a better and non-subjective calculation. All the quantities of the rotary field ellipse had to be measured by means of an antenna system constant in space instead of using the direction finding antenna of former experiments.

3.2 The pedaloid

The measurement of a rotary field ellipse always leads to "pedal locus curves" when using ferrite-rod direction finding antennas.

Let us now briefly consider this effect mathematically:

a ... maximum voltage - major axis
b ... minimum voltage - minor axis
ω ... angular frequency
ϕ ... angle of inclination between major axis and antenna
θ ... angle between the normal of the ellipse plane and the antenna

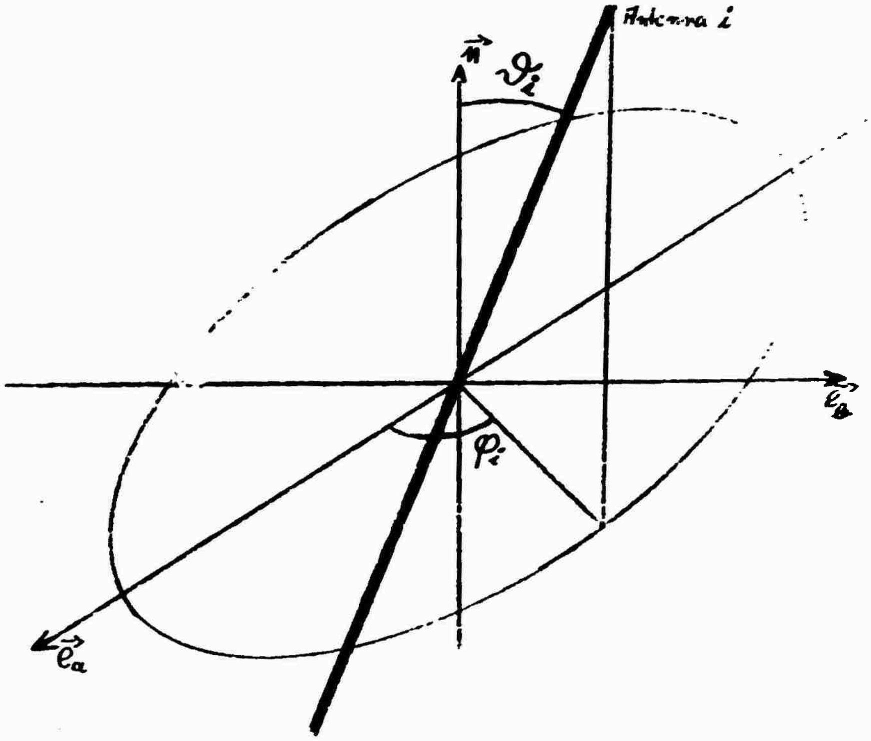

Fig. 3.1

The voltage induced into an antenna in dependence on ω, ϕ, and θ is given by

$$U = (a\cdot\cos\phi\cdot\cos\omega t + b\cdot\sin\phi\cdot\sin\omega t)\sin\theta \qquad (3.1)$$

with a and b containing all conversion factors between magnetic field strength and voltage.

The temporal maximum (minimum) of the voltage is reached when

$$\left.\frac{dU}{dt}\right|_{t=t_o} = 0 = \omega(-a\cdot\cos\phi\cdot\sin\omega t_o + b\cdot\sin\phi\cdot\cos\omega t_o)\sin\theta \qquad (3.2)$$

resulting

$$\frac{b}{a}\cdot\tan\phi = \tan\omega t_o \qquad (3.3)$$

Which further on will be referred to as "pedaloid-condition".

It can be seen that the phase angle relative to the major axis is not identical with the spatial angle, except for the case a = b. And the antenna does not reproduce the ellipse, but a pedal locus curve or a pedaloid.

3.3 Theory of the new method

The antenna combination consists of three electrically identical ferrite-rod antennas perpendicular to one another thereby forming an orthogonal trihedral. The three axes of the pedaloid are represented by the vectors $\vec{e}_a$, $\vec{e}_b$, and $\vec{n}$, with the subscripts a and b standing for the major and minor axes of the ellipse, respectively, and n being the normal vector of the rotary field ellipse. The arbitrary position of the rotary field ellipse in respect to an other Cartesian system is given by the three Eulerian angles ϕ, ψ, θ. Besides, two more unknown quantities are requested for a complete description of the ellipse in space, namely the two main voltages of the ellipse. If we succeed in measuring these five quantities position and size of the ellipse arbitrary in space are definitely determined.

3.4 Calculation

Fig. 2 shows the normal of the ellipse in reference to the antenna system.

Let the directions of the antennas be $\vec{i}$, $\vec{j}$, and $\vec{k}$, the following conditions can be calculated (antenna directions expressed by direction cosines in respect to $\vec{e}_a$, $\vec{e}_b$, and $\vec{n}$):

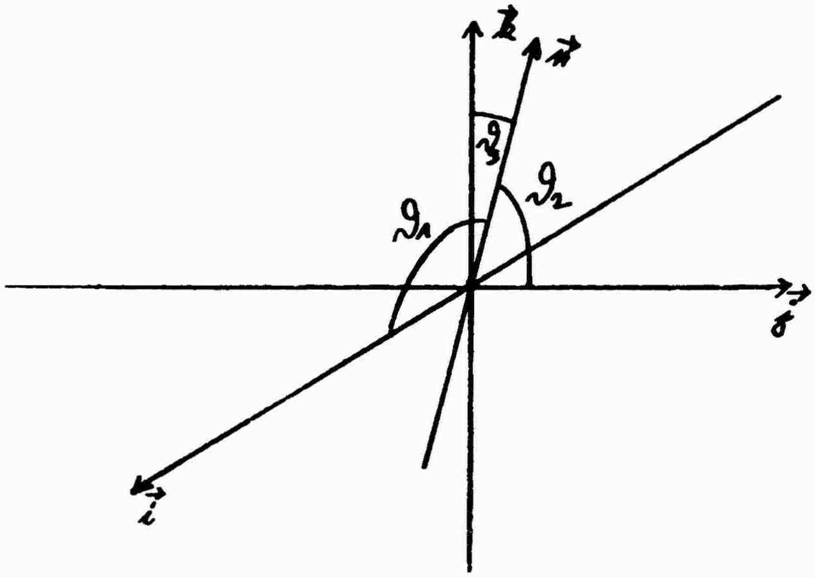

Fig. 3.2

$$\vec{i} = \begin{pmatrix} \cos\phi_1 \cdot \sin\theta_1 \\ \sin\phi_1 \cdot \sin\theta_1 \\ \cos\theta_1 \end{pmatrix}; \quad \vec{j} = \begin{pmatrix} \cos\phi_2 \cdot \sin\theta_2 \\ \sin\varphi_2 \cdot \sin\theta_2 \\ \cos\theta_2 \end{pmatrix}; \quad \vec{k} = \begin{pmatrix} \cos\phi_3 \cdot \sin\theta_3 \\ \sin\phi_3 \cdot \sin\theta_3 \\ \cos\theta_3 \end{pmatrix} \tag{3.4}$$

As $\vec{i}$, $\vec{j}$, and $\vec{k}$ form an orthogonal trihedral the following conditions are valid, too.

$$\begin{aligned} \vec{i} \times \vec{j} &= \vec{k} \\ \vec{j} \times \vec{k} &= \vec{i} \\ \vec{k} \times \vec{i} &= \vec{j} \end{aligned} \tag{3.5}$$

Together with the pedaloid condition (3.3) we get from (3.1) the voltages in terms of ϕ_i and θ_i:

$$U_i = (a^2 \cdot \cos^2\phi_i + b^2 \cdot \sin^2\phi_i)^{1/2} \cdot \sin\theta_i \tag{3.6}$$

and with the abbreviation $\omega t_o = \Omega$ we obtain

$$U_i = a\cdot b\cdot(a^2\cdot\sin^2\Omega_i + b^2\cdot\cos^2\Omega_i)^{-1/2}\cdot\sin\theta_i \quad (3.7)$$

and thereby the voltages expressed by the phase angles Ω_i. These three voltages form a vector with a constant amount, e.g.

$$\sum_{i=1}^{3} U_i^2 = a^2(\cos^2\phi_1\cdot\sin^2\theta_1 + \cos^2\phi_2\cdot\sin^2\theta_2 + \cos^2\phi_3\cdot\sin\theta_3) + b^2(\sin^2\phi_1\cdot\sin^2\theta_1 + \sin^2\phi_2\cdot\sin^2\theta_2 + \sin^2\phi_3\cdot\sin\theta_3) \quad (3.8)$$

From Eq. (3.4) we know that $\cos\phi_i\cdot\sin\theta_i$ and $\sin\phi_i\cdot\sin\theta_i$ are the direction cosines of the pedaloid axes $\vec{e}_a$ and $\vec{e}_b$ in reference to the antenna system. As the sum of the squares of direction cosines always equals 1 we may write formula (3.8) shortly as

$$\sum_{i=1}^{3} U_i^2 = a^2 + b^2 \quad (3.9)$$

On the other hand, the condition of orthogonality delivers the following formula:

$$\vec{k} = \vec{i}\times\vec{j} =$$

$$\begin{pmatrix} k_1 \\ k_2 \\ \cos\theta_3 \end{pmatrix} = \begin{pmatrix} i_2 j_3 - i_3 j_2 \\ i_3 j_1 - i_1 j_3 \\ (\cos\phi_1\cdot\sin\phi_2 - \cos\phi_2\cdot\sin\phi_1)\sin\theta_1\cdot\sin\theta_2 \end{pmatrix} \quad (3.10)$$

The main result of this formula is:

$$\begin{aligned} \cos\theta_3 &= -\sin(\phi_1 - \phi_2)\sin\theta_1\cdot\sin\theta_2 \\ \cos\theta_2 &= -\sin(\phi_2 - \phi_1)\sin\theta_1\cdot\sin\theta_3 \\ \cos\theta_1 &= -\sin(\phi_3 - \phi_3)\sin\theta_2\cdot\sin\theta_3 \end{aligned} \quad (3.11)$$

With the pedaloid condition (3.3) we derive

$$\sin(\phi_1 - \phi_2) = \sin\phi_1\cdot\cos\phi_2 - \sin\phi_2\cdot\cos\phi_1 =$$

$$= \frac{\frac{a}{b}\tan\Omega_1}{\sqrt{1+\frac{a^2}{b^2}\tan^2\Omega_1}} \cdot \frac{1}{\sqrt{1+\frac{a^2}{b^2}\tan^2\Omega_2}} -$$

$$- \frac{\frac{a}{b}\tan\Omega_2}{\sqrt{1+\frac{a^2}{b^2}\tan^2\Omega_2}} \cdot \frac{1}{\sqrt{1+\frac{a^2}{b^2}\tan^2\Omega_1}} \qquad (3.12)$$

We then obtain with Eq. (3.7)

$$\sin(\phi_1 - \phi_2) = \frac{\sin(\Omega_1 - \Omega_2)}{ab\cdot\sin\theta_1\cdot\sin\theta_2} U_1U_2 \qquad (3.13)$$

Consequently, Eq. (3.11) with the abbreviations $\Omega_1 - \Omega_2 = X_1$, $\Omega_2 - \Omega_3 = X_2$, $\Omega_3 - \Omega_1 = X_3$ (phase differences between two antennas) reads as follows:

$$\cos\theta_1 = -\frac{\sin X_2}{ab} U_2U_3$$

$$\cos\theta_2 = -\frac{\sin X_3}{ab} U_3U_1 \qquad (3.14)$$

$$\cos\theta_3 = -\frac{\sin X_1}{ab} U_1U_2$$

Since these cosines $\cos\theta_i$ are the direction cosines of the normal of the ellipse in reference to the antenna system

$$\sum_{i=1}^{3} \cos^2\theta_i = 1 \qquad (3.15)$$

is valid, or, for further calculations

$$a^2b^2 = \sin^2X_1U_1^2U_2^2 + \sin^2X_2U_2^2U_3^2 + \sin^2X_3U_3^2U_1^2 \qquad (3.16)$$

Formulas (3.9) and (3.16) together allow the evaluation of a and b.

$$P^2 = a^2 + b^2 = \sum_{i=1}^{3} U_i^2 \tag{3.17}$$

$$Q^2 = a^2 \cdot b^2 = \sum_{i=1}^{3} \sin^2 X_i U_i^2 \cdot U_{i+1}^2 \tag{3.18}$$

and therefrom

$$a^2 = \frac{P^2}{2} + \sqrt{\frac{P^4}{4} - Q^2} \tag{3.19}$$

and

$$b^2 = \frac{P^2}{2} - \sqrt{\frac{P^4}{4} - Q^2} \tag{3.20}$$

So the two main voltages are known in terms of the measured quantities!

3.5 Calculation of the Eulerian angles

The three Eulerian angles are θ, ψ, and ϕ.

θ ... angle of nutation (between ellipse normal $\vec{n}$ and the direction $\vec{k}$)

ψ ... angle of precession (between axis i and intersection line $\vec{x}$ of the $\vec{e}_a$-$\vec{e}_b$-plane and the $\vec{i}$-$\vec{j}$-plane)

ϕ ... angle of torsion (between the intersection line $\vec{x}$ and the axis $\vec{e}_a$)

θ: It is evident (Fig. 3.2) that

$$\theta \equiv \theta_3 \tag{3.21}$$

ψ: First we have to determine the intersection line $\vec{x}$. So we form the cross product of the vectors $\vec{k}$ and $\vec{n}$.

$$\vec{k} \times \vec{u} = \begin{pmatrix} \sin\phi_3 \\ -\cos\phi_3 \\ 0 \end{pmatrix} = \vec{x} \tag{3.22}$$

Now the requested angles are easily to be calculated:

$$(\vec{X}\cdot\vec{i}) = \cos\psi = \cos\phi_1\cdot\sin\theta_1\cdot\sin\phi_3 - \sin\phi_1\cdot\sin\theta_1\cdot\cos\phi_3 \qquad (3.23)$$

As there are certain conditions valid between the direction cosines in the matrix of torsion we can write Eq. (3.23) as follows:

$$(\vec{X}\cdot\vec{i}) = \cos\psi = -\frac{\cos\theta_2}{\sin\theta_3} \qquad (3.24)$$

Together with (3.15)

$$\sin\psi = \frac{\cos\theta_1}{\sin\theta_3} \qquad (3.25)$$

follows.

$\underline{\phi:}$ The angle ϕ follows from the scalar product of the vectors $\vec{x}$ and $\vec{e_a}$.

$$\vec{x}\cdot\vec{e_a} = \cos\phi = \sin\phi_3 \qquad (3.26)$$

$\sin\phi$ follows from the cross product of these two vectors:

$$\left|\left|\vec{x}\times e_a\right|\right| = \sin\phi = \cos\phi_3 \qquad (3.27)$$

We now have to write the Eulerian angles in terms of the voltages U_1, U_2, U_3 and the phase angles X_1, X_2, X_3.

$\underline{\theta:}$

$$\cos\theta \equiv \cos\theta_3 = -\frac{\sin X_1}{ab}\cdot U_1U_2 \qquad (3.28)$$

As ab is evaluated in Eq. (3.16), $\cos\theta$ is known.

$\underline{\psi:}$

$$\cos\psi = -\frac{\cos\theta_2}{\sin\theta_3} \qquad (3.29)$$

$$\cos\theta_2 = -\frac{\sin{}_3}{ab}\,U_3U_1 \qquad (3.30)$$

$$\sin\theta_3 = \sqrt{1-\cos^2\theta_3} = \frac{1}{ab}\cdot\sqrt{\sin^2X_2U_2^2U_3^2+\sin^2X_3U_3^2U_1^2} \qquad (3.31)$$

$$\cos\psi = \frac{1}{\sqrt{\dfrac{\sin^2X_2U_2^2}{\sin^2X_3U_1^2}+1}} \qquad (3.32)$$

$$\sin\psi = \frac{\cos\theta_1}{\sin\theta_3} \qquad (3.33)$$

$$\cos\theta_1 = -\frac{\sin X_1U_1U_2}{ab} \qquad (3.34)$$

$$\sin\psi = \frac{-1}{\sqrt{1+\dfrac{\sin^2X_3U_1{}^2}{\sin^2X_2U_2{}^2}}} \qquad (3.35)$$

So the angle ψ is known, too.

ϕ: From Eq. (3.6) we get:

$$\cos\phi = \sin\phi_3 \qquad (3.36)$$

$$U_3{}^2 = (a^2\cos^2\phi_3 + b^2\sin^2\phi_3)\sin^2\theta_3 \qquad (3.37)$$

$$\sin^2\phi_3 = \frac{\dfrac{U_3{}^2}{\sin^2\theta_3} - a^2}{b^2 - a^2} \qquad (3.38)$$

$$\sin\phi = \cos\phi_3 \qquad (3.39)$$

$$\cos\phi_3 = \frac{\dfrac{U_3{}^2}{\sin^2\theta_3} - b^2}{a^2 - b^2} \qquad (3.40)$$

As a, b, and $\sin\theta_s$ are known from Eqs. (3.19), (3.20), (3.14), all Eulerian angles are known in terms of the measured quantities.

3.6 Conclusion

It is possible to determine the exact spatial position of the rotary field ellipse by measuring three voltages and three phase angles. The results can be computed. This new method has the advantage of being quick and free of errors of adjustment (measurement possible at any trihedral position!) and can be done automatically without any further adjustment of the antenna position.

CHAPTER 4

EXTERNALLY KEYED PHASE-LOCK DEVICE

4.1 Equipment

The externally keyed (by VLF-wave propagation) phase-lock device described in /11/ measures the phase difference between a VLF wave with the frequency of 2.667 kHz in the near field and the GBR signal (16.0 kHz) in the far field. The measuring principle shall be briefly repeated (cf. Fig. 4.1, 4.2, 4.3).

The GBR signal (A2 or F2 keyed) is received by ferrite rod antennas and used for phase-stable triggering of an extremely stable balance oscillator. The lock-in range is only 20 Hz so that only the 16,000 Hz-signal is used for phase triggering during the FM-keyed time (16,000 and 15,950 Hz), thus avoiding influences of keying effects and giving a stable, extremely exact time normal at any arbitrary point of reception.

This type of time normal is used to trigger both the transmitter and the receiver of a VLF-signal transmission chain. Before triggering the frequency must be changed in order not to affect the original "clock-triggering" signal. To get the required high accuracy only a digital frequency change is allowed. In the described equipment a divide-by-6-mode is used so that the frequency of 2.667 Hz results.

In the transmitting equipment this signal is amplified and sent by a frame antenna.

The receiving equipment uses two ferrite rod antennas for the reception of the VLF signal and of the GBR synchronous signal, respectively. The two signals (VLF signal and the divided 16 kHz signal) are compared in the phase detector. The result is a DC-signal changing with phase difference which may act as phase proportional voltage on the one hand or as rectified signal of a receiver with extremely small bandwidth (depending on integration time constant; here 0.2 Hz!) on the other hand.

The measuring practice showed the necessity of some changes and supplements in circuit design, e.g.:
1) a special Schmitt-trigger to make the triggering correspond with the zero-axis crossing of the GBR signal, thus ensuring that the phase relation is independent on the amplitude (further details see Fig. 4.1 or /11/);
2) a measuring amplifier for measuring the incoming VLF signal combined with an attenuator providing a unique signal amplitude at the phase detector independent on the input voltage (cf. Fig. 4.2 and 4,3);
3) a main operation mode switch with the positions "off / battery control / GBR amplitude / VLF amplitude / phase".
A number of test jacks were added at the front panels of both the transmitting and receiving parts for operation control and the possibility of connecting external devices (e.g. line recorder).

The complete electrical and mechanical design is shown in Figs. C, D, E, F.

4.2 Measurements

The measurements were scheduled for the first quarter of 1977 but could not be done in time because GBR stopped transmitting in January for a longer period of time.

After GBR had started again, the phase measurements were conducted in St. Gertraudi mine / Tyrol. The measuring series proved to be correct because it was repeated twice.

The [illegible] amplifier (1 kW maximum output) was used as transmitter in connection with the big loop (40x40 m, 10 windings) which was tuned to resonance by capacitors. Although there is a stopper circuit for the VLF frequency the current in the antenna (15 A) produces such a high magnetic field in the very near measuring points, that the ferrite rod antenna for the reception of the synchronizing GBR signal had to be oriented very exactly in minimum field strength direction of the VLF signal in order to prevent an overload of the input.

The measuring points were situated along the "Westschlag"-gallery which is nearly parallel to the Inn valley. Table 4.1 gives the measuring results.

48-9

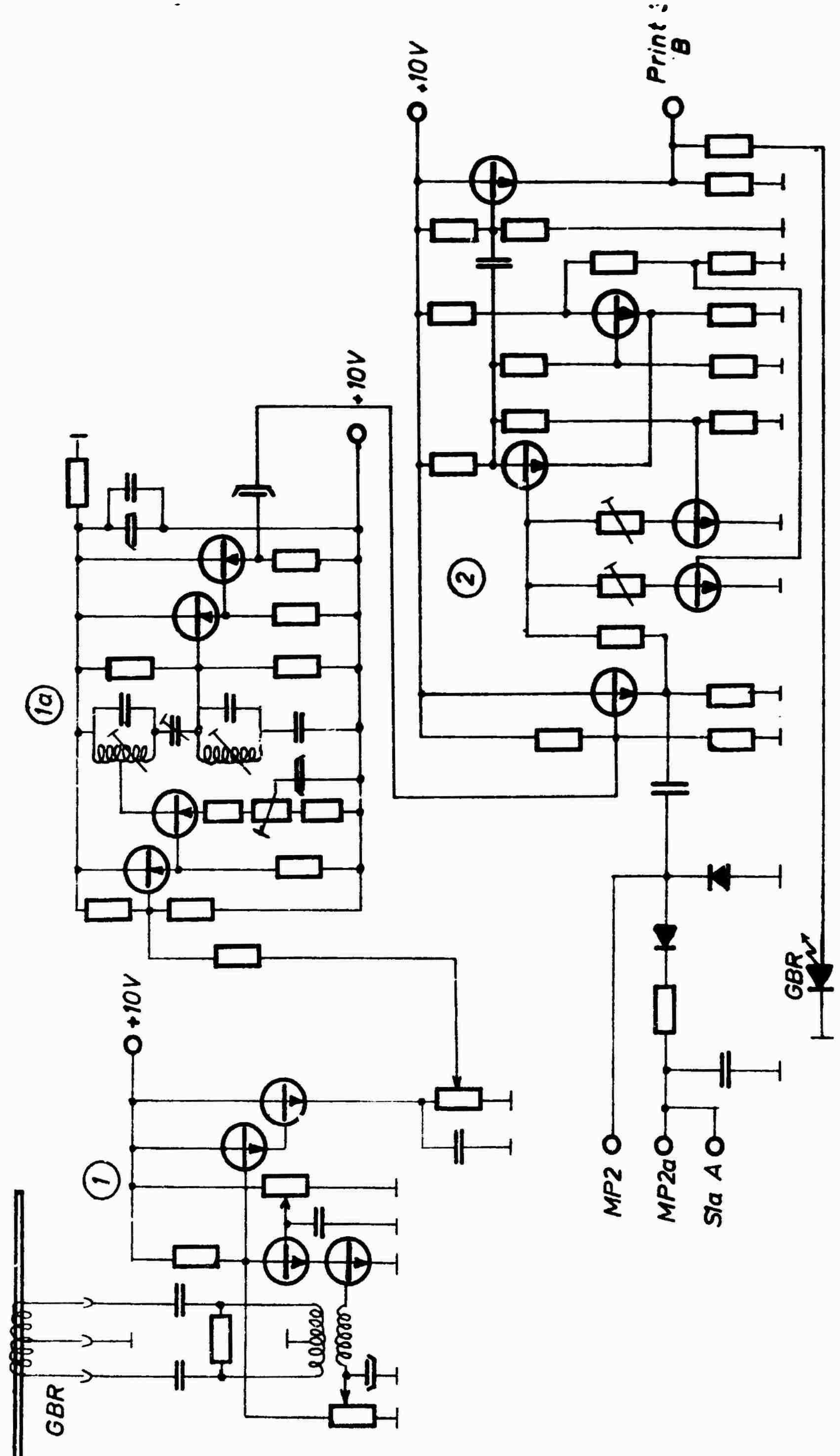

Fig.: 4.1

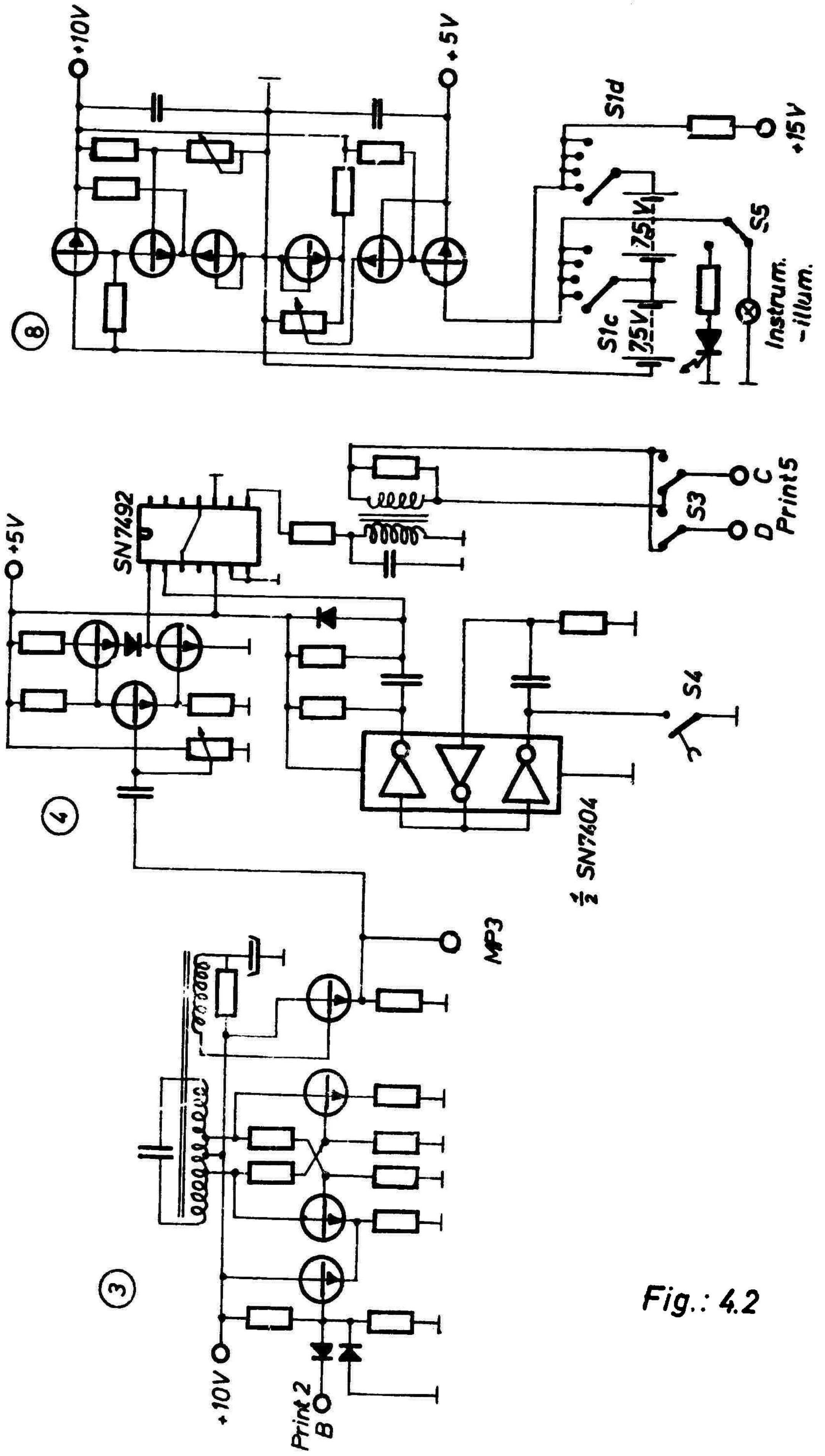

⑧
+10V
+5V
S1d
+15V
S5
S1c
7.5V
7.5V
7.5V
7.5V
Instrum. -illum.
④
+5V
SN7492
C
D
Print 5
S3
S4
½ SN7404
MP3
③
+10V
Print 2
B

Fig.: 4.2

48 c

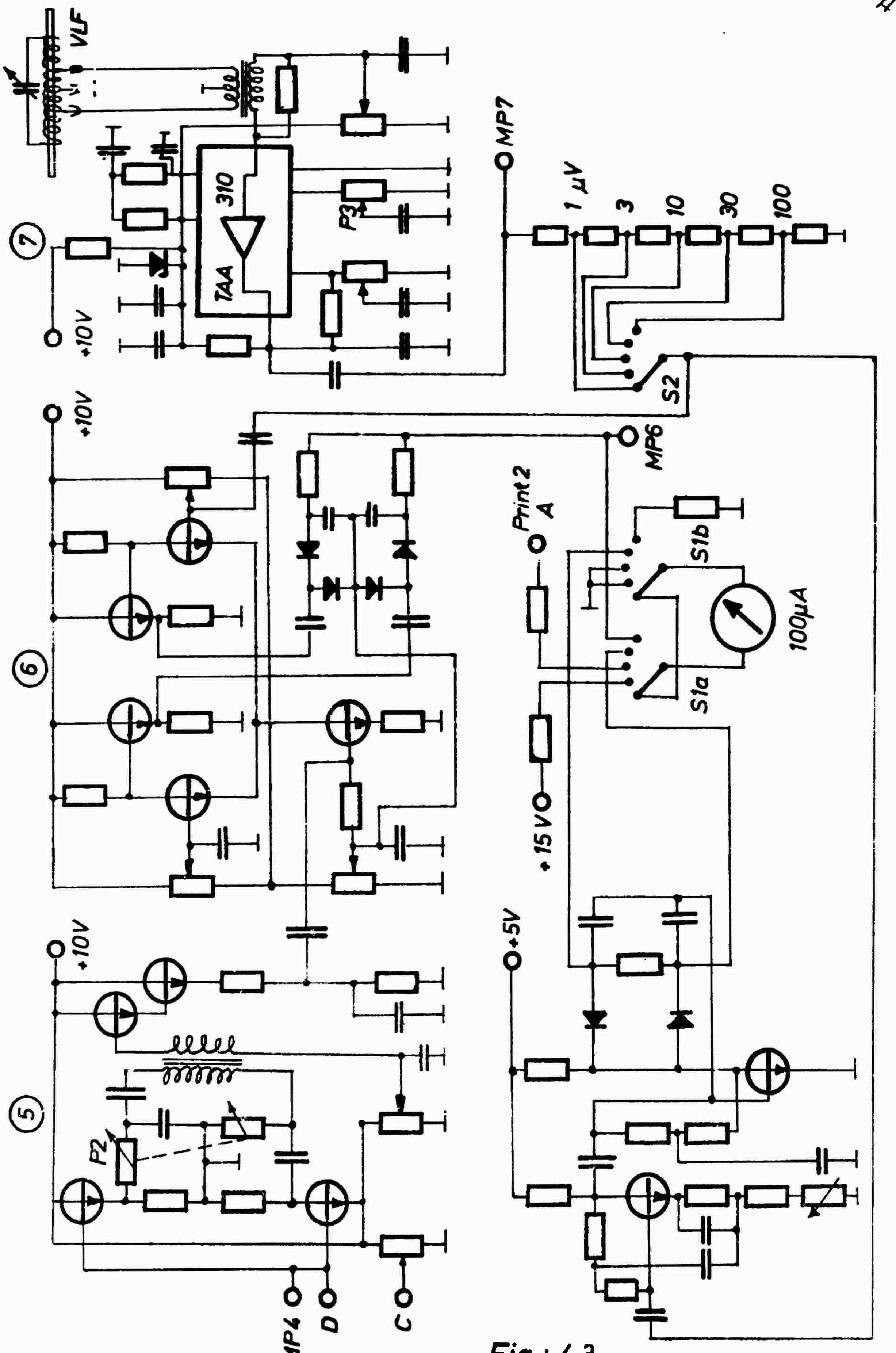

⑦
+10V
VLF
TAA 310
P3
MP7
1 µV
3
10
30
100
S2
⑥
+10V
MP6
Print 2
A
S1b
S1a
100µA
+15V
+5V
⑤
+10V
P2
MP4
D
C

Fig.: 4.3

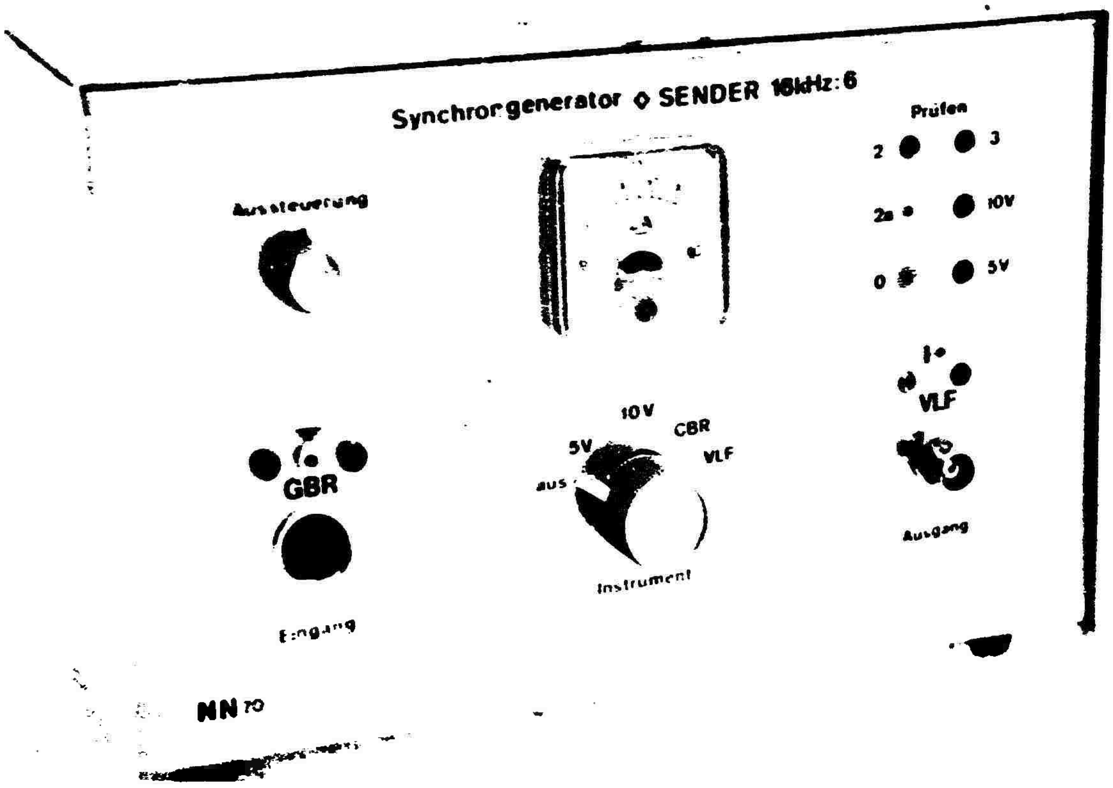
Synchrorgenerator ◇ SENDER 16kHz:6
Prüfen
2
3
2a
10V
0
5V
Aussteuerung
GBR
Eingang
10 V
CBR
5V
VLF
aus
Instrument
VLF
Ausgang
NN 70

Bild C

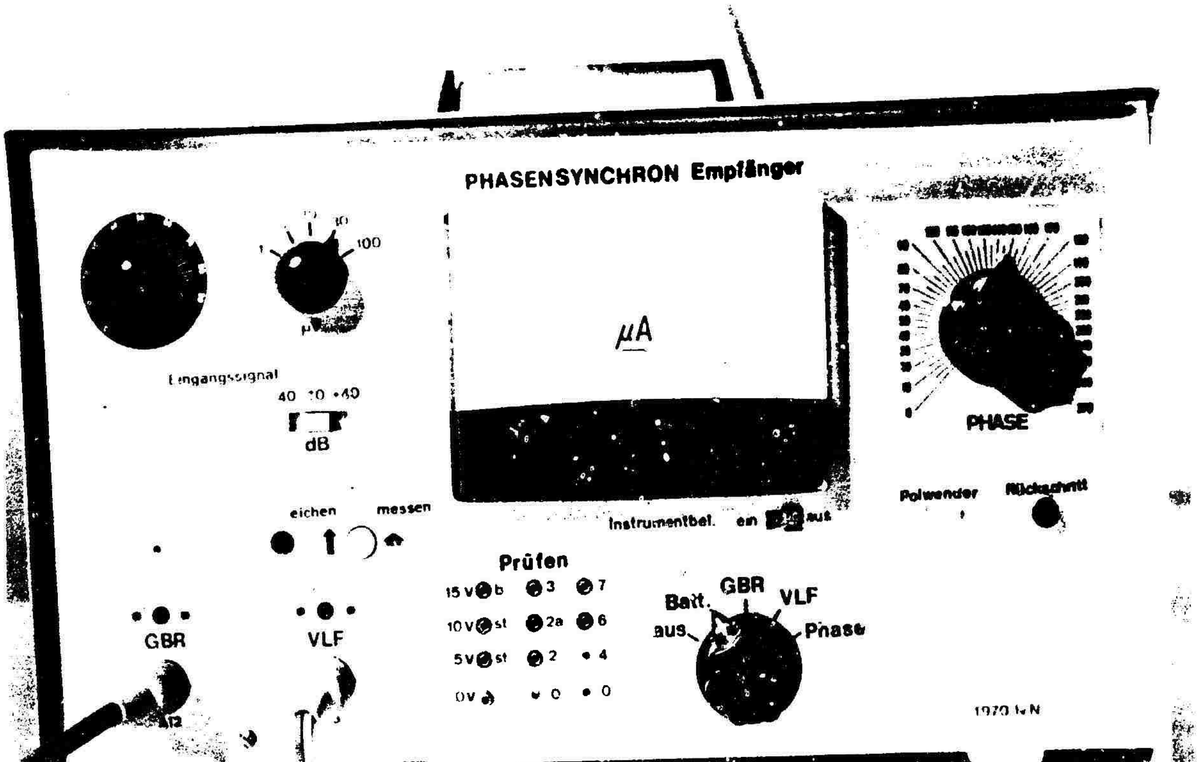
PHASENSYNCHRON Empfänger
1
10
30
100
µA
Eingangssignal
40 10 +40
dB
eichen
messen
Instrumentbel. ein aus
PHASE
Polwender
Rückschnitt
Prüfen
15 V b 3 7
10 V st 2a 6
5 V st 2 4
0 V 0 0
Batt.
GBR
VLF
aus
Phase
GBR
VLF
1970 IvN

Bild D

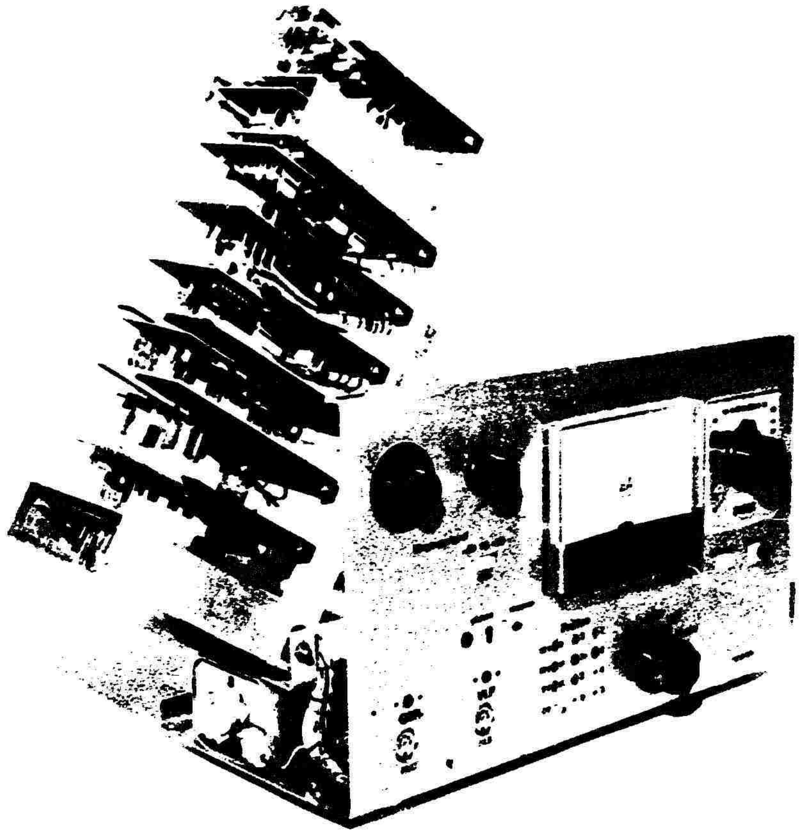

Bild E

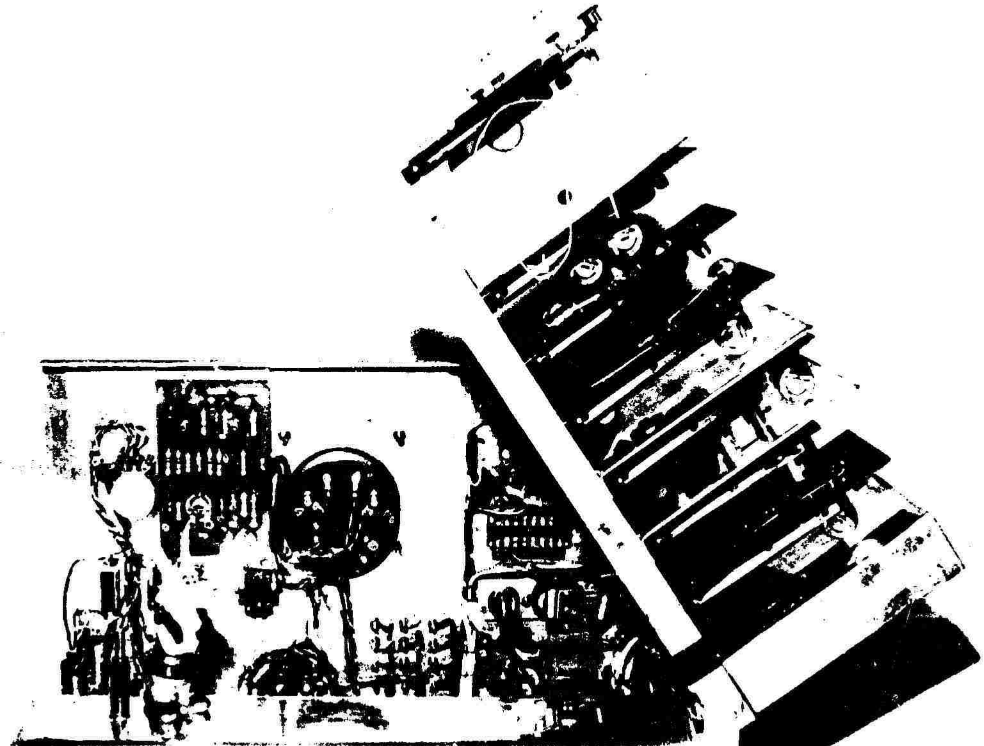

Table 4.1

d |m|	U_{VLF} |μV|	Phase |°|
100	27	20
150	21	15
200	14	15
250	7.4	15
300	5.0	20
350	2.5	20
400	1.9	20
450	1.5	25
500	1.1	30
550	0.9	20
600	0.77	18
650	0.63	22
700	0.54	15
750	0.47	0

d ..... distance between transmitter and receiver
U_{VLF} .. voltage proportional to received VLF signal
Phase . phase difference between synchronization signal GBR and transmitted VLF signal reduced modulo 60° (because of the 6 : 1 reduction of the GBR frequency)

Result: Primarily it was assumed that the GBR incoming direction is vertical to the line transmitter - receiver so that there is no phase difference between these two points. Therefore the difference was expected to rise with increasing distance.

4.3 Conclusion

This phase measuring device measures the phase difference between the synchronization signal and the VLF signal, and has the disadvantage that for measuring the phase of one channel the phase shift of the other channel must be known. If transmitter and receiver are exchanged the phase shifts between VLF and GBR signal can be added and subtracted, respectively. Thus, it is possible to eliminate the phase shift of the GBR signal.

CHAPTER 5

A DIGITAL PHASE MEASURING DEVICE

5.1 Introduction

To be able to measure phases at the propagation of electromagnetic waves in the VLF range a device was developed by Dr. N. NESSLER /20/ showing the possibility of phase measurements within this frequency range for the first time. For the synchronization between transmitter and receiver a further external transmitter was used. This existing equipment allows phase measurements only at a certain frequency, and in some special cases indication is amplitude-dependent. A new phase measuring device comparing two incoming signals (measuring signal and reference signal) completely independent on frequency and amplitude is now being built.

The requirements which should be fulfilled by this device are rather high: current consumption must be very small to enable battery operation; the device should have little weight and volume and be insensitive to heavy pushes and high atmospheric humidity to be able to be operated in the mine; production cost must be kept low (since the main part of the device is intended to be used as well for a special measuring equipment of the rotary field ellipse).

Thorough information showed that no commercial device fulfills all these requirements, that is why it was considered most efficient to build it in our own laboratory.

The device is to indicate the phase digitally independently on amplitude and frequency within the frequency range of 100 Hz - 100 kHz over a liquid crystal display counting from -180° to +180°.

5.2 Basic construction

Fig. 5.1 shows the block diagram of the device without a representation of receiving antennas and preamplifiers. The two receiving signals the mutual phase position of which is to be measured are connected to the inputs A and B. The two Schmitt trigger units transform the sine signal at the input to a square-wave signal with the pulse duty factor 1 : 2 (pulse duration : pulse period). The two square-wave signals are compared as to their coincidence in the discriminator. The pulse duration of the output signal at the discriminator is a direct measure for the phase shift. In the logic unity this phase-proportional signal cuts in a counting oscillator (10 MHz) the number of pulses of which is counted. This number within a definite time is a direct measure for the phase angle independent on input amplitude and input frequency and is indicated at the liquid crystal display.

5.3 Description of circuit

5.3.1 Input Schmitt trigger with null hysteresis

Fig. 5.2 shows the circuit for channel A. The sine signal is connected to input A (about 30 mV_{pp} - 5 V_{pp}). In the upper branch an impedance transformer follows (T 1) and connected thereto the one "half-Schmitt trigger". In the bottom branch the sine signal is inverted by a T 2 and the gain of the transistor is set to 1 by a P 3. The succeeding T 3 works as an emitter follower and controls the second half-Schmitt trigger. Such a half-Schmitt

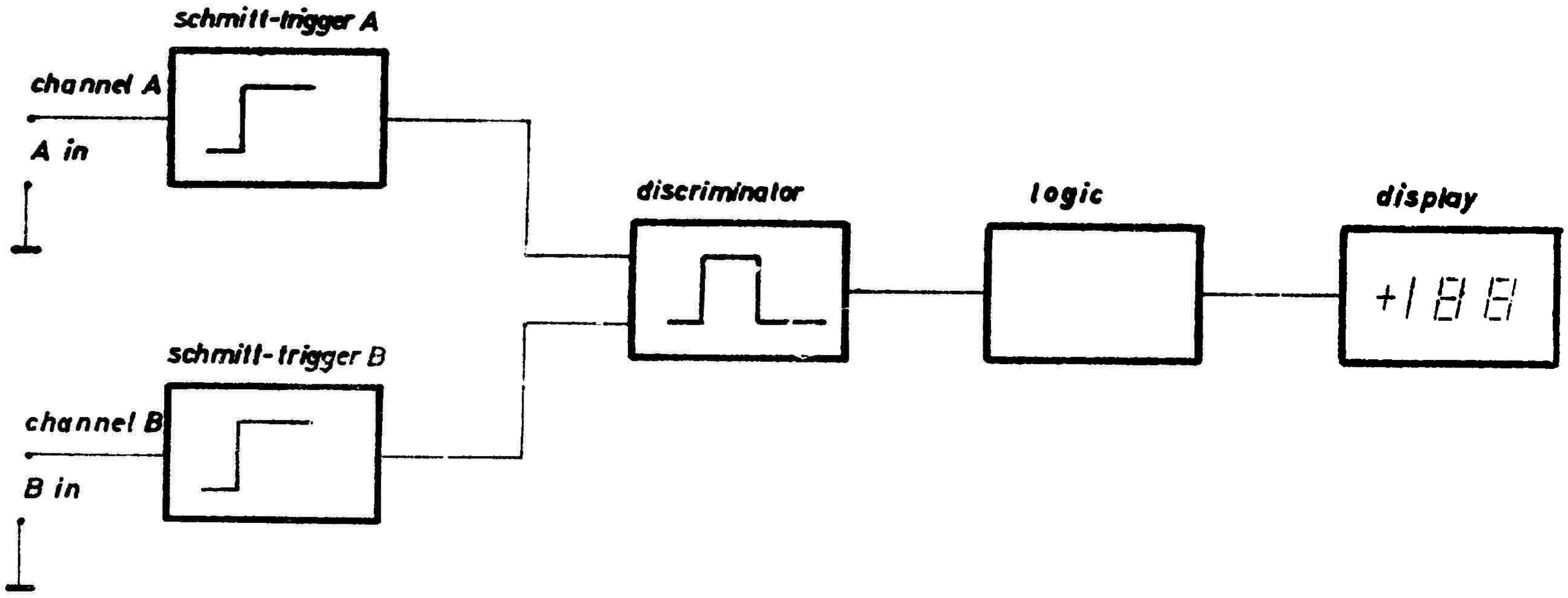
schmitt-trigger A
channel A
A in
schmitt-trigger B
channel B
B in
discriminator
logic
display
+188

FIG. 5.1.

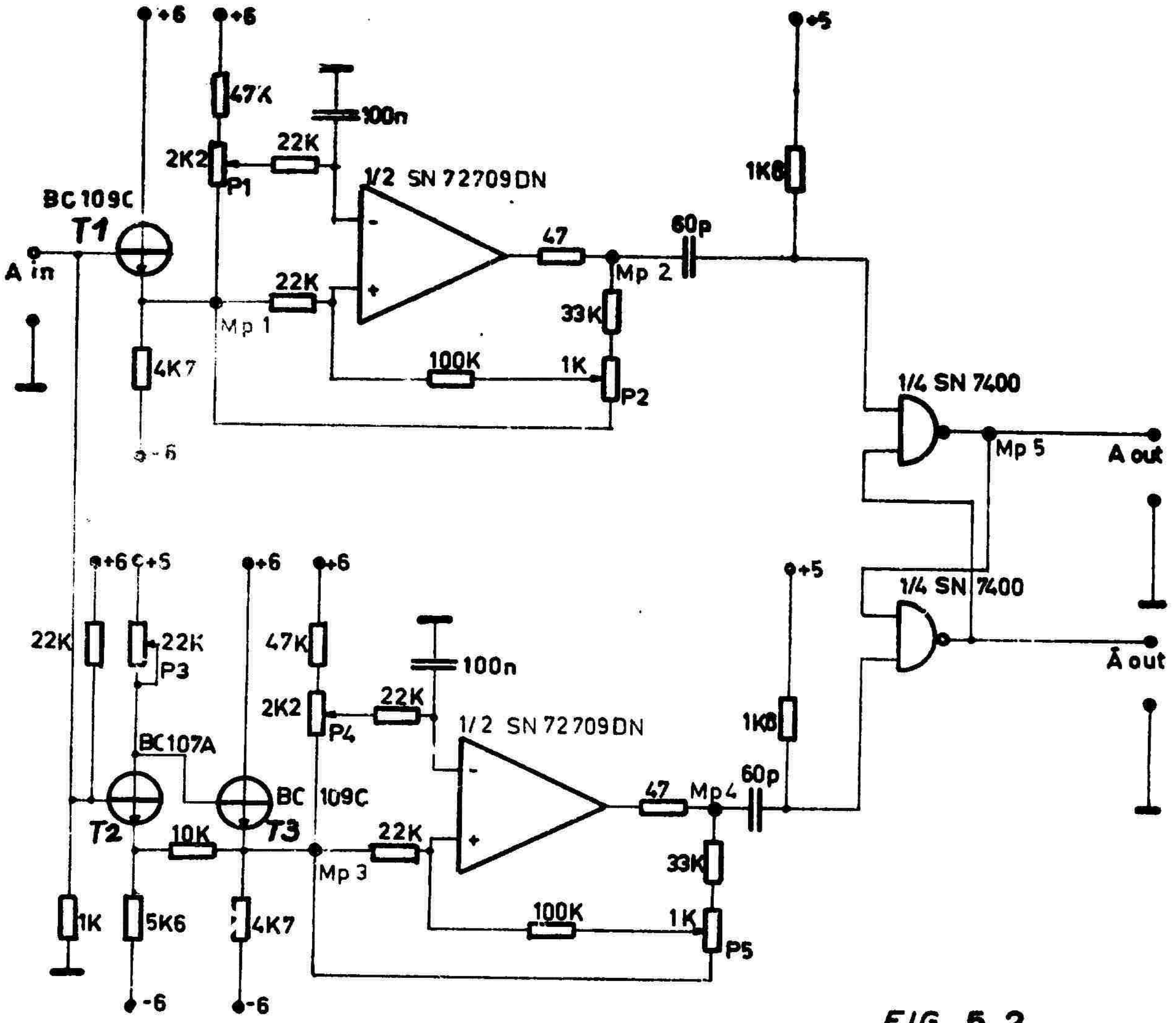
+6
+6
47K
100n
2K2
22K
P1
1/2 SN 72709DN
BC109C
T1
A in
22K
Mp 1
47
Mp 2
60p
33K
4K7
100K
1K
P2
-6
+5
1K8
1/4 SN 7400
Mp 5
A out
+6
+5
22K
22K
P3
BC107A
T2
10K
1K
5K6
-6
+6
BC 109C
T3
4K7
-6
+6
47K
2K2
P4
22K
100n
1/2 SN 72709DN
22K
Mp 3
47
Mp4
60p
33K
100K
1K
P5
+5
1K8
1/4 SN 7400
Ā out

FIG. 5.2.

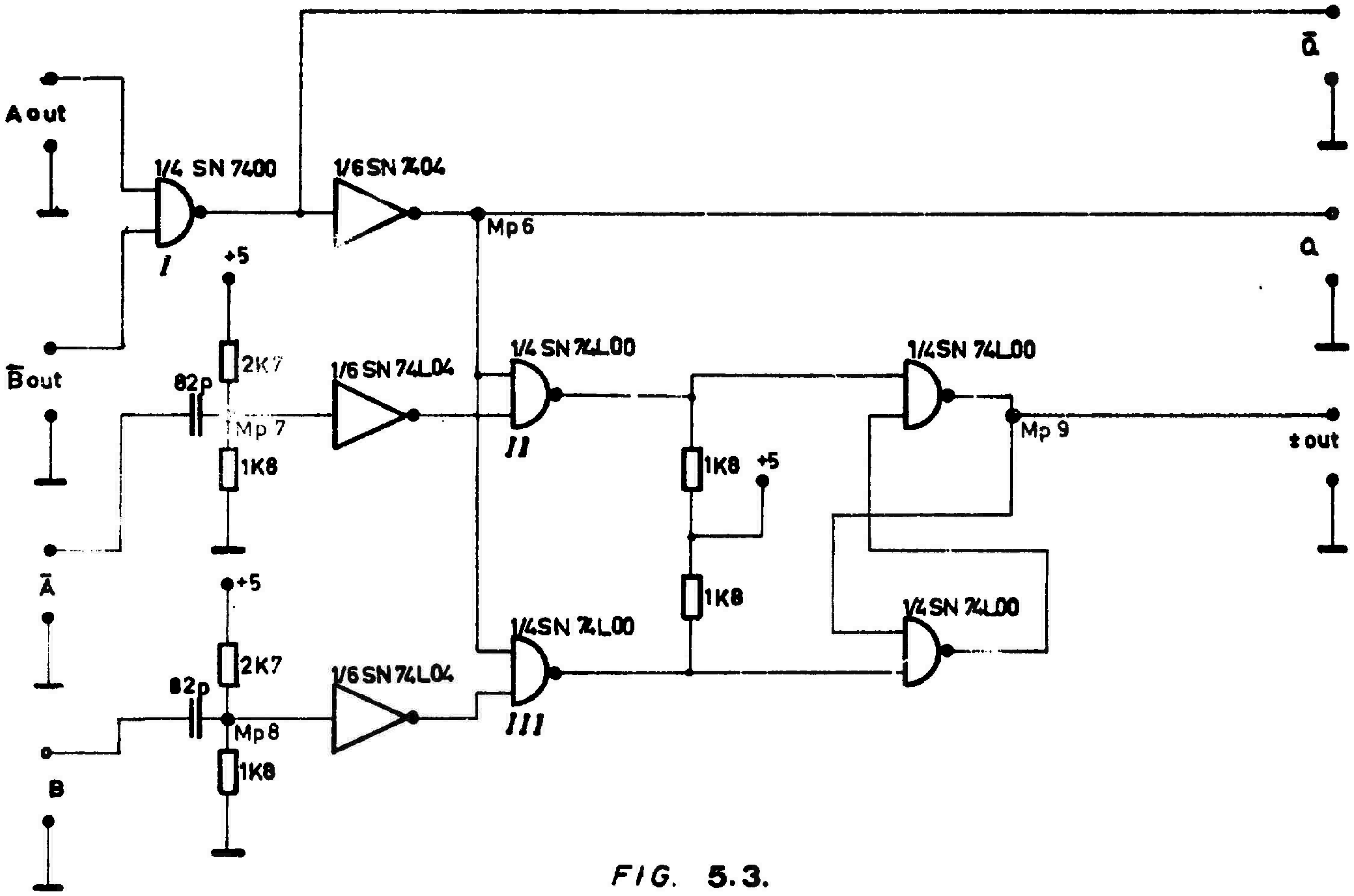
Aout
B̄out
Ā
B
1/4 SN 7400
I
1/6 SN 7404
Mp 6
+5
2K7
82p
Mp 7
1K8
1/6 SN 74L04
+5
2K7
82p
Mp 8
1K8
1/6 SN 74L04
1/4 SN 74L00
II
1/4 SN 74L00
III
1K8
+5
1K8
1/4 SN 74L00
1/4 SN 74L00
Mp 9
ā
a
t out

FIG. 5.3.

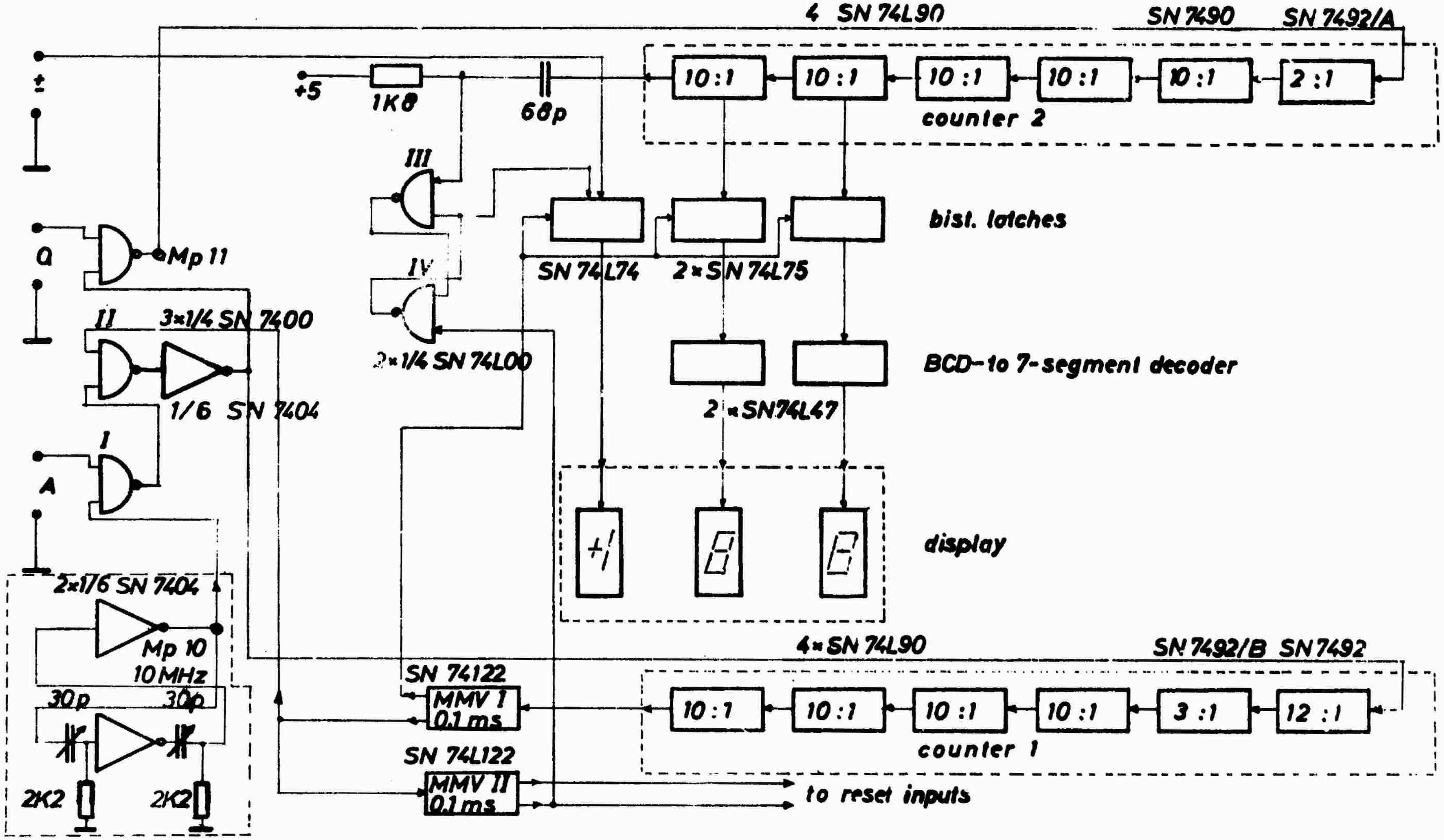
4 SN 74L90
SN 7490
SN 7492/A
±
+5
1K8
68p
10 : 1
10 : 1
10 : 1
10 : 1
10 : 1
2 : 1
counter 2
III
bist. latches
Q
Mp 11
SN 74L74
2 × SN 74L75
IV
II
3×1/4 SN 7400
2×1/4 SN 74L00
BCD-to 7-segment decoder
1/6 SN 7404
2 × SN74L47
I
A
display
2×1/6 SN 7404
Mp 10
10 MHz
30p
30p
2K2
2K2
4 × SN 74L90
SN 7492/B
SN 7492
SN 74122
MMV I
0.1 ms
10 : 1
10 : 1
10 : 1
10 : 1
3 : 1
12 : 1
counter 1
SN 74L122
MMV II
0.1 ms
to reset inputs

FIG. 5.4.

through. This interruption is necessary when the input-signal becomes discontinuous as it is the case with keyed transmitters. Counter 2 can reach 360000 at most since the two counters only work when A = L (pulse duty factor of A is 1 : 2).

After dividing this number by two and cancellation of the last three decimal places the content of the counter corresponds to the phase shift measured in angular degrees. The end of one counting cycle sets the monostable multivibrator I to a logical 'L' which blocks the 10 MHz clock pulse over NAND gate II. At the same time the bistable latches are switched through. The first two decimal places of counter 2 and the carry over of counter 2 are directly transferred to the indicator. The falling slope of MMV I switches a second monostable multivibrator (MMV II) to the quasistable position. Consequently all counters and the flip-flop for the carry-over (NAND gates III and IV) are zeroed; a new counting cycle can start.

The above described arrangement allows a phase indication independent of the input frequency and independent of the 10 MHz clock frequency.

5.3.4 The display unit

A 2 1/2-place liquid crystal display (L.C.D.) is used which has the advantage of an extremely low power consumption (about 40μW/segment, i.e. less than 1/1000 of the power requirement of a segment of an L.E.D. The drive of the L.C.D. is more laborious than triggering the L.E.D., since the L.C.D. can only be operated by alternating current from about 15 V_{eff} at 20 - 100 Hz. A special circuit was now developed producing an a-c voltage of 60 V_{pp} which is shown in Fig. 5.5.

The a-c voltage is produced by a self-starting multivibrator /22/ oscillating at a frequency of about 80 Hz. The three coil windings were bridged by capacitors (C2, C3, C4) to avoid dangerous voltage peaks at the output. The output voltage becomes sinusoidal and nearly independent on the load. This output voltage is now rectified over C5 and D1. With this circuit (Villard-doubling) the a-c-component is maintained but is increased by 1/2 V_{pp} (pulsating d-c voltage between 0 V and 60 V). The transistors are special high-blocking types with $U_{CEO} \geq 60$ V. Only the a-c-component is coupled out over C6-C21 and laid onto the segment of the L.C.D.

By using this circuit we can operate the display with the required a-c voltage of about 20 V_{eff} and 80 Hz, which grants a high lifetime of the segments. At the development of this circuit it was taken into account to keep power consumption low. The current input for the whole display unit is not more than 3 mA at 5 V.

5.3.5 Power supply

The device is operated by 2 batteries. For the linear circuits a 12 V accumulator is used. The voltage of ± 6 V for the operational amplifier is obtained by voltage division. The logic is operated by a separate battery (Fig. 5.6). An estimation of the power consumption when using normal ICs showed, that the logic would take about 3300 mW. Consequently, it is advisable to use low-power ICs wherever possible to reduce power consumption to about one half. In spite of the high prime costs the use of low-power ICs is justified, since it will then be possible to take smaller and cheaper batteries and to reduce weight and volume of the device. Since the switching time of the 'L'-series is longer than that of the normal series, low-power ICs can only be used where the limiting frequency is below 1 MHz.

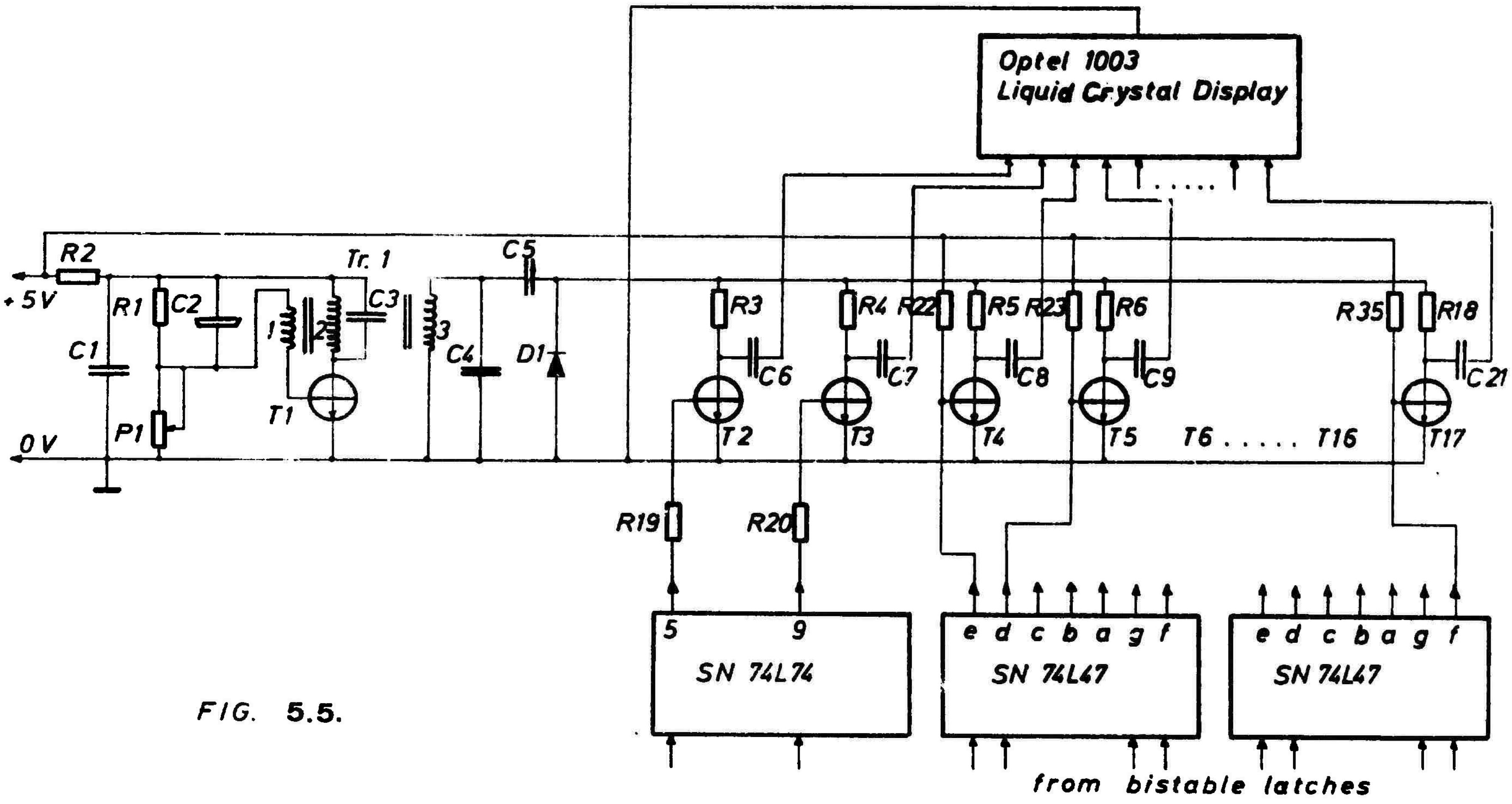
Optel 1003
Liquid Crystal Display
R2
+5V
0V
R1
C1
C2
P1
Tr. 1
1
2
3
C3
T1
C4
C5
D1
R3
C6
T2
R4
R22
C7
T3
R5
R23
C8
T4
R6
C9
T5
T6 ..... T16
R35
R18
C21
T17
R19
R20
5
9
SN 74L74
e d c b a g f
SN 74L47
e d c b a g f
SN 74L47
from bistable latches

FIG. 5.5.

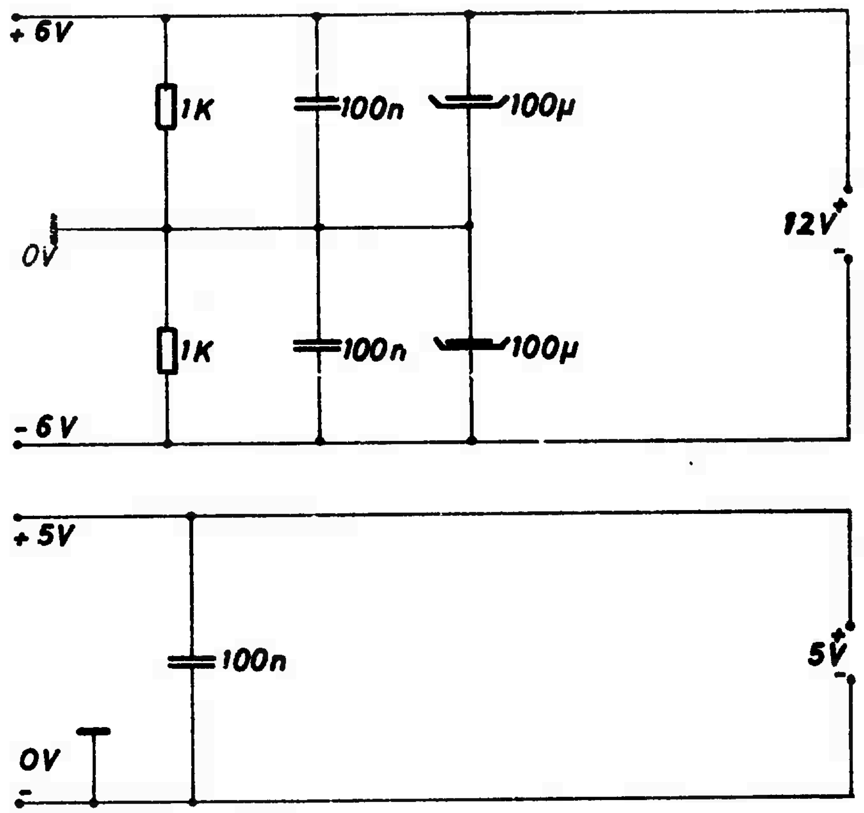

FIG. 5.6.

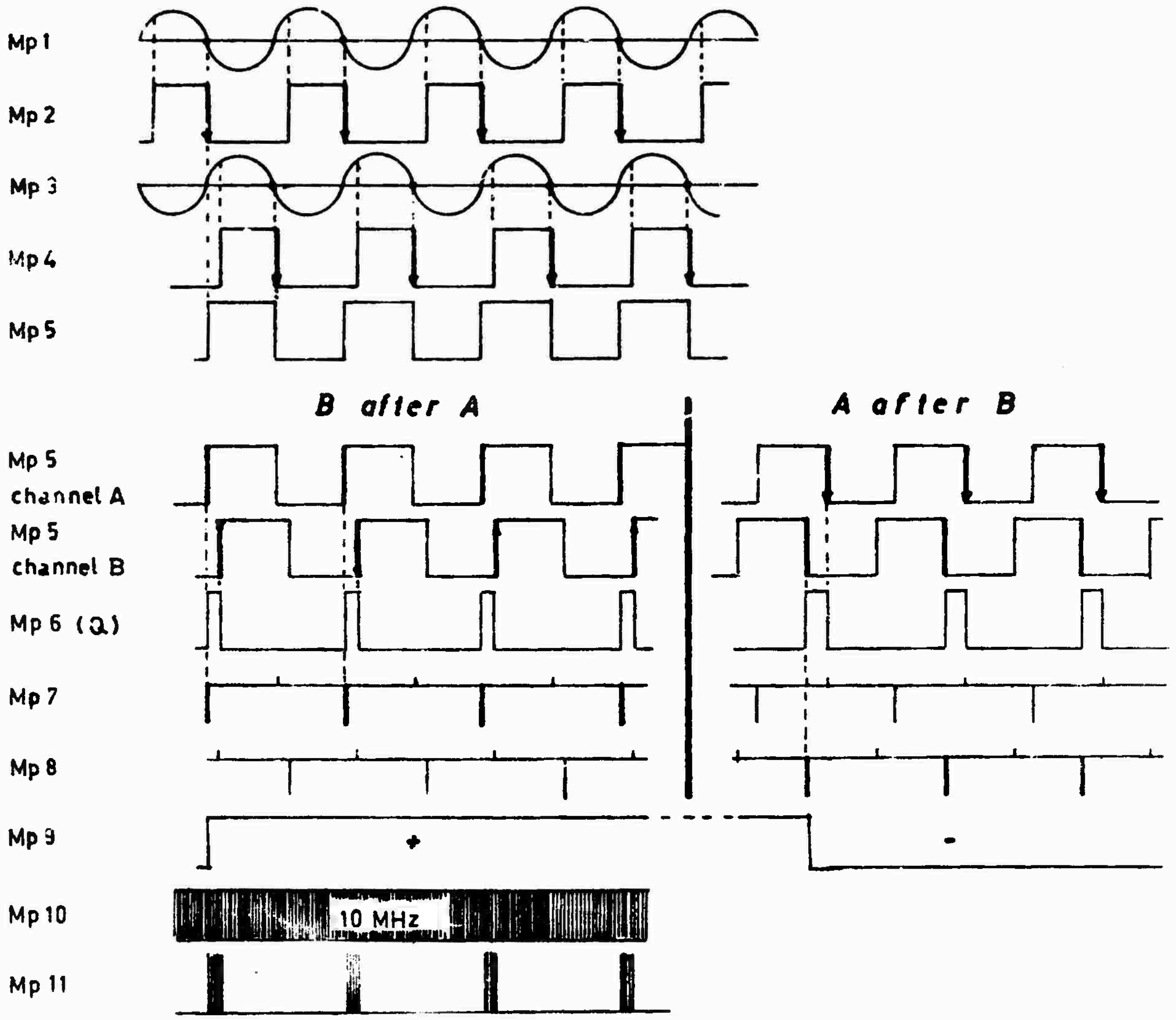
Mp 1
Mp 2
Mp 3
Mp 4
Mp 5
B after A
A after B
Mp 5
channel A
Mp 5
channel B
Mp 6 (Q)
Mp 7
Mp 8
Mp 9
+
-
Mp 10
10 MHz
Mp 11

FIG. 5.7.

5.4 Error estimation

The kind of logic causes 2 errors to arise at counting the Q signal.

Error 1

At counting the Q signal by means of the 10 MHz signal the number of clock pulses has an inaccuracy of ±1 pulse per impulse train (Fig. 5.8). During one counting cycle

$$n_1 = t \cdot \nu_1$$

t ... duration of a counting cycle (sec)
ν_1 .. measuring frequency (Hz)

of such impulse trains occur. The content of counter 2 has a variation of $\pm n_1$ in the most unfavorable case.

Translated to angular degrees the indication error amounts to

$$\Delta\phi_1 = \pm t \cdot \nu_1 \cdot 360/a$$

$\Delta\phi_1$ .. error 1 ($^\circ$)
a .... maximum content of counter 1 (in this case fixed to 360000)

With

$$t = a/\nu_2$$

ν_2 ... clock frequency (Hz)

we have a final result for error 1

$$\Delta\phi_1 = \pm\nu_1/\nu_2 \cdot 360 \qquad (5.1)$$

This shows that the error depends only on the ratio of input frequency to clock frequency. An improvement can be reached by increasing the clock frequency. In the present device $\nu_2 = 10^7 = 10$ MHz.

As is shown in Table 5.2, error 1 is relatively large. A control at the ready-built device, however, showed the real error to be smaller than in Table 5.2 by one order of magnitude, which is due to the fact that the excess and the lack of counted pulses neutralize each other. An exact calculation by means of calculus of probability confirms this measurement result.

<u>Error 2</u>

Fig. 9 shows the formation of error 2; we can distinguish three cases:

Case a) is the ideal case. In the impulse interval of the impulse train the MMV rebounces to the stable state thereby starting the counting cycle as soon as A = L. Let the ratio of clock frequency to measuring frequency be a whole-number multiple modulo 360,000 of frequency A, so that after a definite number of complete impulses A 360,000 clock impulses were counted in counter 1. This means that every complete impulse train of the duration t1 corresponds to a complete impulse train τ. Since the ratio t1 : τ which is proportional to the phase is maintained, no error of the second type arises in this case.

Case b) Let the frequency of A be somewhat smaller than for case a, so that the 360,000 impulses of counter 1 do not completely fill up the impulse groups A. Let the counting cycle - turned on by the MMV - start just at that moment when the impulse group τ in counter 2 corresponding exactly to a block t1 is over.

Case c) Let the frequency of A be slightly larger than in case a, so that the 360,000 impulses of counter 1 need a bit more time than is corresponding to an integral number of impulses A. we may have the case that at

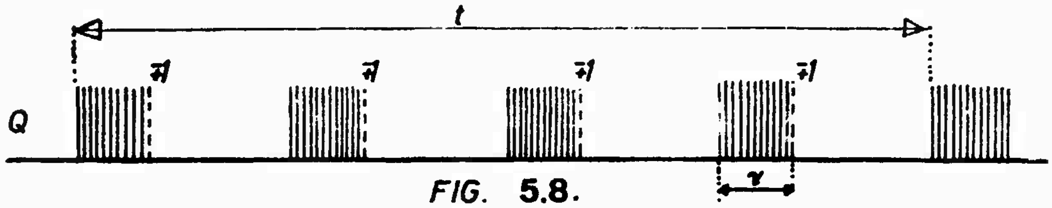
t
Q
τ

FIG. **5.8.**

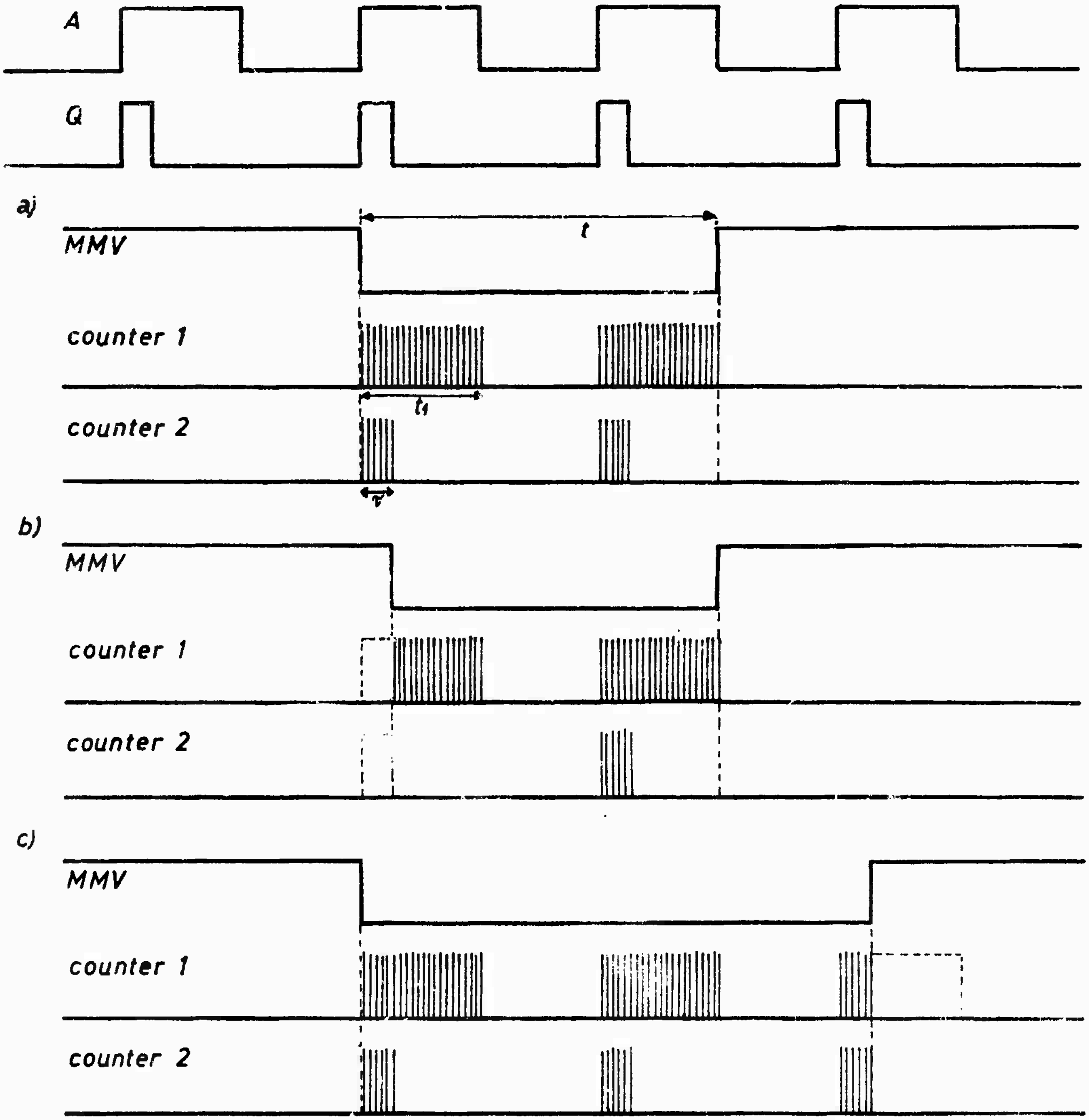
A
Q
a)
MMV
t
counter 1
t1
counter 2
τ
b)
MMV
counter 1
counter 2
c)
MMV
counter 1
counter 2

FIG. **5.9.**

starting the counting according to case a) we count just one additional impulse train τ in counter 2, whereas the corresponding impulse group t1 in counter 1 is not counted completely.

Calculation

To be able to conduct calculations the impulses coming under the period τ must be distributed equally to the time t1. Therefrom we can calculate the lack (case b) or the excess (casec) of impulses in counter 2.

Case b: At first we calculate the number of impulses n that were missing in counter 2 in relation to counter 1

$$n = \frac{\tau}{t1} (t_1 - \tau)\nu_2$$

From the definition of the impulse width τ

$$\tau : 2t_1 = \phi : 360$$

we get with

$$\Delta\phi_2 = n \cdot \frac{360}{a}$$

the equation for error 2

$$\Delta\phi_2 = \left(\phi - \frac{\phi^2}{360}\right) \frac{\nu_2}{\nu_1} \cdot \frac{2}{a}$$

$\Delta\phi_2$ ... error 2

ϕ ..... phase position

ν_1 .... measuring frequency

ν_2 .... clock frequency

a ..... maximum content of counter 1

For case c) the same calculation holds, but the error is negative.

At the device described here the following values were fixed for a and v_2

a 360,000

v_2 . . . 10^7 Hz

From Eq. (5.2) follows that this error becomes smallest When either <u>a</u> becomes very high or the ratio of block frequency to measuring frequency decreases.

Table 5.2 shows the values of the two errors in dependence on phase and measuring frequency.

<u>Table 5.2</u>

v_1 |Hz|	ϕ |°|	$\Delta\phi_1$ |°|	$\Delta\phi_2$ |°|
10^3	3.6	±0.036	±0.2
10^3	180.0	±0.036	±0
10^4	3.6	±0.36	±0.02
10^4	180.0	±0.36	±0
10^5	3.6	±3.6	±0.002
10^5	180.0	±3.6	±0

As can be seen from Fig. 5.9, error 2 is zero at 180^o and increases with decreasing phase.

It is to be mentioned that the duration of a counting cycle is $3.6.10^{-2}$ sec; this time can be easily increased as required by means of the two MMV in Fig. 5.4.

CHAPTER 6

VALLEY MEASUREMENTS

The above-ground registration of VLF signals showed the maximum magnetic field strength always to run in direction of the mountain valleys. This effect obviously does not occur by chance because it could be proved in all by-valleys of the Inn-Valley. A thorough explanation will be given in a particular thesis.

In spring 1972 we started preparatory measurements. Several frequencies were considered (15.1; 50; 128.25; 278 kHz) to be able to recognize a possible frequency dependence. In fact, a new unexpected effect occurred. For the higher frequencies the maximum magnetic field strength was always normal to the valley direction. Fig. 1 shows these results. The contour lines show the course of the valleys in the surroundings of Innsbruck and the vectors show the direction of the maximum magnetic field strength. If the valleys become too narrow all vectors point into valley direction.

For a hollow waveguide the mode with the greatest wavelength is a TE-mode, i.e., a mode with the maximum magnetic field strength following the waveguide axis. So we tried to interprete the effects by a modified waveguide theory. The only difficulty was to recognize the valleys as hollow waveguides. In several publications /23, 24, 25/, the problem of waves over rough surfaces is solved by expanding the irregularities of the surface in Fourier-series. The wave equations are solved for sinoidal modulated surfaces and then superponed. It is evident that surface irregularities will induce new modes.

In /24/ we find waveguides of arbitrary cross section being transformed into cylindrical waveguides by means of conformal mapping. The problem now appeared rather restricted: The shape of the valley has to be transformed to a cylinder.

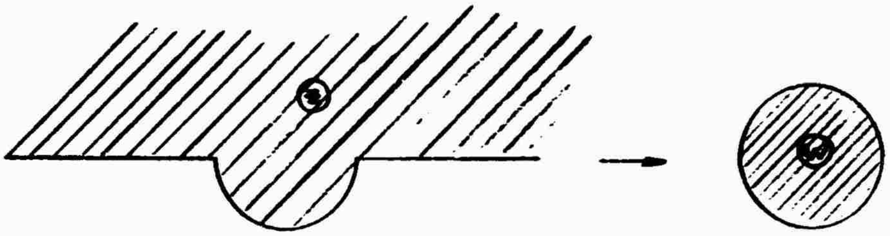

$w = f(z)$

Fig. 6.2

The exact solution requires considerable numerical expenditure. Besides, there is no plotter at Innsbruck University so that the results cannot be plotted. For the time being we have to be satisfied with an approximate solution which, however, shows good physical clearness.

The transformation:
By means of the function $w = \frac{z-i}{z+i}$ the upper semi-plane is represented onto the unit-circle of the w-plane /18, 26/.

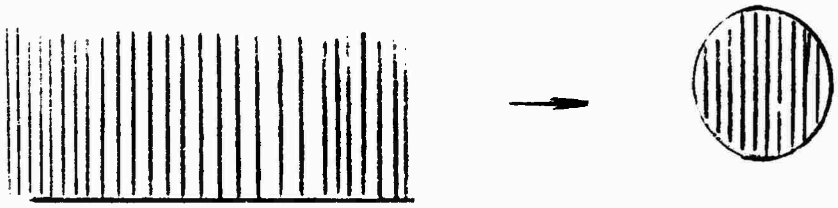

$$w = \frac{z-i}{z+i}$$

Fig. 6.3

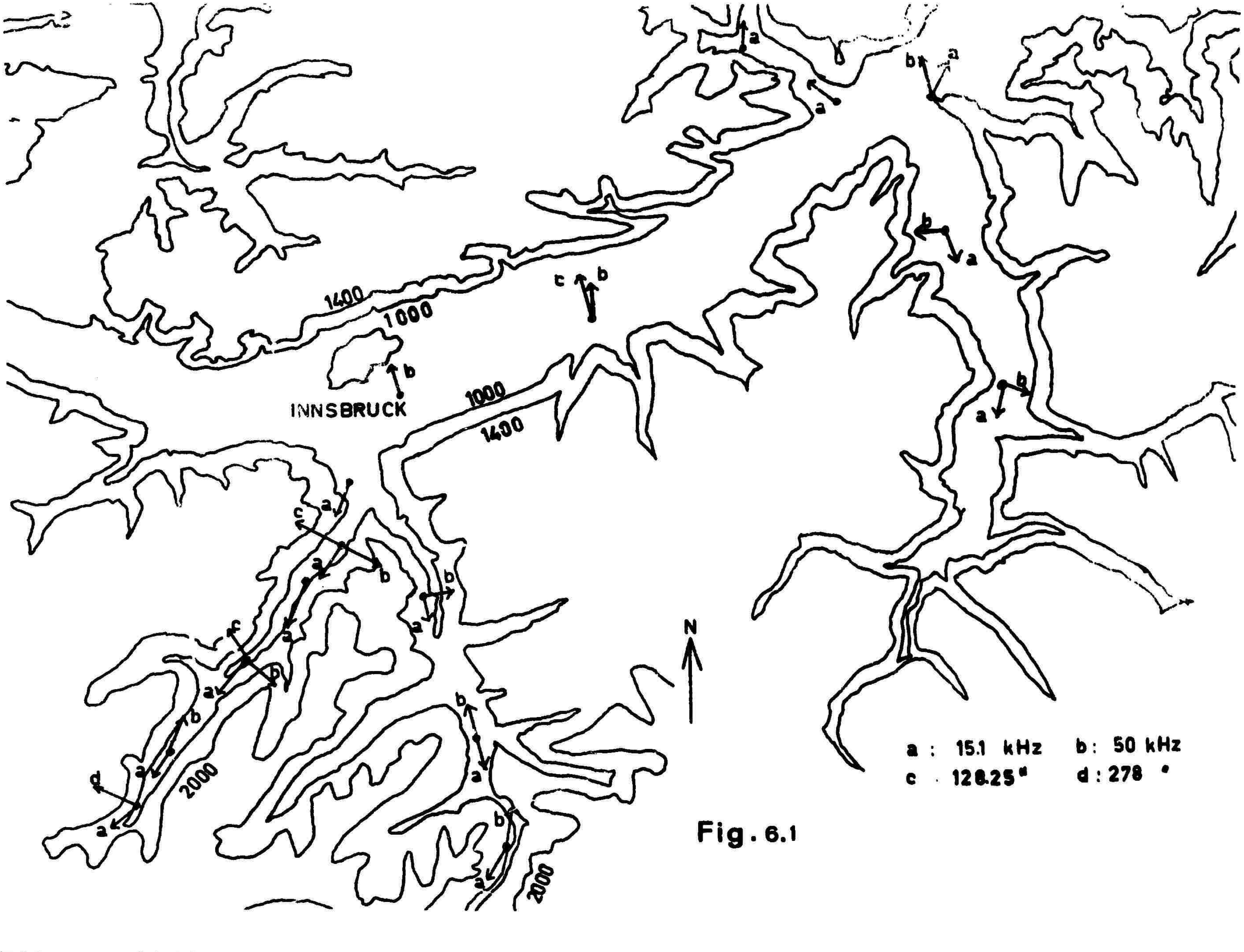
a
b a
a
b
a
c b
1400
1000
b
INNSBRUCK
1000
1400
b
a b
a
c a
a
b
b
a
a
c
b
a
b
a
d
a
2000
b
a
a
b
a
2000
N
a : 15.1 kHz b : 50 kHz
c : 128.25° d : 278°

Fig. 6.1

We choose our valley cross section in a way that it falls completely into the upper semi-plane.

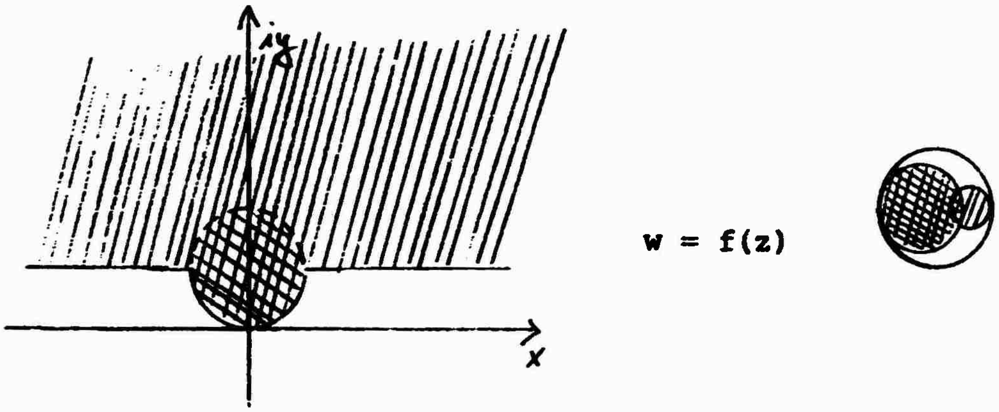

Fig. 6.4

Now the valley is transformed into the interior of two intersecting circles inside the unit circle which depend on the valley size.

Waveguides still can be described by the eigenfunctions of cylindrical waveguides, if the cross section varies slightly from a circle /24/. In our case, this means that the problem is solved principally when the valley is represented onto a fairly circular area.

The representation function reads

$$w = \frac{z - i}{z + i} \tag{6.1}$$

The circle

$$|z - ia|^2 = a^2 \tag{6.2}$$

in the z-plane is transformed into the circle

$$\left(u + \frac{1}{1 + 2a}\right)^2 + v^2 = \frac{4a^2}{(1 + 2a)^2} \tag{6.3}$$

in the w-plane.

For the straight line $Im(z) = b$ we obtain in the w-plane

$$\left(u - \frac{b}{1+b}\right)^2 + v^2 = \left(\frac{1}{1+b}\right)^2 \qquad (6.4)$$

Considering e.g. the case a = b = 3, an approximately circular representation of the valley results in the w-plane. The concentric circles to the circle K in the w-plane are representing coordinate lines in the hollow waveguide.

$$\left|w + \frac{1}{7}\right|^2 = c^2 \qquad (6.5)$$

The inverse transformation of these circles produces

$$\left|z - \frac{48 + 49c^2}{64 - 49c^2}\right|^2 = \frac{7252c^2}{(64 - 49c^2)^2} \qquad (6.6)$$

in the z-plane. These circles are shown in Fig. 6.5.

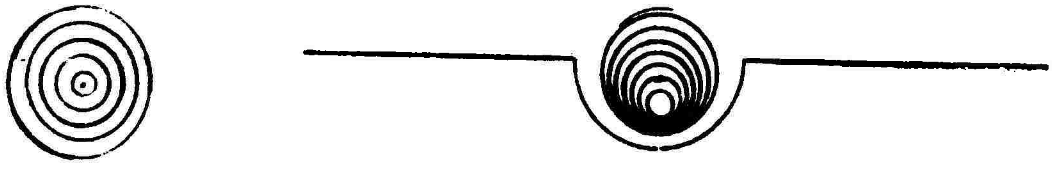

Fig. 6.5

The same results are obtained when using other values for a and b. So we can say that the transformation is independent on the size of the valley.

Conclusion

It is possible to describe a mountain valley by a cylindrical waveguide by means of conformal mapping. From Fig. 6.5 it is to be seen that near the bottom the field density is higher than in the upper regions of the valley.

An exact transformation of the valley cross section into a cylindrical waveguide is possible, but requires a computer with plotter because of the great numerical expenditure.

CHAPTER 7

A NEW METHOD OF DETERMINING THE ELECTRIC ROCK PARAMETERS ε_r AND σ

7.1 General considerations

The procedures of determining ε_r and σ listed below are based on the dependence of the field strength on

1) the dipole moment $\vec{m}$
2) the distance R between point of reception and transmitter
3) the frequency f
4) the dielectric constant ε_r
5) the conductivity σ

$$\vec{H} = \vec{H}(\vec{m}, r, f, \varepsilon_r, \sigma) \qquad (7.1)$$

$\vec{H}$ ... magnetic field strength vector

To restrict this complexity it is necessary to conduct the measurement in a way that as many of these parameters as possible are kept constant.

Furthermore, we have to consider the problem whether and how much the individual parameters depend on each other.

a) Since $|\vec{m}| = n \cdot I \cdot F$ can always be kept constant by readjusting the antenna current, the dependence

$$|\vec{m}| = |\vec{m}|(\varepsilon_r, \sigma)$$

that might possibly arise by attenuating the transmitting antenna operated in resonance, is only of theoretical interest for our case.

b) It is obvious that

$$\varepsilon_r \neq \varepsilon_r(\vec{m}); \quad \sigma \neq \sigma(\vec{m}); \quad f \neq f(\vec{m}); \text{ and } \quad R \neq R(\vec{m})$$

c) The question for the dependence

$$\varepsilon_r \overset{?}{=} \varepsilon_r(R) \quad \text{and} \quad \sigma \overset{?}{=} \sigma(R),$$

however, has to be discussed more thoroughly which is to be illustrated by means of the following figures (Figs. 7.1a and 7.1b).

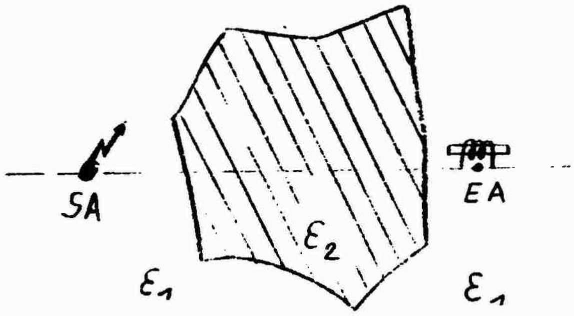

Fig. 7.1a

In the first case (Fig. 7.1a) transmitter and receiver are so close together that solely the dielectric constant ε_1 of the inhomogeneous island in between holds responsible for the field at the point of reception. If the measuring distance is enlarged the surrounding medium characterized by ε_2 becomes more and more effective. The resulting dielectric constant ε_{res} influencing the field of reception is composed of ε_1 and ε_2. Fig. 7.1b will illustrate this situation. It was on purpose that all disturbing bodies were drawn with equal magnitude and shape to make clear then even then ε_{res} is depending on the distance. In reality these islands will be of different size and have a different dielectric constant, too.

The distance dependence for ε_r and σ (of course, we can reflect in the same way on the conductivity) can thus be regarded as a fact. The dielectric constant (or conductivity, respectively) determined over a certain measuring distance is a mean value of all dielectric constants (or conductivities) of this region.

It is therefore senseless to compare specific values of dielectric constant (or conductivity), unless they are related to a certain distance. Consequently, listed values given by different authors can only be regarded as approximations and it is necessary to compare measuring methods and conditions, too.

d) The dependence

$$\varepsilon_r \overset{?}{=} \varepsilon_r(f) \quad \text{and} \quad \sigma \overset{?}{=} \sigma(f)$$

is of great importance with regard to the two-frequency method discussed below. The frequency dependence of ε_r and the consequent dependence of the index of refraction on the frequency is called "dispersion" in optics. In this case, however, wavelengths involved are so small that they can be compared with molecules and resonance vibrations occur. At low frequencies there are no such vibrations; the approximate limit lies at about 30 MHz (λ_0 = 10 m, SW-band). Below this frequency, calculations are performed with the static value of the dielectric constant.

In contrast to this assumption a certain frequency response was observed in the lower frequency range ($f < 100$ kHz) owing to the so-called partition polarization. Among others, STRUTT /27/ and recently WÖBKING /28/ and GRISSEMANN /29/ have observed this phenomenon. In /28/ and /29/, the (ε_r,f) and the (σ,f)-diagrams show a flattening of the curves towards higher frequencies ($f > 100$ kHz)

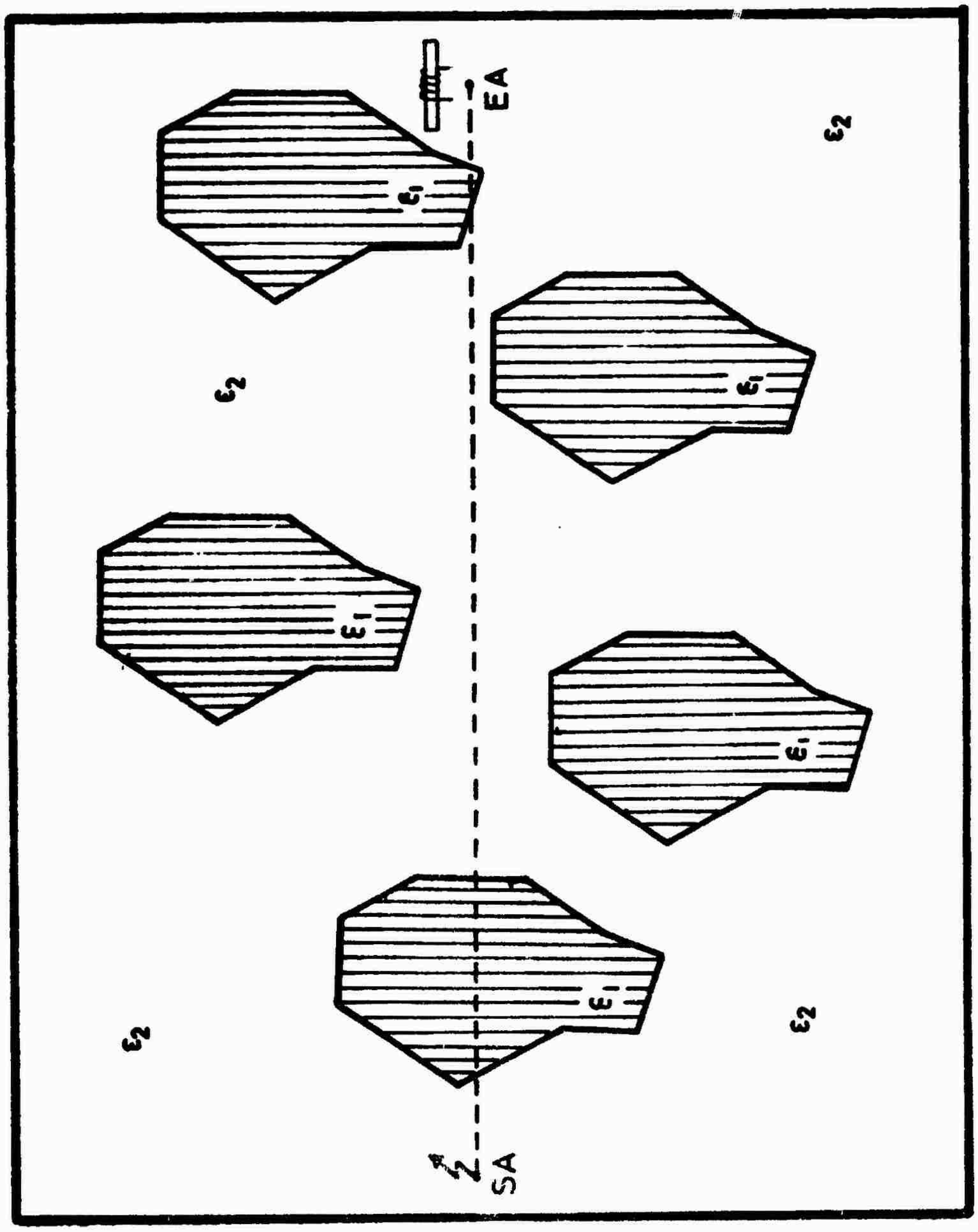
EA
SA
ε_1
ε_1
ε_1
ε_1
ε_1
ε_2
ε_2
ε_2
ε_2

FIG. 7.1b

Whether or not the two-frequency method is admissible for the determination of ε_r and σ depends on the above conclusions.

For a comparison let us briefly refer to methods that have already been worked out by co-workers of the VLF-Project:

7.2 Method according to NESSLER /10/

If the relative value G (to be defined below) is plotted as ordinate for a definite frequency and a definite measuring distance every point in the diagram will constitute a pair of values (ε_r, σ) belonging together. To obtain H_{90} we must know exactly the properties of the receiving equipment,and the calibration factor establishing the interrelation between actual field strength and measured voltage must be determined as accurately as possible. Since the calibration factor comprises quite a number of measuring values, the uncertainty factor is rather high. The resolving power of the method is, however, good even at small measuring distances of about 20 m.

7.3 Method according to KELLNER /14/

Based on an adequate representation of the formulas for the vector components of the field strength, KELLNER /14/ found a possibility to determine the complex wave number from relative values and thereby calculate ε_r and σ.

The main disadvantage of this method is its failure in the inhomogeneous measuring site. According to the author, the method can only be used up to a frequency of about 350 kHz and a measuring distance of 50 m. This is due to the fact that with decreasing wave length the inhomogenities form an ever increasing hindrance for the field which thus is more and more distorted. It is chiefly the bearing angle ψ indicating the direction of maximum field strength and playing a dominating role in the evaluation formulas that is distorted, thus heavily falsifying the result.

7.4 New Method according to KLEIN /17/ Two-frequency method

To be able to make quantitative statements on the behavior of electromagnetic waves penetrating zones of inhomogenity it is necessary to know the electric rock parameters ε_r and σ. Real and imaginary parts of the complex wave number k^* and of the complex refraction index n^* can be calculated from these parameters. Therefore we had to find a method delivering workable results even in an inhomogeneous medium.

The following requirements had to be fulfilled:

1) The method must be practicable in inhomogeneous medium.
2) In its formulas and diagrams it should contain only quotients of absolute measuring values.

A favorable application of a possible method made us request two more conditions:

3) Measurements should be able to be conducted easily and quickly.
4) The values ε_r and σ to be determined should possibly be readable at the measuring site thus enabling a short-time change in the measuring program.

A solution of these problems was found using the field strength ratio G (as was done with the two methods described above) considering, however, two different measuring frequencies. According to /10/ G is defined as

$$G = \frac{H_0}{H_{90}} = \frac{H_R}{H_\theta} \tan\theta \qquad (7.2)$$

H_0 ... field strength maximum at $\theta = 0^\circ$

H_{90} .. field strength maximum at $\theta = 90^\circ$

H_R ... field strength in the direction towards the transmitting antenna

H_θ ... field strength vertical to H_R

θ .... angle between transmitting antenna and radius vector

Since the field strength vector $\vec{H}$ and thus all its components depend on frequency, dielectric constant, conductivity, and distance to the transmitter

$$G = G(f, \varepsilon_r, \sigma, R)$$

Owing to the above mentioned reasons the measuring distance transmitter - point of reception must be kept constant, i.e.

$$G = G(f, \varepsilon_r, \sigma)$$

The above mentioned frequency independence of ε_r and σ at one and the same measuring distance reduces the dependence of G to

$$G = G(f)$$

at ε_r = const. and σ = const.

If groups of curves with the parameters ε_r and σ, resp., are plotted in a diagram with the ordinate $G = G(\varepsilon_r,\sigma)$ at a frequency f_1 and with the abscissa $G = G(\varepsilon_r,\sigma)$ at a frequency f_2, every point of intersection of the ε_r-parameter group with the σ-parameter group constitutes a (ε_r,σ)-pair of values belonging definitely together.

For our measurements, the following values were chosen: f_1 = 500 kHz; f_2 = 1000 kHz; R = 100 m (50 m), thereby taking into consideration the geometry of the gallery, the resolving power at a definite measuring distance (splitting of the curves of the diagram), and the power of the transmitter. For G(500) (i.e. G at 500 kHz) and G(1000) (i.e. G at 1000 kHz) determined by measurement, dielectric constant and conductivity can be taken from Fig. 7.2. For other measuring distances and frequencies corresponding diagrams have to be plotted.

There are three possibilities to measure G:

a) With the relation

$$G = \frac{H_R}{H_\theta} \tan\theta$$

any angle position θ of the transmitting antenna is admissible. For $\theta \rightarrow 90^\circ$, $\tan\theta \rightarrow \infty$, i.e., the determination of G becomes inaccurate for large values of θ.

b) If = 45°

$$G = \frac{H_R}{H_\theta}$$

thus considerably reducing measuring expenditure, because only the frequency has to be interchanged.

c) Using the relation

$$G = \frac{H_0}{H_{90}}$$

the transmitting antenna is first adjusted to $\theta = 0^\circ$ and then to $\theta = 90^\circ$. At both positions the maximum field strength is measured for both frequencies.

Out of these three possibilities it is the third one that offers the decisive advantage in comparison to the methods by NESSLER and KELLNER.

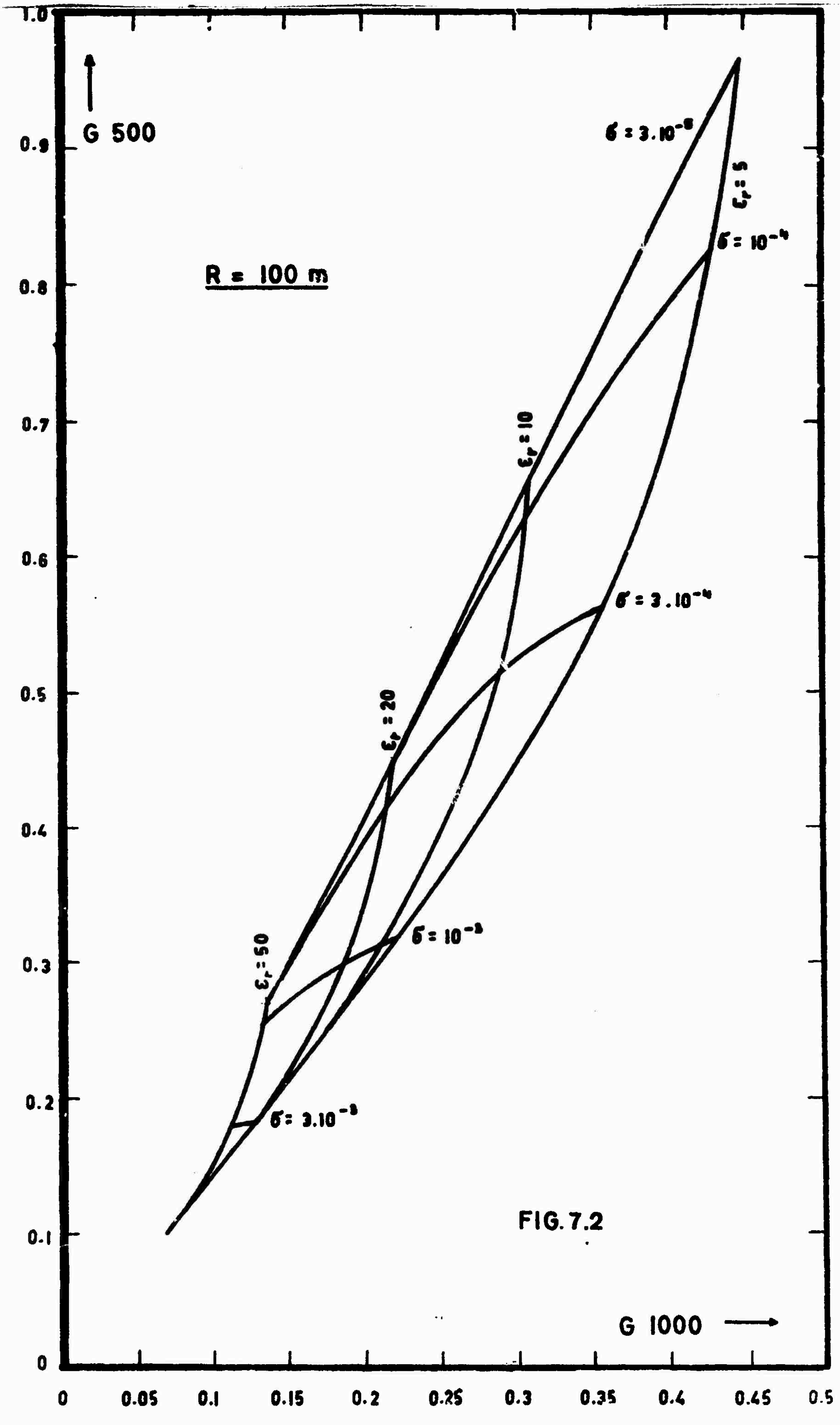

G 500
R = 100 m
$\sigma = 3.10^{-5}$
$\varepsilon_r = 5$
$\sigma = 10^{-4}$
$\varepsilon_r = 10$
$\sigma = 3.10^{-4}$
$\varepsilon_r = 20$
$\sigma = 10^{-3}$
$\varepsilon_r = 50$
$\sigma = 3.10^{-3}$
G 1000
1.0
0.9
0.8
0.7
0.6
0.5
0.4
0.3
0.2
0.1
0
0.05
0.1
0.15
0.2
0.25
0.3
0.35
0.4
0.45
0.5

FIG. 7.2

Both for $\theta = 0^{\circ}$ and for $\theta = 90^{\circ}$ the field is linearly polarized. When measuring, the H_0 and H_{90} directions are sought and the amount is measured. That is why a deviation owing to disturbances can by no means influence the accuracy of the value $G = H_0/H_{90}$.

7.5 Practical application of the new method

Numerous measurements were executed in the mine of St.Gertraudi. Whereas for most measuring sites a homogeneous rock structure could be assumed, the measurements in "Morgenschlag" produced (cf. Fig. 7.3) surprisingly different values; results are listed in Table 1.

Table 1: R = 100 m

exp. no.	measuring distance	f [kHz]	U_0 [μV]	U_{90} [μV]	G(500) G(1000)	ε_r	σ [S/m]
97	M8.2 - M12	500 1000	290 78	880 420	0.33 0.19	20	$9\cdot10^{-4}$
101	M12 - M8.2	500 1000	505 165	1300 810	0.39 0.21	20	$5\cdot10^{-4}$
100	M11.3 - M9	500 1000	490 108	790 390	0.62 0.28	12	10^{-4}
104	M9 - M11.3	500 1000	485 120	780 400	0.62 0.30	10	10^{-4}
99	M11.3-M11	500 1000	125 55	138 143	0.91 0.39	8	$6\cdot10^{-5}$
103	M11-M11.3	500 1000	445 120	610 360	0.73 0.33	8	$8\cdot10^{-5}$
98	M11.3-M12	500 1000	530 92	510 205	1.04 0.45	4	$2\cdot10^{-5}$
102	M12-M11.3	500 1000	480 85	510 210	0.94 0.41	6	$5\cdot10^{-5}$

The number of experiment refers to Fig. 7.3. On comparing exp. no. 97 with exp. 98 perpendicular thereto we realize that the two dielectric constants are 5 : 1, the conductivities, however, nearly 50 : 1. From these remarkable differences we can draw the conclusion that a disturbance runs through the medium. The recognition of such disturbances means a real advantage for geological prospecting. The method described above together with the method of images thoroughly discussed in /17/ has already produced promising results.

7.6 A further possibility to locate disturbing zones in rock

The following characteristic resulted from the forementioned measurements for the determination of the electric rock parameters ε_r and σ in "Morgenschlag":

At the execution of measurement 106 (78) (cf. Fig. 7.3) from M8.2 to M12 the direction of maximum field strength (major axis of receiving ellipse) rotates by 180° together with the rotation of the transmitting antenna whereas at measurements perpendicular thereto the maximum field strength shows some kind of pendulous motion. The rotation occurring in one direction up to a certain angle of rotation θ of the transmitting antenna suddenly reverses so that the receiving antenna tilts back to the starting position without having done a 180°-rotation.

Fig. 7.4 illustrates quite clearly this extraordinary behavior. The curves do not proceed - as could be expected from theory - from the first to the third quadrant, but from the first to the second one at the forward measurement and from the fourth to the third quadrant at the backward measurement (with exchanged transmitter and receiver).

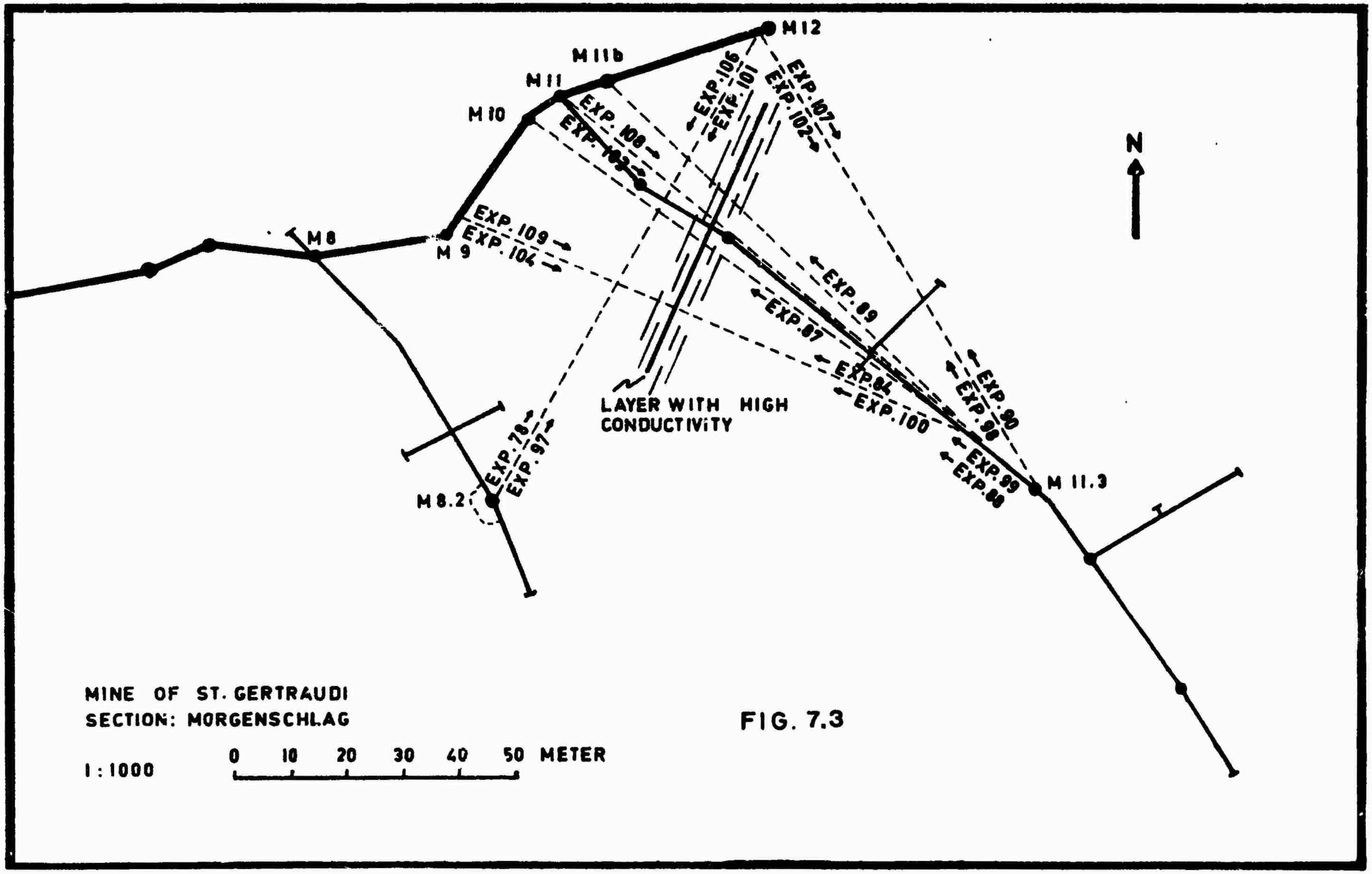
M12
M11b
M11
M10
M 9
M8
M 8.2
M 11.3
N
EXP.106
EXP.101
EXP.107
EXP.102
EXP.108
EXP.103
EXP.109
EXP.104
EXP.89
EXP.87
EXP.84
EXP.100
EXP.90
EXP.98
EXP.99
EXP.88
EXP.78
EXP.97
LAYER WITH HIGH
CONDUCTIVITY
MINE OF ST. GERTRAUDI
SECTION: MORGENSCHLAG
1:1000
0
10
20
30
40
50 METER

FIG. 7.3

74-B

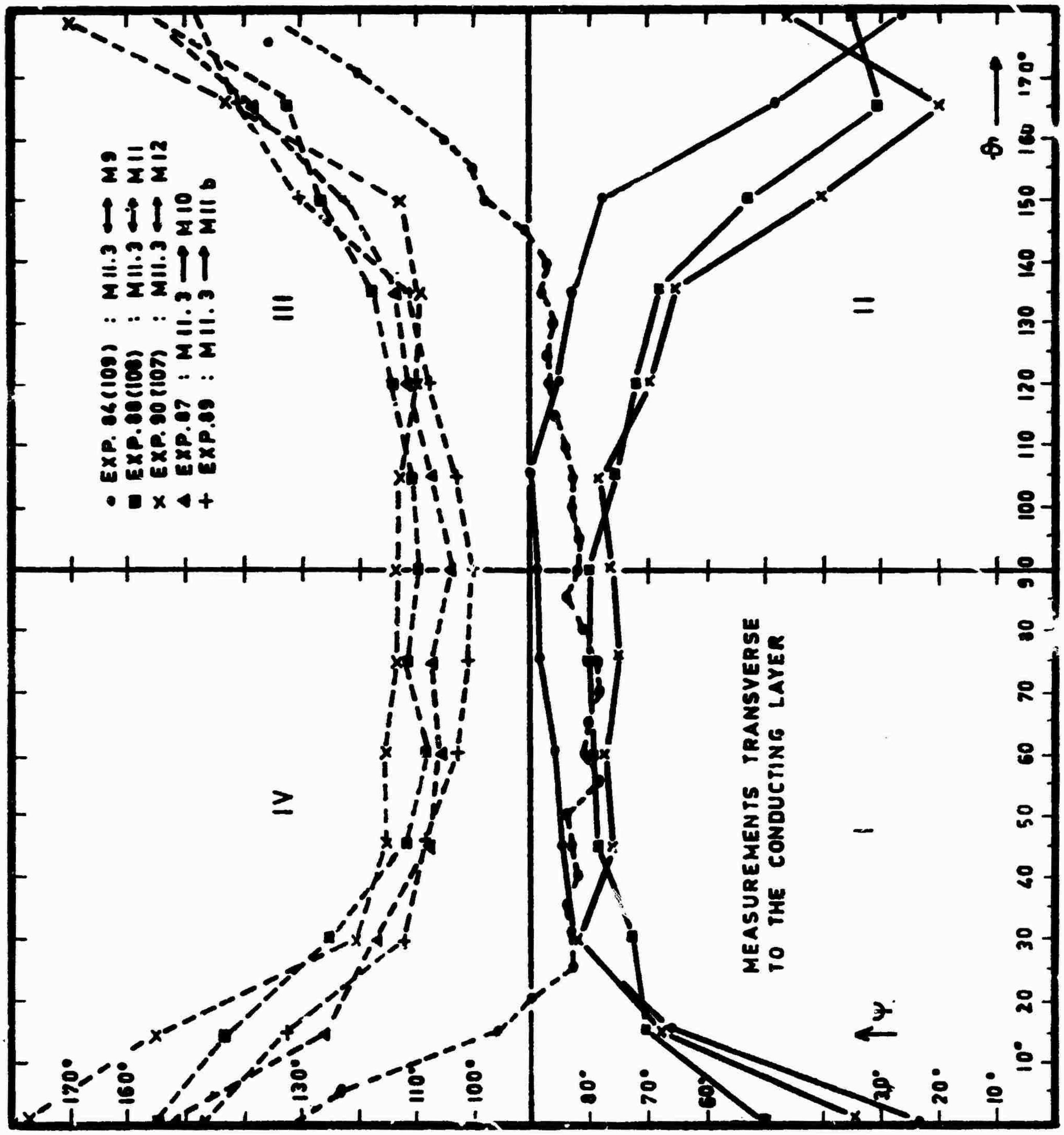

• EXP. 84(109) : M11.3 ⟷ M9
■ EXP. 88(108) : M11.3 ⟷ M11
× EXP. 90(107) : M11.3 ⟷ M12
▲ EXP. 87 : M11.3 ⟶ M10
+ EXP. 89 : M11.3 ⟶ M11 b
III
II
IV
I
MEASUREMENTS TRANSVERSE
TO THE CONDUCTING LAYER
ψ
ϑ
10°
20
30
40
50
60
70
80
90
100
110
120
130
140
150
160
170°
10°
20°
30°
60°
70°
80°
100°
110°
130°
160°
170°

FIG. 7.4

The curve of the backward measurement is, as it were, the "image" of the forward measurement curve.

An exact, purely mathematical description of this effect would be extremely difficult, because too many unknown quantities or variables are involved. Certainly, numerous papers were published on this subject but finally calculations are always based on the assumption of quite special facts. The main object of our method, however, was to give at least a qualitative explanation for the "pendulous motion" by means of a clearly arranged geometrical construction using the method of images.
The development of the theory was stimulated by /37, 38, 39, 40/.

7.7 Theory of images

If a quiescent charge is situated in direct neighborhood of a conducting infinite surface a field distribution according to Fig. 7.5a results. This consideration shall apply analogously for moved charges (Fig. 7.5b). The relation between the magnetic dipole moment and its image is shown in Fig. 7.5c.

There are two measuring possibilities in the neighborhood of a disturbing zone:

Type 1: Measurement approximately parallel to disturbing zone

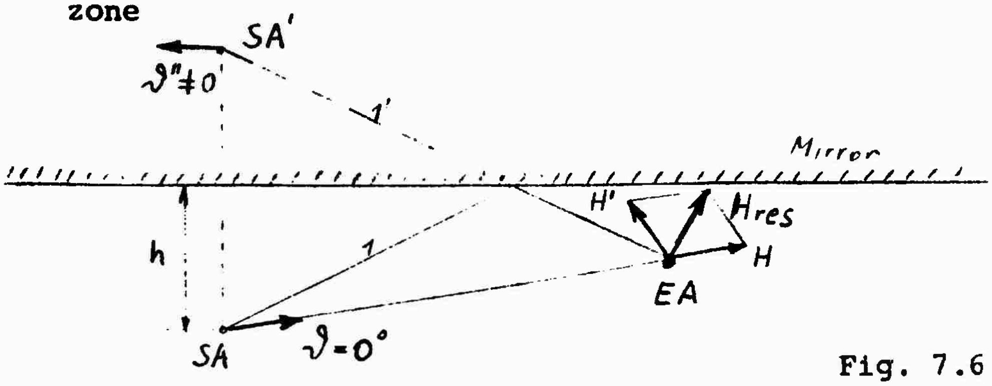

Fig. 7.6

Let SA' be the mirror image of SA. At EA, two signals are received superponing one another. The two field vectors $\vec{H}$ and $\vec{H}'$ generally having different directions form a resulting vector $\vec{H}_{res}$ with another direction.

<u>Type 2:</u> The conducting zone is situated between transmitting antenna and receiver

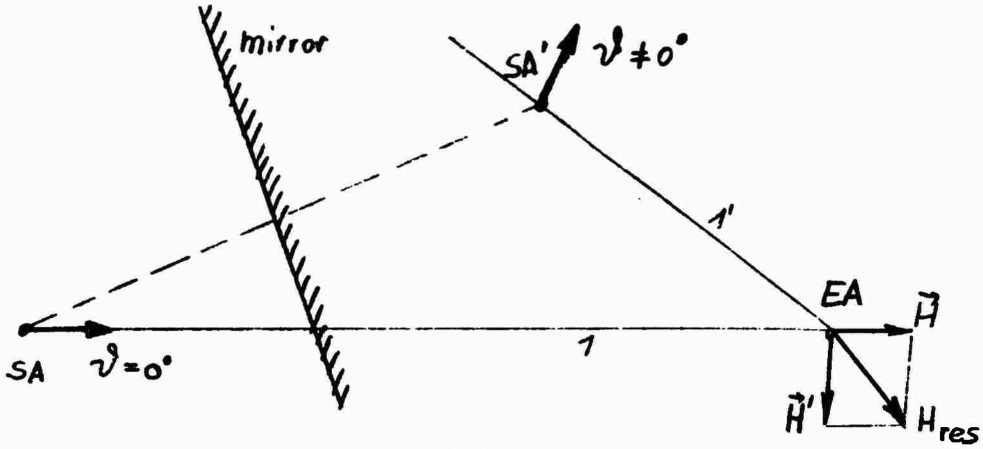

Fig. 7.7

Here, the image SA' develops from the charge distribution induced by SA in the conducting layer and acting as an image of SA at SA'. The field strength at EA is again composed of the signal originating at SA and SA'.

The good agreement between theory and experiment shall be shown by means of two examples:
Fig. 7.8 is an example for type 1. The measuring distance is parallel to the disturbance determined in "Morgenschlag".

Fig. 7.9 represents type 2 with the disturbance between transmitter and receiver.

From the above figures we recognize that the auxiliary vector $\vec{H}'$ explains rather well the deviating direction of $\vec{H}_{ex}$.

If, however, $\vec{H}$ and $\vec{H}'$ include an angle of approximately

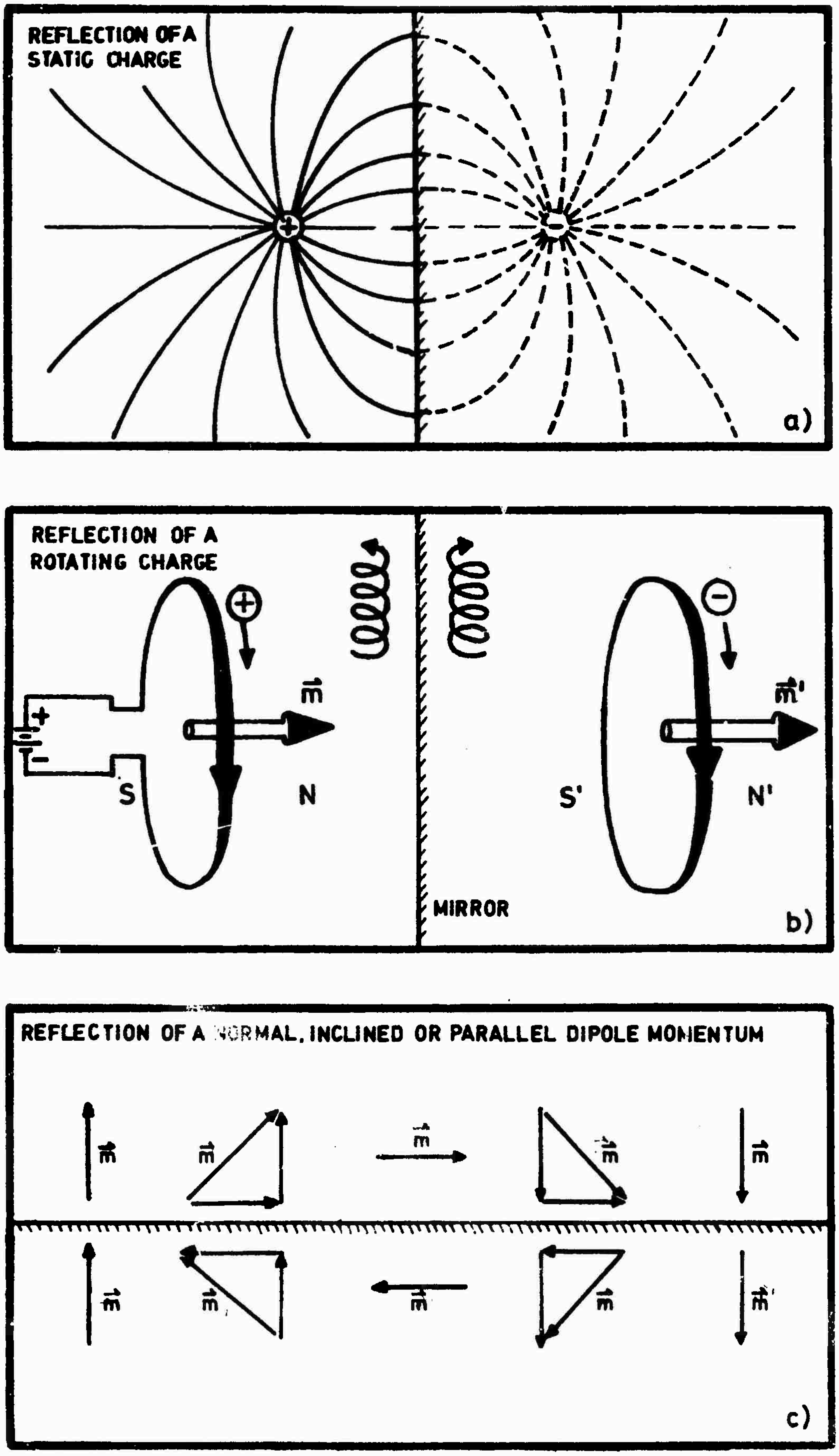
REFLECTION OF A STATIC CHARGE
+
−
a)
REFLECTION OF A ROTATING CHARGE
+
−
$\vec{m}$
+
−
S
N
$\vec{m}'$
S'
N'
MIRROR
b)
REFLECTION OF A NORMAL, INCLINED OR PARALLEL DIPOLE MOMENTUM
$\vec{m}$
$\vec{m}$
$\vec{m}$
$\vec{m}$
$\vec{m}$
$\vec{m}$
$\vec{m}$
$\vec{m}$
$\vec{m}$
$\vec{m}'$
c)

FIG. 7.5

EXP. 106 (M 12 → M 8.2) G = 0.2 $\chi = 7°$

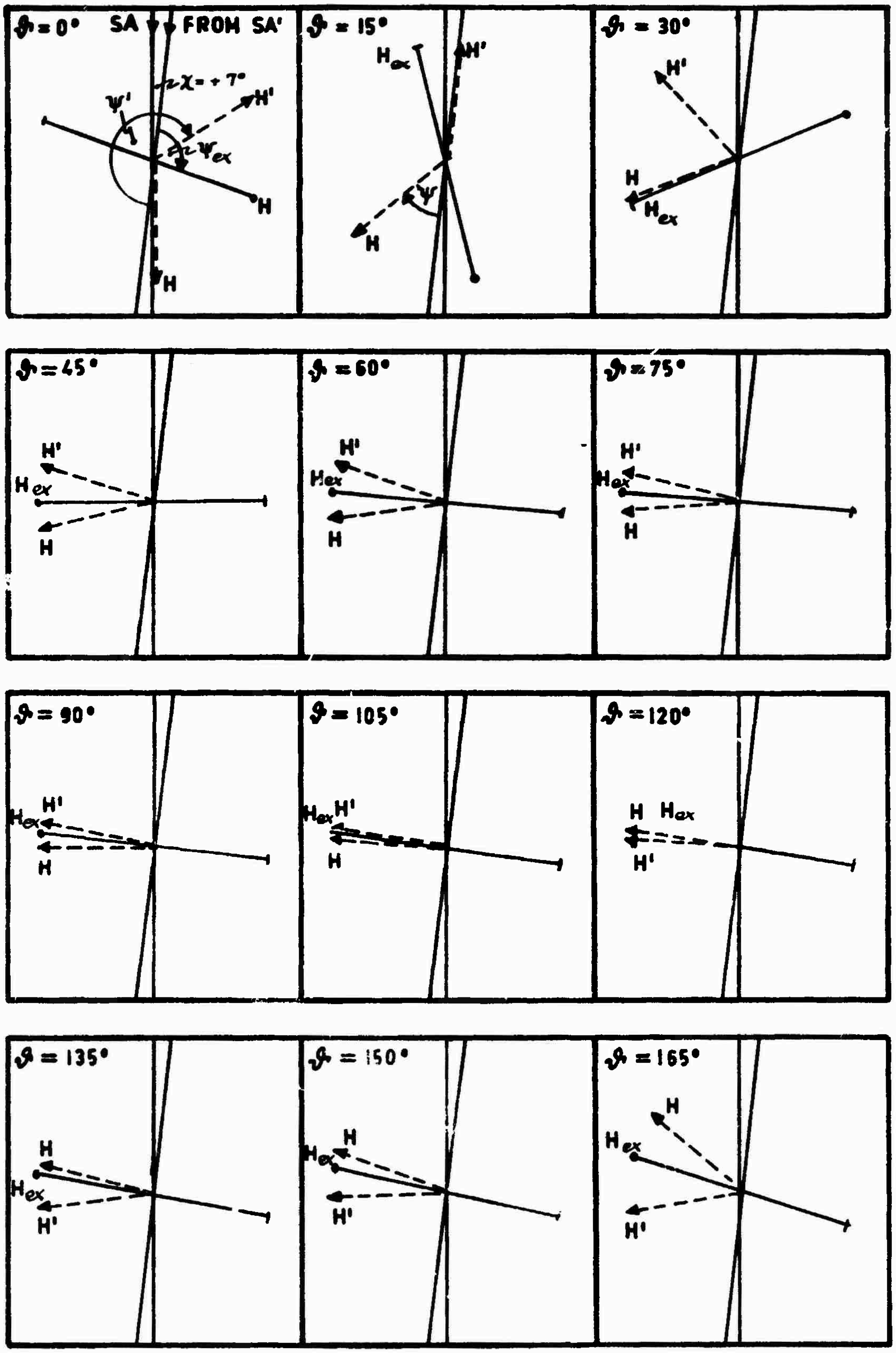

FIG. 7.8

EXP. 88 (M 11.3 → M 11) G = 0.3 $\chi = 117°$

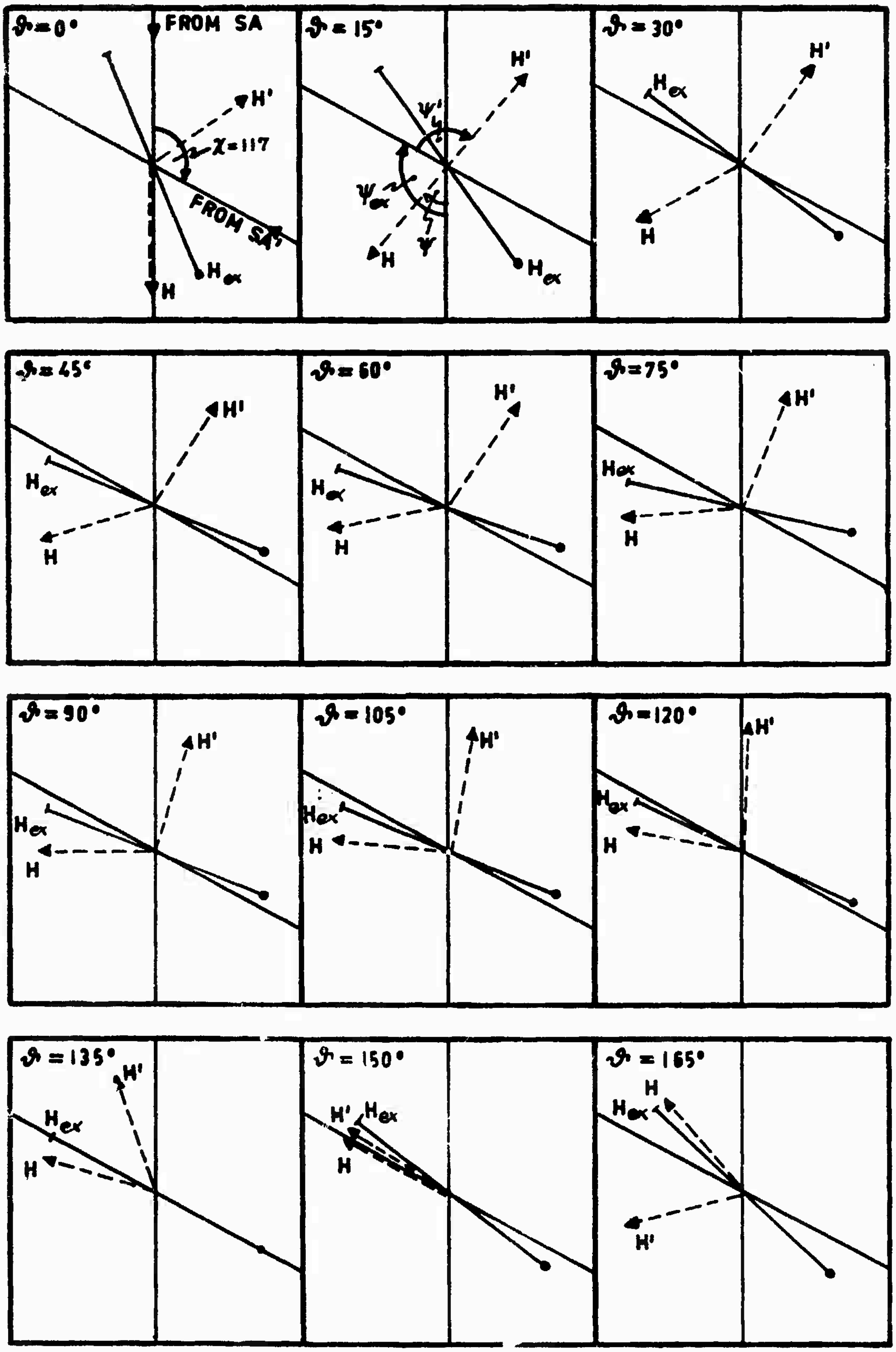

FIG. 7.9

180° some difficulties in interpretation will arise. The direction of the resulting vector $\vec{H}_{ex}$ coincides with $\vec{H}$ or $\vec{H}'$ at type 1 (exp. no. 106), whereas $\vec{H}_{ex}$ is perpendicular to $\vec{H}$ and $\vec{H}'$ at type 2 (exp. no. 88). So we have to assume that a phase reversal in respect to $\vec{H}'$ (or $\vec{H}$) occurs at the second case, thereby giving a good explanation for the pendulous motion characterized by the reversal of rotation.

The method developed in the mine of St. Gertraudi was already successfully applied in other mines (Schwaz/Tyrol, Bleiberg/Carinthia) thereby confirming our theory. A commercial application of this method for ore prospecting, however, would require further experiments to investigate the influence of watercourses, rails, and other technical equipment.

CHAPTER 8

ENTERING MECHANISM OF ELECTROMAGNETIC WAVES INTO A DISSIPATIVE MEDIUM

8.1 Introduction

In December 1972 the investigations on this subject were finished. The basic theory which will be briefly referred to was already published in Final Report 1971 together with the development of an autorange receiver.

Problem:

Measurements /11/ of the broadcasting transmitter Ö-Regional along a gallery of the mine St. Gertraudi showed a local period of the maximum magnetic field strength (major axis of a rotary field ellipse). The transmitter (629 kHz) is situated at a distance of 30 km from the mine.

Repeated measurements confirmed this unexpected result which was tried to be explained /30/ by developing a theory for an electromagnetic wave with oblique incidence on a boundary surface.

8.2 Equations of the magnetic field strength in medium

The equations used by Schumann /30/ are specified in /11/. For $\vec{H}$ polarized in the direction of the plane of incidence (in air) they take the form

$$\begin{aligned} E_z(x,y) &= E_s^e \exp\{j\omega t + f(x,y)\} \\ H_x(x,y) &= -E_s^e \frac{\cos\phi_1}{W_1} \exp\{j\omega t + f(x,y)\} \qquad (8.1) \\ H_y(x,y) &= -E_s^e \frac{\sin\phi_1}{W_1} \exp\{j\omega t + f(x,y)\} \end{aligned}$$

for $\vec{H}$ polarized vertically to the plane of incidence (in air) they read:

$$
\begin{aligned}
H_z(x,y) &= H_s{}^e \exp\{j\omega t + f(x,y)\} \\
E_x(x,y) &\approx H_s{}^e \cdot W_1 \cos\phi_1 \exp\{j\omega t + f(x,y)\} \qquad (8.2) \\
E_y(x,y) &= H_s{}^e \cdot W_1 \sin\phi_1 \exp\{j\omega t + f(x,y)\}
\end{aligned}
$$

$E_s{}^e$ ... electric field strength of the incoming wave
$H_s{}^e$ ... magnetic field strength of the incoming wave
W_1 .... wave resistance in air = 377 Ω
ϕ_1 .... angle of incidence
ω ..... circular frequency

With the boundary conditions the complex law of Snellius is obtained

$$
\begin{aligned}
\sin\phi_1 &= \frac{W_1}{W_2} \sin\phi_2 \\
W_2 &= \rho_{W_2} \exp\left|j^{\alpha/2}\right| \\
\rho_{W_2} &= \frac{\omega \cdot \sqrt{\mu_2 \varepsilon_2}}{c_0 \sqrt{\sigma^2 + \omega^2 \varepsilon_0^2 \varepsilon^2}} \sqrt[4]{1 + \left(\frac{\sigma}{\omega \varepsilon_0 \varepsilon_2}\right)^2} \qquad (8.3) \\
\alpha &= \arctan \frac{\sigma}{\omega \varepsilon_0 \varepsilon_2}
\end{aligned}
$$

W_2 .... wave resistance in medium (rock)
ε_2 .... dielectric constant in medium
ε_0 .... absolute dielectric constant
μ_2 .... permeability in medium (rock)
σ .... conductivity in medium (rock)
c_0 .... vacuum light velocity

From the boundary conditions we can conclude the complex transmission coefficients for the case of parallel polarization $(1+\Gamma_p)$ and vertical polarization $(1+\Gamma_v)$, respectively

$$1+\Gamma_p = \frac{2\cos\phi_1}{\cos\phi_1 + W_1\sqrt{\frac{1}{W_2^2} - \frac{1}{W_1^2}\sin^2\phi_1}}$$

$$1+\Gamma_v = \frac{\left(\frac{W_1}{W_2}\right)^2\cos\phi_1 - \sqrt{\left(\frac{W_1}{W_2}\right)^2 - \sin^2\phi_1}}{\left(\frac{W_1}{W_2}\right)^2\cos\phi_1 + \sqrt{\left(\frac{W_1}{W_2}\right)^2 - \sin^2\phi_1}} \qquad (8.4)$$

The equations can be simplified to

$$1+\Gamma_p = \rho_{1+\Gamma_p}\, e^{j\zeta_p}$$

$$1+\Gamma_v = \rho_{1+\Gamma_v}\, e^{j\zeta_v} \qquad (8.5)$$

After laborious calculations the following equations for the magnetic field strength are obtained

$$H_x{}^d = \rho_{1+\Gamma_p}\sqrt{\rho}\cdot W_1\cdot H_p^0\cdot e^{\psi}\cdot\exp\{j|\omega t + \pi + (\theta_p - \xi/2|\}$$

$$H_y{}^d = \rho_{1+\Gamma_p}\cdot\sin\phi_1\cdot H_p^0\cdot e^{\psi}\exp\{j|\omega t + \pi + \theta_p|\} \qquad (8.6)$$

$$H_z{}^d = \rho_{1+\Gamma_v}\cdot H_v^0\cdot e^{\psi}\cdot\exp\{j|\omega t + \varsigma_p - \zeta_p + \zeta_v - \Omega|\}$$

$\rho_{1+\Gamma_p}$ ... amount of the transmission coefficient of the electric field strength with $\vec{H}$ polarized parallel to the plane of incidence

$\rho_{1+\Gamma_v}$ ... amount of the transmission coefficient of the magnetic field strength with $\vec{H}$ polarized vertically to the plane of incidence

$\psi=\psi(x,y)$ attenuation factor

$\theta_p=-\vec{k}\,\vec{x}$ .. position function of the phase

$\vec{k}$ .... vector of wave number

H_p^o, H_s^o ... amplitudes of the magnetic field strength of the incoming elliptically polarized wave

ζ_p, ζ_s ... phases of the complex transmission coefficients

Ω .... phase shift of the incoming elliptically polarized field

Furthermore,

$$\begin{aligned} \sqrt{\rho} &\sim \frac{1}{\rho_{W_2}} \\ \xi &\sim -\alpha \end{aligned} \tag{A}$$

is valid with high accuracy (error less than 1 %).

In the following paragraph the reasons leading to a local periodicity are dealt with.

8.3 Reasons for the local periodicity

Assumption:

The rock is no longer assumed to be homogeneous but bearing a reflecting layer which is shown in Fig. 3a. By superposition of the incoming and the reflected wave a local periodicity is generated. Further calculations show the possibility of determining the angle between reflected layer and gallery axis from the three occurring modes:

a) $\vec{k}_r$ in the first quadrant of the complex
period only in z'-direction. Since $k_{x',r}$ has the same direction as $k_{x'}$ no periodicity can occur in x'-direction.

b) $\vec{k}_r$ in the second quadrant
   x'- and z'-periodicity. $k_{x',r}$ and $k_{z',r}$ are antiparallel to $k_{x'}$ and $k_{z'}$.

c) $\vec{k}_r$ in the third quadrant
   period only in x'-direction. $k_{x',r}$ antiparallel to $k_{x'}$, $k_{z',r}$ parallel to $k_{z'}$.

(The dashed quantities relate to the coordinate system determined by the gallery system.)

Fig. 3b shows the possible modes.

The following relations between the angles can be read from Fig. 3a:

$$\begin{aligned}
&\text{a)}\quad 0 < \kappa = \frac{\pi}{2} + 2\gamma - \theta < \frac{\pi}{2} \\
&\text{b)}\quad 0 < \kappa = \frac{\pi}{2} + \theta - 2\gamma < \frac{\pi}{2} \qquad (8.7) \\
&\text{c)}\quad 0 < \kappa = 2\gamma - (\theta + \frac{\pi}{2}) < \frac{\pi}{2}
\end{aligned}$$

8.4 Determination of γ

From

$$\theta_p = -\vec{k}\vec{x}$$

$k_{x'}$ and $k_{z'}$ can be obtained.

$$k_{x'} = \frac{1}{377}\,\mu\mu_0\omega\sqrt{1 - \frac{\cos^2\phi_1}{\sin^2\tau}} \qquad (8.8)$$

$$k_{z'} = \frac{1}{377}\,\mu\mu_0\omega\cos\phi_1\,\frac{\cos^2\tau}{\sin\tau} + \sin\tau\,\frac{\omega\sqrt{\varepsilon\mu}}{c_0\sqrt{2}}\sqrt{1 + \sqrt{1 + \left(\frac{\sigma}{\omega\varepsilon_0\varepsilon}\right)^2}} \qquad (8.9)$$

τ .... slope angle

ϕ_1 ... angle of incidence

σ ... rock conductivity

ε ... dielectric constant of the rock

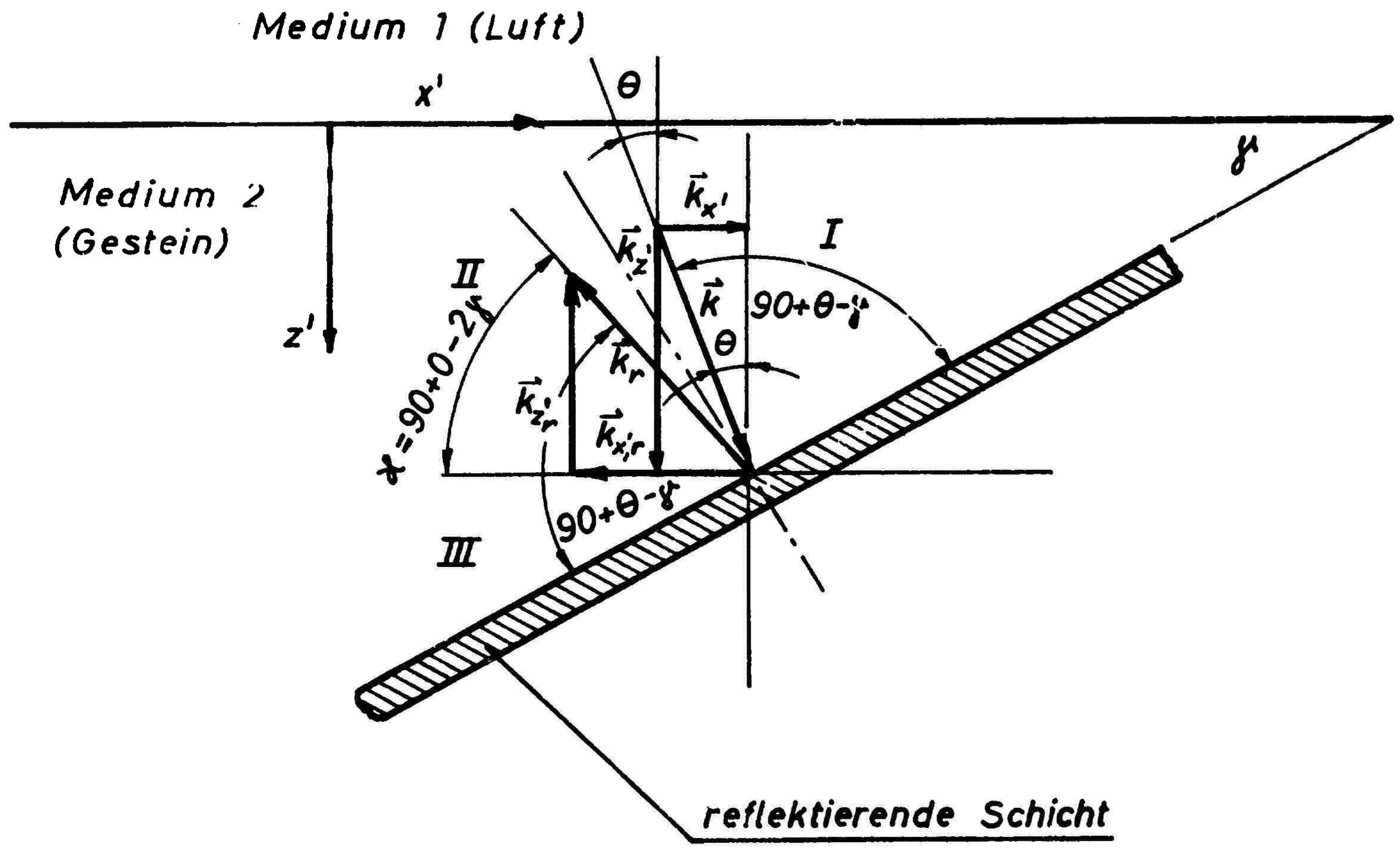
Medium 1 (Luft)
x'
Θ
γ
Medium 2
(Gestein)
$\vec{k}_{x'}$
$\vec{k}_{z'}$
I
II
$\vec{k}$
90+Θ-γ
z'
Θ
$\vec{k}_r$
$\vec{k}_{z'r}$
$\vec{k}_{x'r}$
α=90+Θ-2γ
90+Θ-γ
III
reflektierende Schicht

Fig. 3a

Wellentypen, die bei Anwesenheit einer reflektierenden Schicht im Medium 2 dort auftreten können

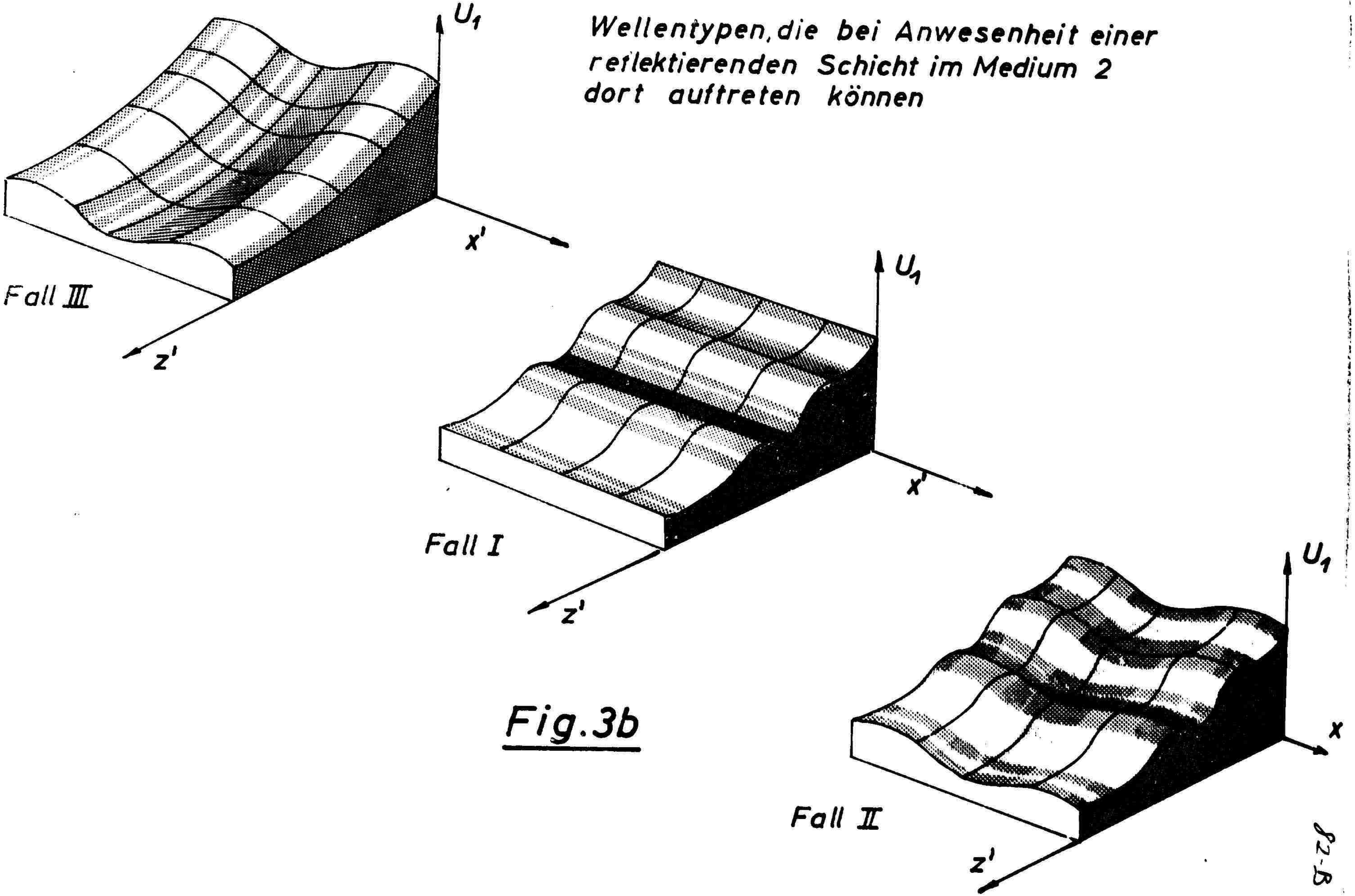

Fall III

Fall I

Fall II

Fig. 3b

From

$$k_{x',r} = |k|\cos\kappa \qquad (8.10)$$
$$k_{z',r} = |k|\sin\kappa$$

and

$$|k| = \sqrt{k_{x'}^2 + k_{z'}^2}$$

we can calculate both the period in x'-direction

$$P_{x'} = \frac{2\pi}{k_{x'} + k_{x',r}} \qquad (8.11)$$

and the period in z'-direction

$$P_{z'} = \frac{2\pi}{k_{z'} + k_{z',r}} \qquad (8.12)$$

Thus, it is possible to determine $k_{x',r}$ and $k_{z',r}$ from the rock parameters, and the period κ can be determined by means of Eq. (8.10) and finally γ is calculated from Eq. (8.7) if the mode is known.

Measurements showed a periodicity in z' thus proving the occurrence of case b).
For $\varepsilon = 10$, $\sigma = 10^{-3}$ S/mm, $f = 629$ kHz and $\phi_1 \sim 84^\circ$

$$\gamma = 36{,}7^\circ$$

The above described method fails if wavelength and dimension of the reflecting surface are in the same order of magnitude. This fact could be proved by experiments at low frequencies (278 kHz). Eqs. (8.8) and (8.9) show that $k_{x'}$ and $k_{z'}$ are proportional to ω, the periods $P_{x'}$ and $P_{z'}$ being inversely proportional to ω.

Fig. 4b is a schematical representation of the surroundings of the measuring site in the mine of Grosskogel.

Theory says that for plane waves the x- and u-waves are not attenuated, whereas the y- and v-waves are. Influencing the test results by the v-wave is impossible on account of the large distance.

8.5 Transmission coefficients

The amounts of the transmission coefficients were computed for different values of σ and represented in dependence on ϕ_i in the diagrams 4c and 4d.

$(\rho_{1+\Gamma_p})_{el}$ always remains <1, whereas $(\rho_{1+\Gamma_v})_{mag}$ can grow much larger than 1.

The present calculations, however, are not contradictory to the law of energy preservation, since the transmission coefficient of the pointing vector $\vec{S}$ is smaller than 1 in any case as is shown in Fig. 4e.

A possible explanation can be: The electric field in the dissipative medium is immediately transformed to an eddy current field. Thus, a transformation of electric into magnetic energy occurs. This is in good agreement with the unexpectedly high measuring values in winter.

On the one hand, the boundary surfaces are covered by a well conducting snow layer, on the other hand, the attenuation factor diminishes on account of the decreased humidity in winter.

8.6 The pointing vector $\vec{S}$

$\vec{S}$ was investigated for $\vec{H}$ polarized parallel to the plane of incidence and was found to be by no means stationary any more. The top of the vector $\vec{S}$ is following an ellipse being situated in the plane of incidence.

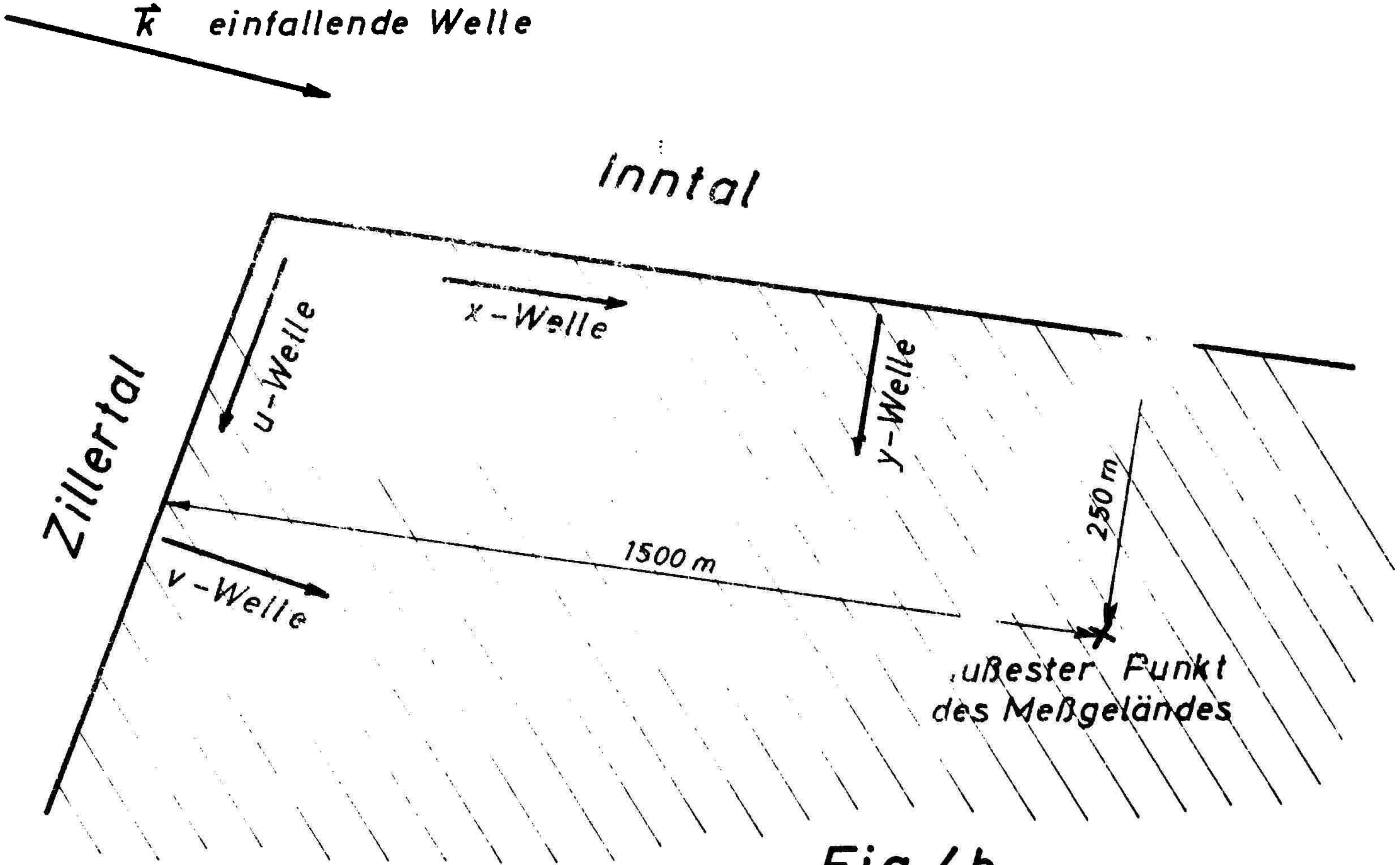
$\vec{k}$ einfallende Welle
Inntal
Zillertal
u-Welle
x-Welle
y-Welle
v-Welle
1500 m
250 m
ußester Punkt
des Meßgeländes

Fig. 4b

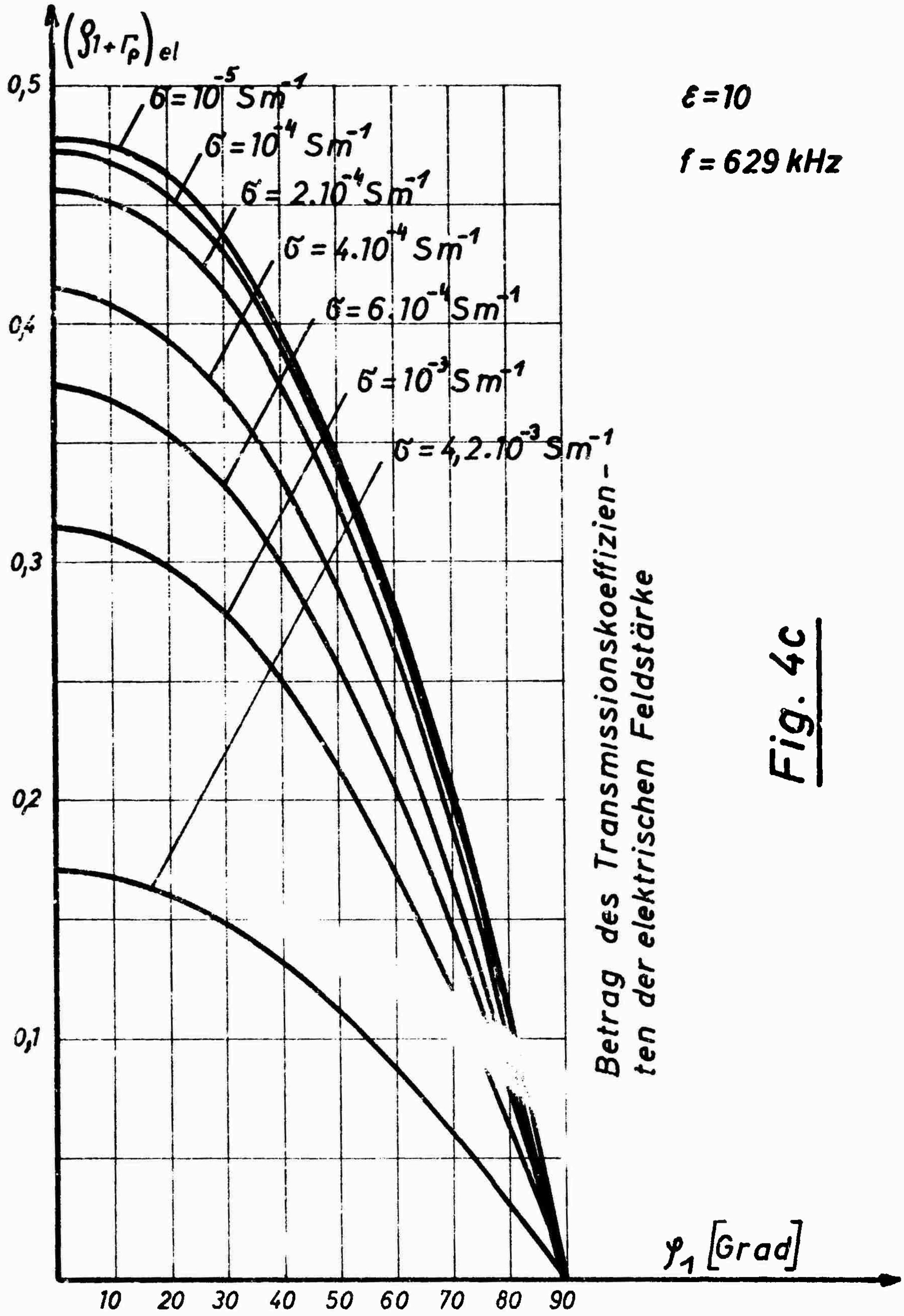

Betrag des Transmissionskoeffizienten der elektrischen Feldstärke

Fig. 4c

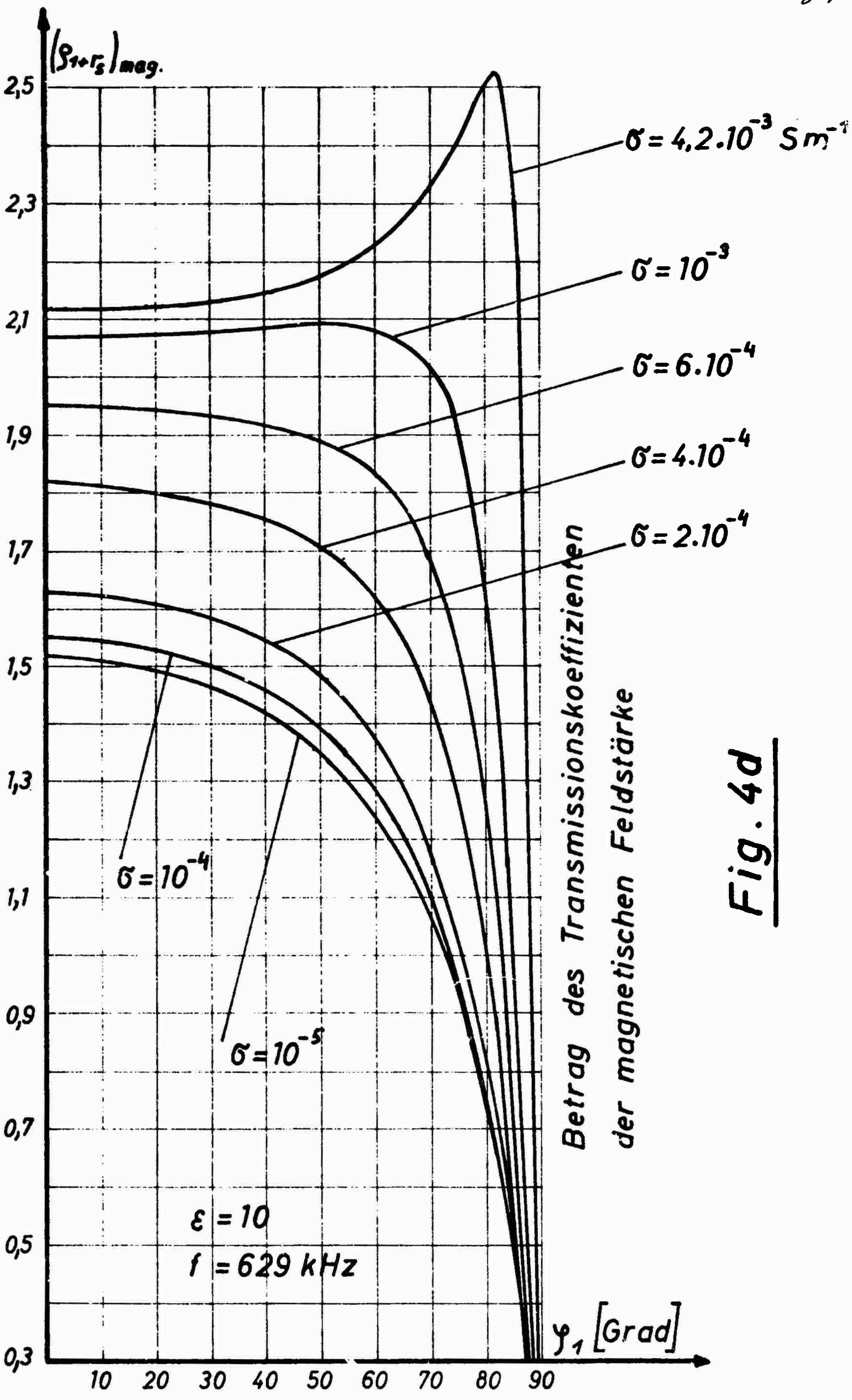

Betrag des Transmissionskoeffizienten der magnetischen Feldstärke

Fig. 4d

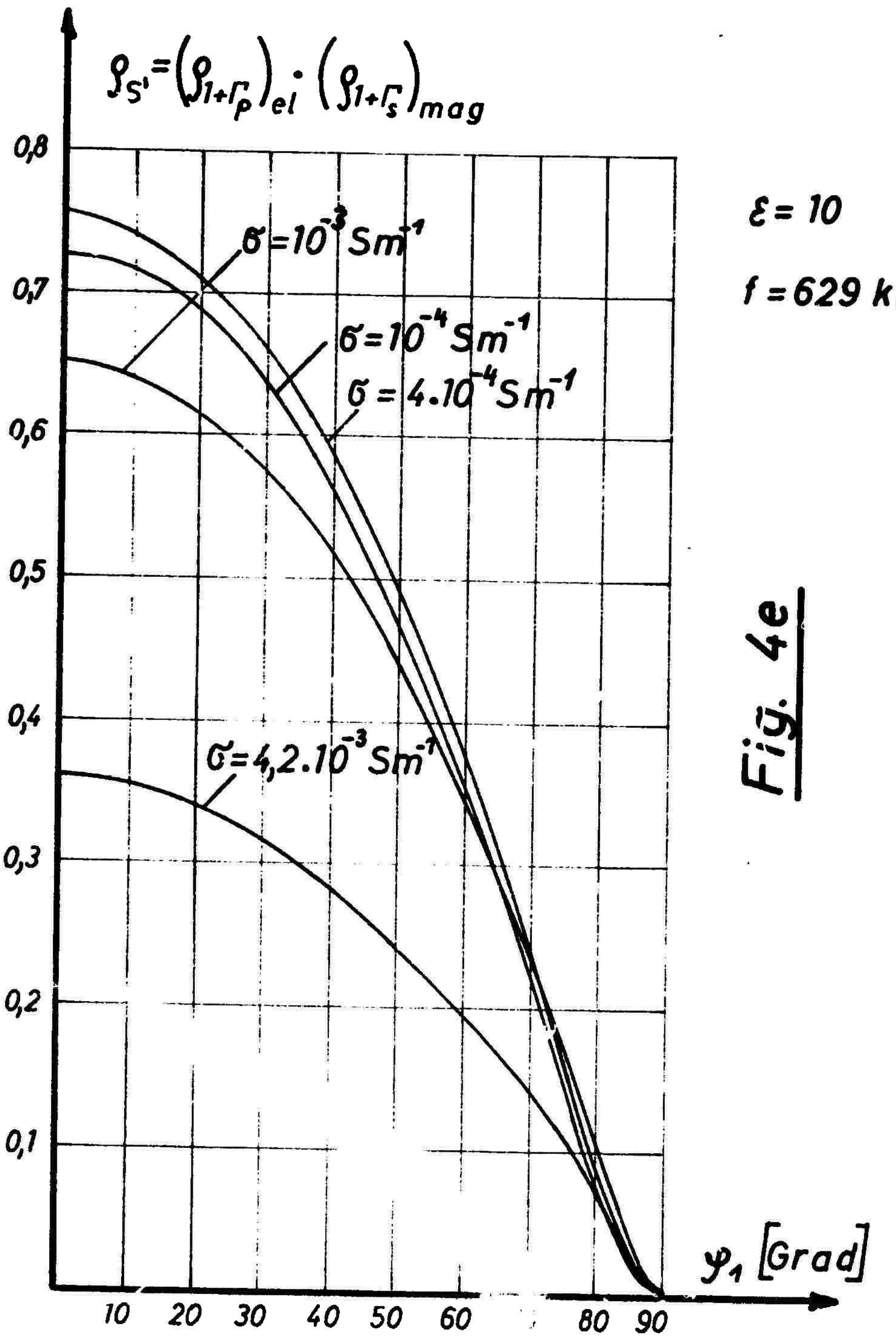

$\varepsilon = 10$

$f = 629$ kHz

Fig. 4e

84.c

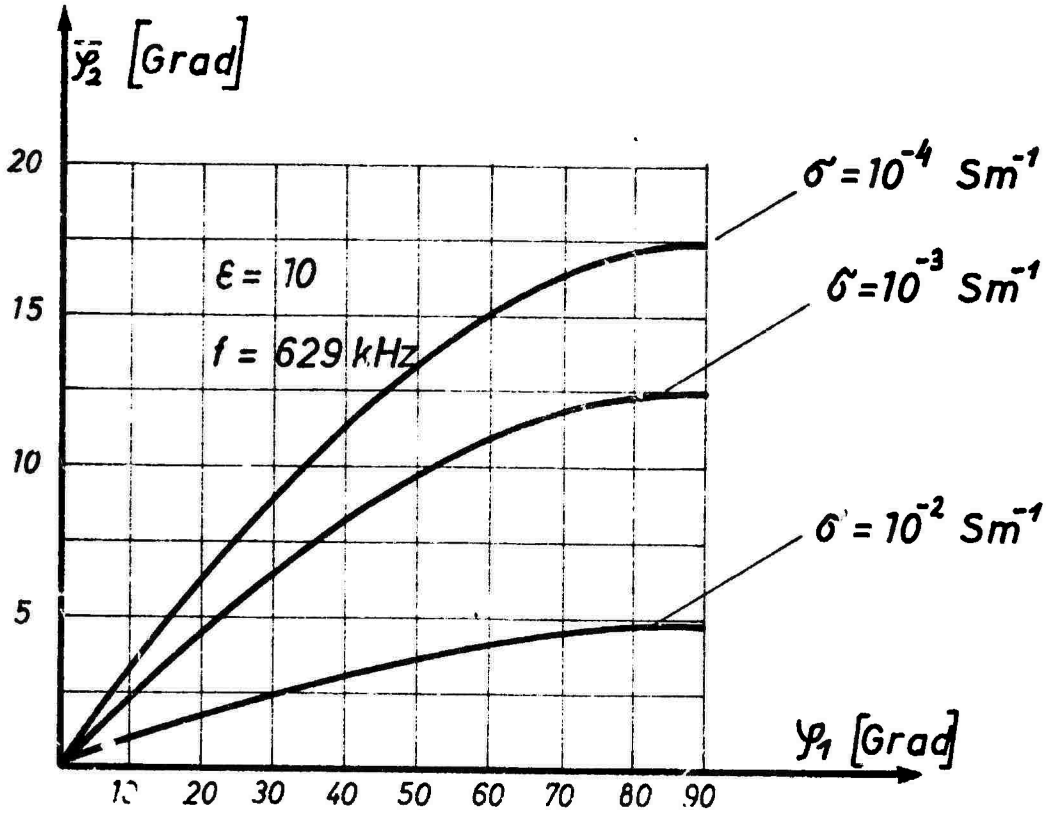

Richtung, die $\overline{\mathrm{Re}\,\vec{S}}^{\,t}$ zum Einfallslot einnimmt

Fig. 4g

For the general case of an elliptically polarized wave $\vec{S}$ is describing an oblique elliptical cone in the dissipative medium. S is complex; the mean time values of $\overline{\mathrm{ReS}}^{t}$ and $\overline{\mathrm{ImS}}^{t}$ were calculated

$$\overline{\mathrm{ReS}}^{t} = \overline{\mathrm{Im}\vec{S}}^{t}$$

So only half of the total energy is measurable.

Finally, the direction of $\overline{\mathrm{ReS}}^{t}$ in respect to the vertical incidence was examined and represented in Fig. 4g for different σ in dependence on ϕ_1.

CHAPTER 9

ABOVE-GROUND AND SUBSURFACE LONG-TIME REGISTRATION OF VLF TRANSMITTERS

Based on some preparatory experiments of W. GRADL performed in 1965, the wellknown British VLF transmitters GBR at 16.0 kHz and GBZ at 19.6 kHz were registered. The main purpose of this registration is to determine whether or not a surface wave of measurable amplitude is existing. Subsurface measurements shall make it possible to eliminate above-ground atmospherics.

To measure the GBR and GBZ signals a tube-operated selective levelmeter with a total band width of 80 Hz, which is just including the frequency jump of 50 Hz at frequency modulation was used. The simple rectification used at the beginning proved to be insufficient because the noise amplitudes amounted to a multiple of the effective amplitudes at times of greater atmospherics (thunderstorms). Only a special decoder in two stages with time constants of 0.1 and 10 sec allowed an undisturbed reception of signals.

The long integration time constant has the disadvantage of delivering a distorted pattern if the signal is amplitude-keyed, the distortion being due to the time intervals (in the order of seconds). There are always 2 hours of information followed by 1 hour of outage which showed up to be a negligible loss of information.

Since the tube-operated receiver did not maintain the adjusted receiving frequency with sufficient accuracy for a period of several days (owing to unevitable temperature fluctuations) a varicap was added to the oscillator thus providing the possibility of wobbling a certain frequency band externally. Fig. 9.1 shows the block diagram of the complete equipment.

Long ferrite rod antennas which were optimized adequately have proved successful /9, 31, 32/. The essential piece of the equipment is the selective levelmeter with an input sensitivity of -11 neper corresponding to about 10 µV. The saw-tooth voltage of a Wavetek 142 with 10 min time constant was used as sweep control. The output signal of the levelmeter was amplified by 14 dB to max. 4 V by a PM 5175 (Philips) to keep down the error influence of the threshold voltage of the decoding diodes. The decoded signal is registered on a line recorder and constitutes a spectral distribution of the VLF signals in the requested frequency range. Fig. 9.2 shows a part of such a registration tape.

One measuring point per transmitter for every 10 minutes proved just sufficient, an increase in wobbling frequency would have caused a decrease of the registered maximum amplitudes on account of the integration time constant.

The signals of all receivable VLF transmitters in the world within the frequency range of 14.5 to 20.5 kHz were received above and below the earth surface. The object was to find out whether over a propagation distance of 1300 km, several 100 m below the surface, the sky waves, i.e. the signal, that is reflected by the ionosphere, form the main part of the received signal or if the surface waves represent a considerable amount of signal or the signal at all.

For this purpose the course of the signal amplitude of the GBR transmitter (16.0 kHz) was plotted in the same scale during 24 hours from both a measurement below and above the earth surface (Fig. 9.3). The two curves were measured on two different days, because only one reception apparatus was available. A determination of a mean value of amplitudes over a period of several days was impossible, since this would have blurred the characteristic sudden increase of amplitude at sunrise. The two curves may be regarded as standing for a number of curves plotted under the same conditions. From the curves it is obvious that the wave in soil (curve 2) is certainly the sky wave, because the attenuation measured at the very constant amplitude during daytime corresponds exactly to the precalculated attenuation of the sky wave. Furthermore, the course of amplitude at sunrise and sunset characteristic for the sky wave can be determined equally above and below the surface. If the fluctuating night course of several measuring series below and above the surface is averaged, the same amplitude ratio as during daytime can be calculated. If there were a signal portion of significant magnitude that is independent on the ionosphere, the amplitude ratio would change on account of the different attenuation for surface and sky waves. Thus, it is evident that the ionosphere has a significant influence on the diurnal course of amplitude even at subsurface reception.

The dashed parts of the curve in Fig. 9.3 are estimated values corresponding to the AM-periods of the transmitter. This characteristic course could be observed during all the time of registration (several months) in practically the same way. It must be mentioned that at night the amplitude is considerably smaller than at daytime.

Plotting the GBZ transmitter at 19.6 kHz with the same location brought about quite different results (Fig. 9.4).

REGISTRIERANLAGE

Blockschaltbild

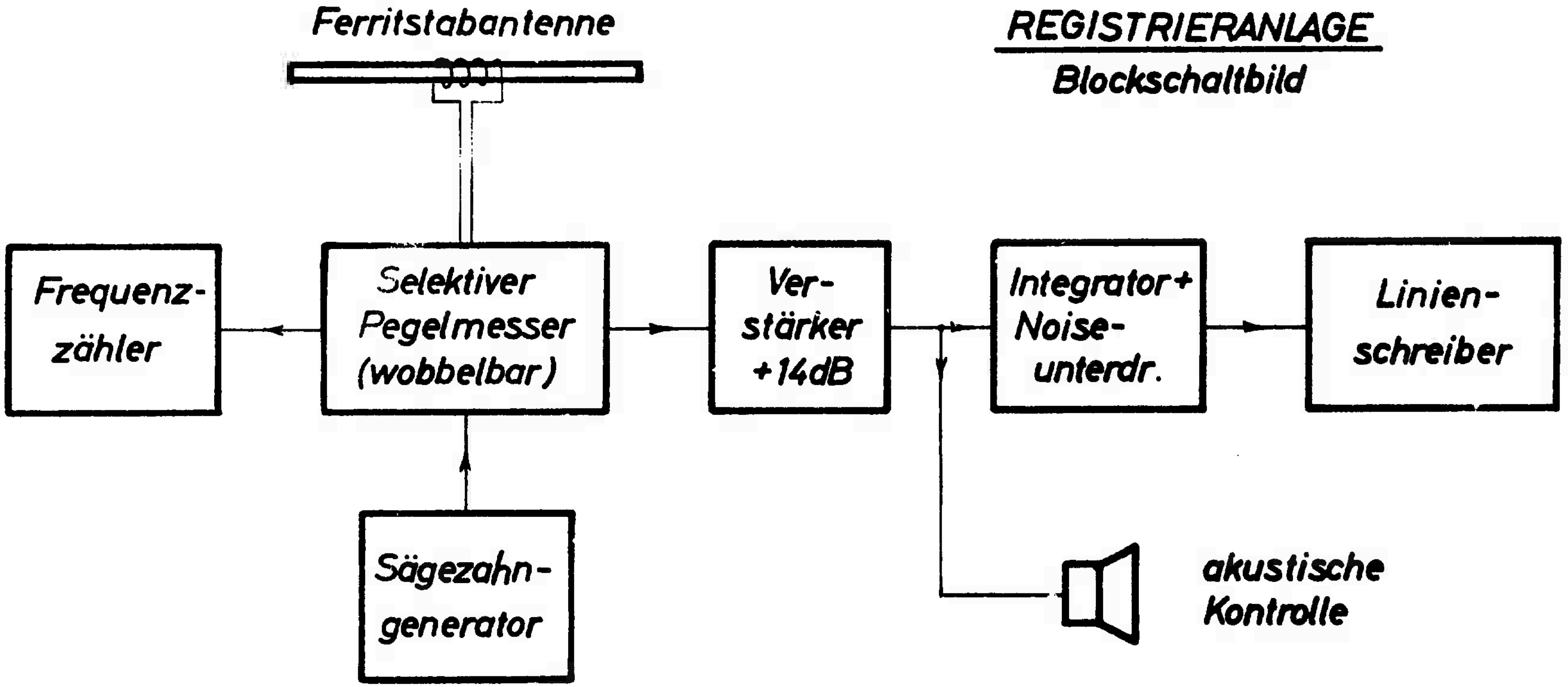

Fig. 9.1

88 B

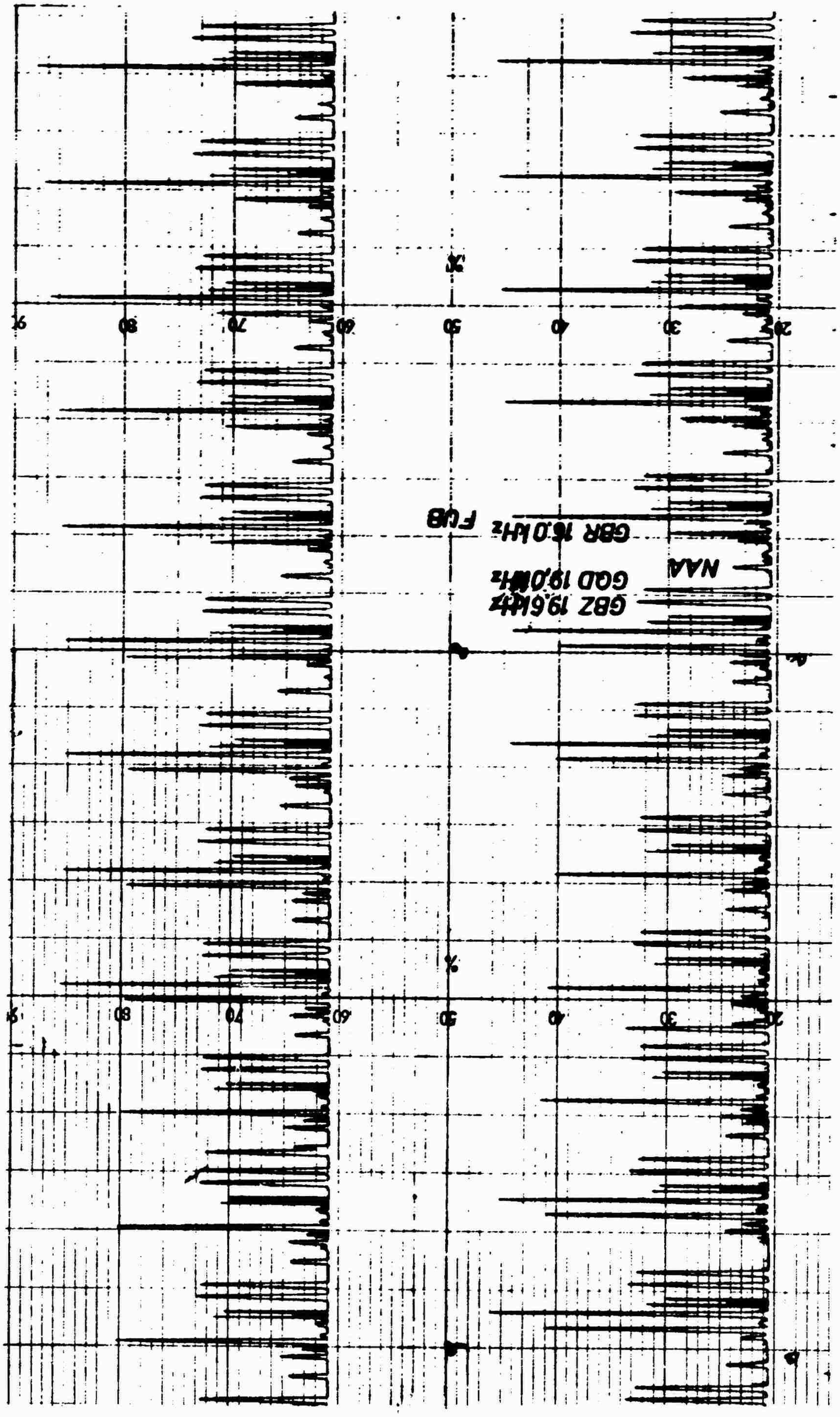

Fig.: 9.2

GBR- (16,0kHz) Registrierung

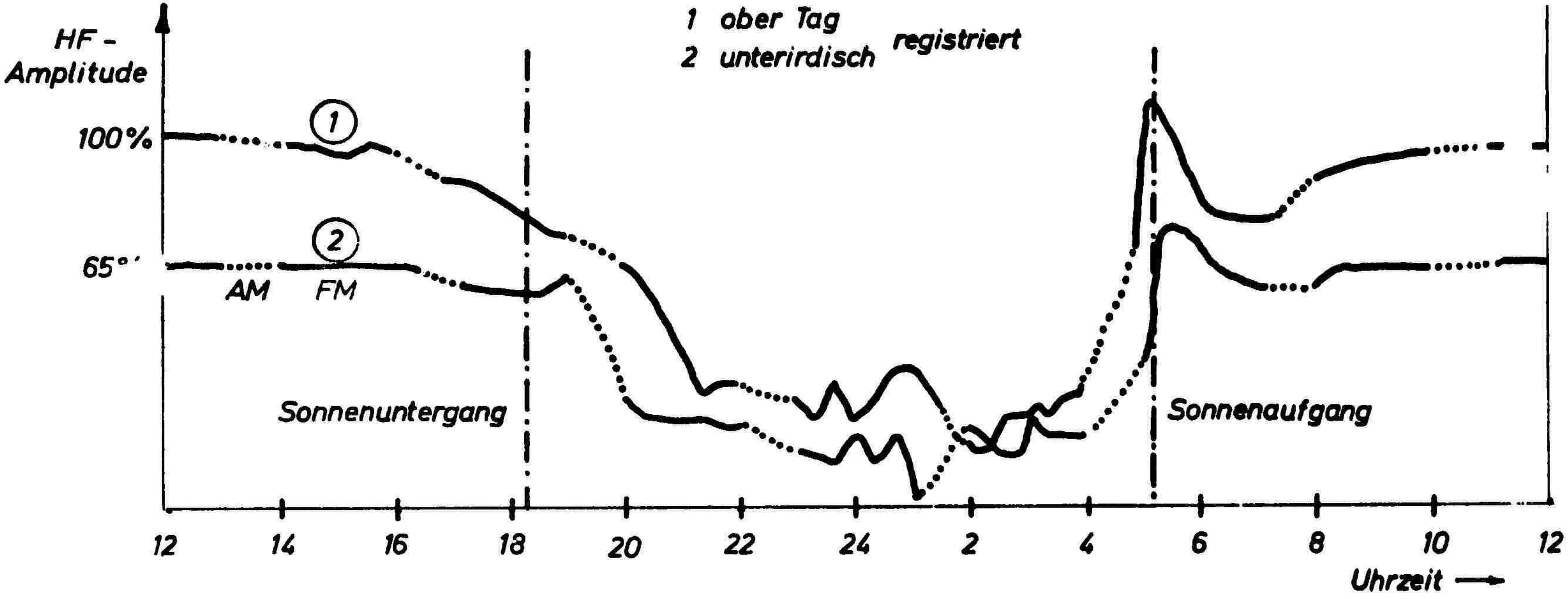

Fig.9.3

Nachtamplitude

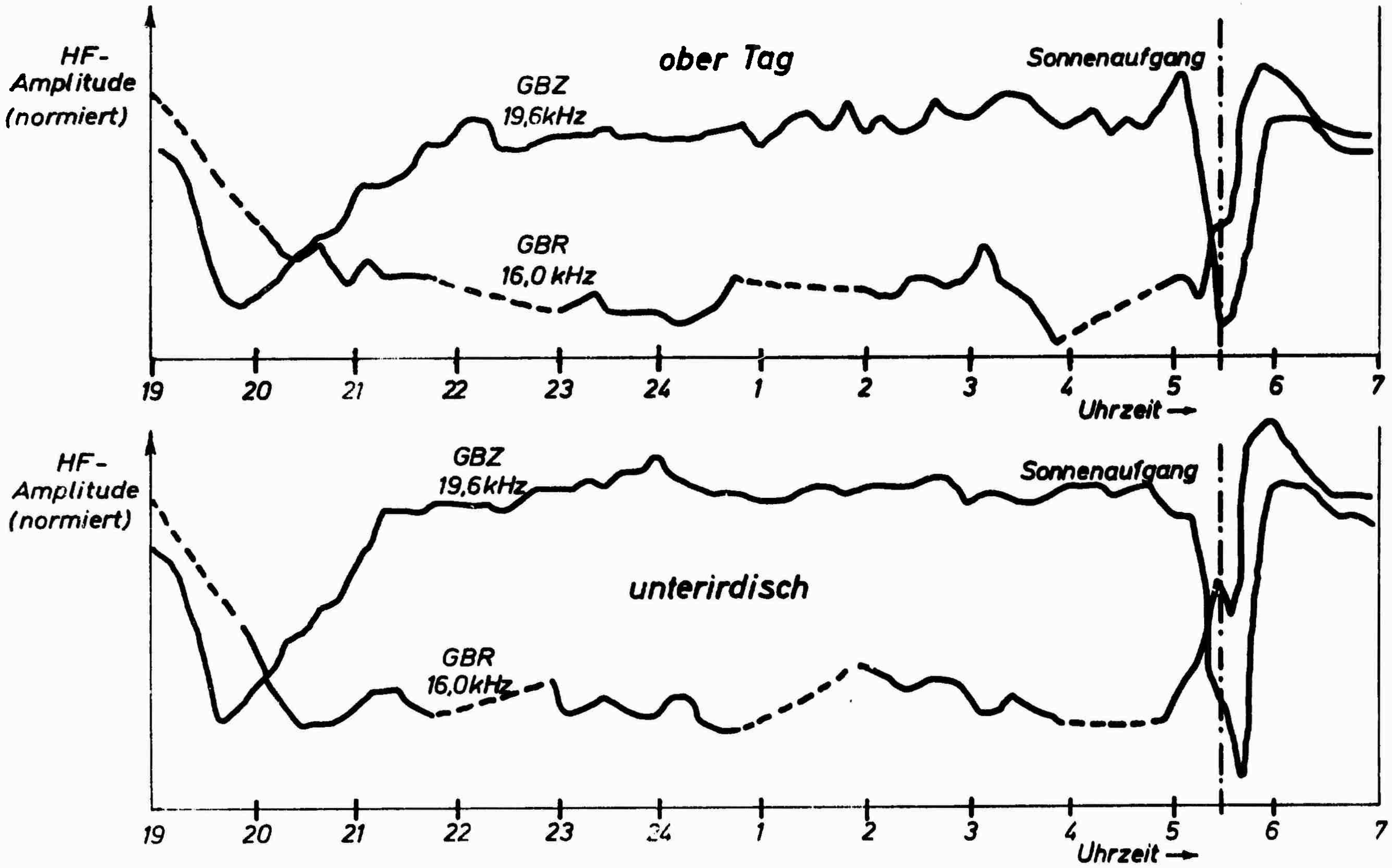

Fig. 9.4

88-D

In Fig. 9.4 the night course between 7 p.m. and 7 a.m. is plotted. The diurnal course of the two transmitters is approximately identical (GBZ amplitude is by about 20 % smaller than GBR amplitude) whereas the GBZ night amplitude comes up to the value of the day amplitude. In some nights the day values were even exceeded.

The upper diagram of Fig. 9.4 shows the characteristic conditions of the above-ground registration, the diagram below shows the interpretation of a subsurface registration.

Since there was only one device available to plot all these diagrams an exact coincidence of the reception characteristics is impossible. Two comparable diagrams had to be measured on two different days.
To eliminate accidental fluctuations, a greater number of above-ground and subsurface diagrams was interpreted always showing this distinct difference between the two neighboring frequencies of 16 and 19.6 kHz. It is principally possible to take an average of the different similar diagrams and would equalize the slight fluctuations of the night course, but the characteristic sunrise peaks would also be blurred.

For a further examination of these effects it is absolutely necessary to register the signal amplitudes above and below the earth surface simultaneously. Two battery-operated registration devices are already under construction, using a magnetic tape instead of the line recorder as a data carrier. Thereby it will be possible to show up clearly one of the expected advantages of a subsurface registration, namely the fact, that artificial or man-made noise peaks are more heavily attenuated than the measuring signal penetrating from outside. This effect was partly determined with the simple equipment already and is due to the fact that the signal of the two transmitters arrives as a farfield at the point of reception whereas the especially disturbing noise peaks from the near neighborhood arrive as a nearfield with a multiple of the measuring amplitude. This is explained by the following two diagrams (Figs. 9.5 and 9.6).

Fig. 9.5 shows an above-ground registration during a local thunderstorm; it can be seen that instead of the zero line there is a beam of numerous noise peaks which come through very distinctly in spite of the efficient noise inverter.

Fig. 9.6 represents the equivalent subsurface registration showing an absolutely undisturbed diagram when passing frequency ranges without transmitting signals. An exact correlation of these diagrams is again impossible, as they were plotted at different times.

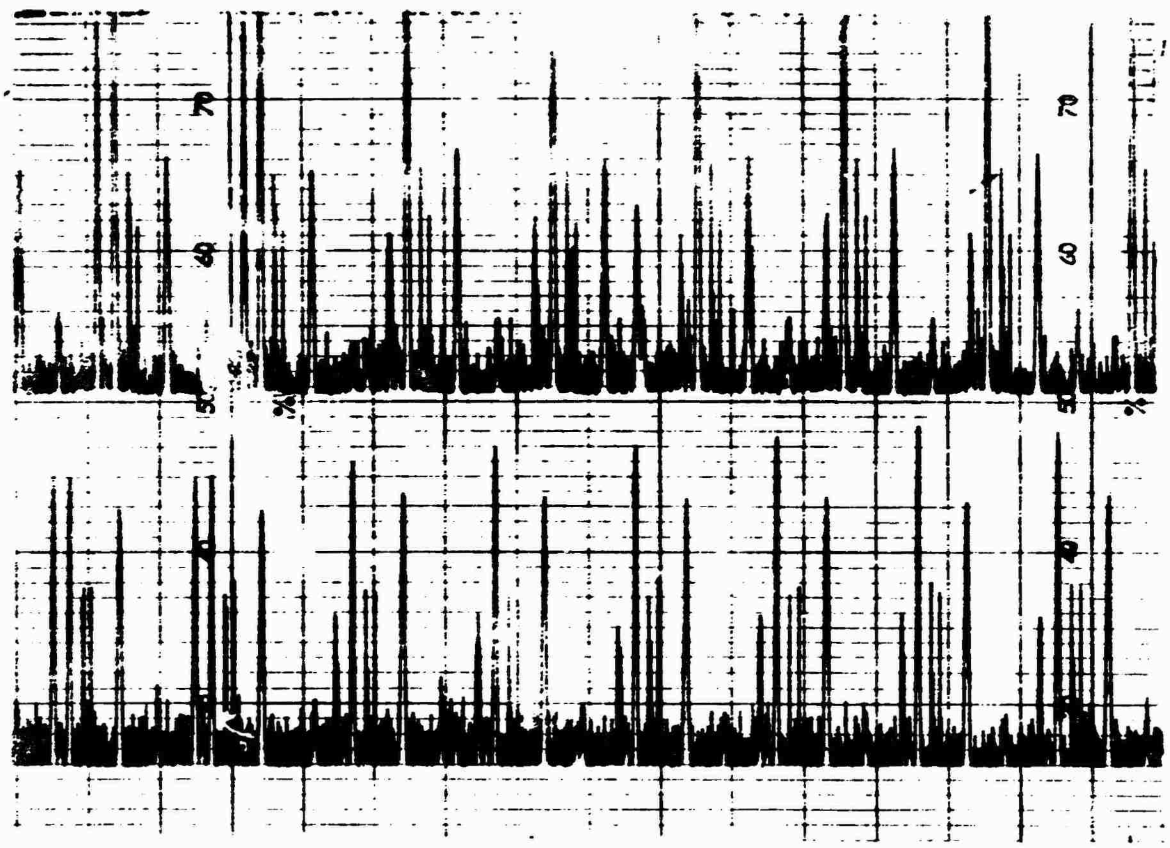

Fig.: 9.5

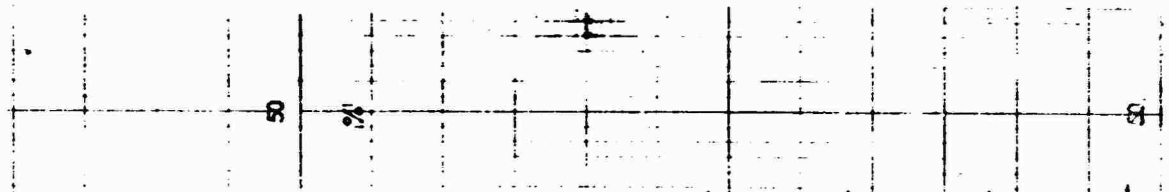

Fig.: 9.6

REFERENCES

1 LUKAVEC, R., Über die Eigenschafter kleiner eigenresonanter Wendelantennen bei niedrigen Frequenzen und ihre Felder in dissipativen Medien. Thesis, Innsbruck University, 1969

2 HEYNISCH, H., Die Ausbreitung von Mikrowellen und langen Wellen auf einer Wendelleitung mit Dielektrikum und koaxialem Außenleiter. A.E.Ü. vol. 17, no. 5

3 MEINKE, H., and GUNDLACH, F. W., Taschenbuch der ~~Hf~~-Technik, Springer Verlag Wien/New York, 1968

4 HÜTTE 5b, Des Ingenieurs Taschenbuch, Teil B, Berlin/München, 1962

5 WHEELER, H. A., Fundamental Limitations of Small Antennas, Proc. I.R.E., pp. 1479-1484, Dec. 1947

6 ZHURT, H., Elektromagnetische Strahlungsfelder, Springer Verlag Wien/New York, p. 151, 1953

7 WHEELER, H. A., A Helical Antenna for Circular Polarization, Proc. I.R.E., pp. 1484-1488, Dec. 1947

8 GABILLARD, R., DEGAUQUE, P., and WAIT, J. R., Subsurface Electromagnetic Telecommunication - A Review, IEEE Transactions on Communication Technology, vol. 19, no. 6, pp. 1217-1228, Dec. 1971

9 BITTERLICH, W., Magnetische Dipolantennen für Feldstärkemessungen im LF- und LF-Bereich. Internat. Elektr. Rundsch. Berlin, vol. 21, no. 9, pp. 225-228, 1967

10 NESSLER, N., Die Ausbreitung langer elektromagnetischer Wellen durch homogene und inhomogene feste Medien. Thesis, Innsbruck University, 1967

11 Final Scientific Report, Theoretical and Experimental Studies of VLF and LF Waves; US-Contract No. F44620-72-C-0071, Innsbruck University, 1971

12 ROTHE, R., Höhere Mathematik für Mathematiker, Physiker, Ingenieure. G.B. Teubner, Leipzig, 1954

13 BERGMANN, L., Messungen im Strahlungsfeld eines Hertz'schen und eines Abraham'schen ungedämpften Erregers. Ann. Phys. vol. 4, p. 13 ff., 1967

14 KELLNER, A. W., Die Bestimmung elektrischer Gesteinsparameter aus der Feldstruktur eines magnetischen Dipols. Thesis, Innsbruck University, 1969

15 BERGMANN, L., SCHAEFFER, Cl., and MATOSSI, F., Lehrbuch der Experimentalphysik, Optik. Walter de Gruyter & Co., Berlin, 1966.

16 KLEIN, R., Mathematical Classification and Description of the Response Characteristic in the Elliptically Polarized VLF and LF Field, Scient. Rep. No. 3, US-Contract No. F44620-72-C-0052, Innsbruck University, 1972

17 KLEIN, R., Einfluß von Stollenhohlräumen und Inhomogenitäten auf die Ausbreitung von elektromagnetischen Langwellen durch leitfähiges Medium. Thesis, Innsbruck University, 1972

18 BRONSTEIN-SEMENDJAJEW, Taschenbuch der Mathematik, Verlag Harry Deutsch, Zürich/Frankfurt a.M., 1967

19 TEICHMANN, H., Physikalische Anwendung der Vektor- und Tensorrechnung, BI Hochschultaschenbuch 39/39a, Mannheim, 1966

20 BITTERLICH, W., A Phase-sensitive Receiver for VLF Signals, Annual Report, US-Contract No. F61052-69-C0007, Innsbruck University, 1969

21 BECKSTEIN, H., Schmitt-Trigger mit in weiten Grenzen einstellbarer Hysterese. Elektronik, Franzis-Verlag München, no. 12, p. 360, 1969

22 BITTERLICH, W., Einführung in die Elektronik, Springer-Verlag Wien/New York, p. 512-517, 1967

23 BECKER, K. D., On Reflection and Refraction of Electromagnetic Dipole Fields at Rough Surfaces of Homogeneous and Inhomogeneous Media. Bericht des Instituts für Radiometeorologie und maritime Meteorologie, Hamburg, No. 21, 1972

24 Handbuch der Physik, Springer Verlag Wien/New York, vol. 16, 1958

25 WAIT, J. R., Oblique Reflection of an Electromagnetic Plane Wave from a Striated Impedance Surface, Journal of Mathematical Physics, vol. 11, no. 4, 1970

26 PESCHL, E., Funktionentheorie I, BI Hochschultaschenbuch 131/131a, Mannheim

27 VILBIG, F., Lehrbuch der Hochfrequenztechnik, Akademische Verlagsgesellschaft, Leipzig, 1942

28 WÖBKING, H., Über den Frequenzgang der Dielektrizitätskonstante und der elektrischen Leitfähigkeit bei Gesteinen. Thesis, Innsbruck University, 1968

29 GRISSEMANN, Ch., Untersuchung der komplexen Leitfähigkeit und Dielektrizitätskonstanten erzhaltiger Gesteine an Gesteinsmodellen, Thesis, Innsbruck University, 1971

30 SCHUMANN, W. O., Elektrische Wellen, Carl Hauser Verlag, München, 1948

31 NESSLER, N., BITTERLICH, W., Überlegungen zur Eichung einer Ferritstabantenne für Meßzwecke. Intern. El. Rundsch, Berlin, vol. 25, pp.277-279, 1971

32 BITTERLICH, W., Measuring Device for Recording the Field Strength of VLF Signals over Long Periods of Time, Scient. Rep. No. 14, US-Contract No. 61(052)-490, 1965

33 STEINACKER, I., SCOTTI, H., Attenuation in Subsurface Signal. Techn. Note No. 2, US-Contract No. 61(052)-490, 1963

34 BITTERLICH, W., HOMMEL, R., Determination of Rock Conductivity from VLF-Propagation Measurements. Techn. Note No. 3, US-Contract No. 61(052)-490,1963

35 NESSLER, N., BITTERLICH, W., Die Messung der Leitfähigkeit und der Dielektrizitätskonstanten eines schwach leitfähigen homogenen Mediums mittels Wellenausbreitung. Acta Physica Austriaca, Springer Verlag Wien/New York, vol. 29, pp. 228-240, 1969

36 BITTERLICH, W., Altes Bergwerk mit neuen Aufgaben. Der Aufschluß, vol. 21, pp. 107-111, 1970

37 WAIT, J. R., Image Theory of a Quasistatic Magnetic Dipole Over a Dissipative Half-Space. Electronics Letters, vol. 5, no. 13, pp. 281-282, 1969

38 WEAVER, J. T., Image Theory for an Arbitrary Quasistatic Field in the Presence of a Conducting Half-Space. Radio Sci. vol. 6, no. 6, pp. 647-654, 1971

39 BANNISTER, P. R., Utilization of Image Theory. Techniques in Determining the Mutual Coupling between Elevated Long Horizontal Line Sources, Radio Sci., vol. 5, no. 11, pp. 1375-1381, 1970

40 WASYLKIWSKYJ, W., Gain Efficiency and Receiving Cross Section of Antennas in a Dissipative Medium. Radio Sci., vol. 6, no. 6, pp. 647-653, 1971.